TU/e EINDHOVEN UNIVERSITY OF TECHNOLOGY

Short-range longitudinal and transverse wakefield effects in FERMI@Elettra FEL project

Citation for published version (APA):
Craievich, P. (2010). *Short-range longitudinal and transverse wakefield effects in FERMI@Elettra FEL project*. [Phd Thesis 2 (Research NOT TU/e / Graduation TU/e), Applied Physics and Science Education]. Technische Universiteit Eindhoven. https://doi.org/10.6100/IR676789

DOI:
10.6100/IR676789

Document status and date:
Published: 01/01/2010

Document Version:
Publisher's PDF, also known as Version of Record (includes final page, issue and volume numbers)

Please check the document version of this publication:

• A submitted manuscript is the version of the article upon submission and before peer-review. There can be important differences between the submitted version and the official published version of record. People interested in the research are advised to contact the author for the final version of the publication, or visit the DOI to the publisher's website.
• The final author version and the galley proof are versions of the publication after peer review.
• The final published version features the final layout of the paper including the volume, issue and page numbers.

Link to publication

General rights
Copyright and moral rights for the publications made accessible in the public portal are retained by the authors and/or other copyright owners and it is a condition of accessing publications that users recognise and abide by the legal requirements associated with these rights.

• Users may download and print one copy of any publication from the public portal for the purpose of private study or research.
• You may not further distribute the material or use it for any profit-making activity or commercial gain
• You may freely distribute the URL identifying the publication in the public portal.

If the publication is distributed under the terms of Article 25fa of the Dutch Copyright Act, indicated by the "Taverne" license above, please follow below link for the End User Agreement:

www.tue.nl/taverne

Take down policy
If you believe that this document breaches copyright please contact us at:

openaccess@tue.nl

providing details and we will investigate your claim.

Download date: 04. Oct. 2023

Short-range longitudinal and transverse wakefield effects in FERMI@Elettra FEL project

PROEFSCHRIFT

ter verkrijging van de graad van doctor aan de
Technische Universiteit Eindhoven, op gezag van de
rector magnificus, prof.dr.ir. C.J. van Duijn, voor een
commissie aangewezen door het College voor
Promoties in het openbaar te verdedigen
op maandag 27 september 2010 om 14.00 uur

DOOR

Paolo Craievich

geboren te Trieste, Italië

Dit proefschrift is goedgekeurd door de promotoren:

prof.dr. M.J. van der Wiel
en
prof.dr. F. Parmigiani

Copromotor dr.ir. O.J. Luiten

Druk: Universiteitsdrukkerij Technische Universiteit Eindhoven
Ontwerp omslag: P. Craievich and E. Zettin

A catalogue record is available from the Eindhoven University of Technology Library
ISBN: 978-90-386-2294-1

The work described in this thesis has been carried out at the ELETTRA laboratory of Sincrotrone Trieste (Italy) under the FERMI@Elettra Free Electron Laser project.

Ai miei genitori, a mia moglie Erika, mio figlio Alvise e...

Avevo una città bella tra i monti rocciosi e il mare luminoso
Umberto Saba

...my soul is in Trieste...
James Joyce

La vita non è né brutta né bella ma è originale!
Italo Svevo

Contents

1 Introduction **1**
1.1 The FERMI@Elettra Facility . . . 1
1.2 Introduction to the wakefields . . . 4
1.2.1 Diffraction wakes . . . 9
1.2.2 Resistive wall wake . . . 10
1.2.3 Surface roughness wake . . . 12
1.3 This thesis . . . 12
1.3.1 Publications . . . 14
References . . . 15

2 Short-range wakefields in the BTW accelerating structures **17**
2.1 Introduction . . . 18
2.2 Analytical estimations . . . 21
2.3 Single-Cell Structure . . . 22
2.4 Multi-Cell Structure . . . 25
2.5 Longitudinal wake function . . . 25
2.6 Transverse wake function . . . 31
2.7 Single bunch energy spread . . . 36
2.8 Conclusion . . . 38
References . . . 43

3 Beam break-up instability in the FERMI@Elettra linac **45**
3.1 Introduction . . . 46
3.2 Study outline . . . 47
3.3 Theoretical background . . . 48
3.3.1 Equation of motion . . . 48
3.3.2 Wake function . . . 48
3.4 Static trajectory distorsion . . . 49
3.4.1 Machine Error Budget . . . 49
3.4.2 Trajectory Distortion by Collective Effects . . . 51
3.4.3 Trajectory Local Bumps . . . 51
3.5 Trajectory Jitter Budget . . . 52
3.5.1 Launching Error . . . 52
3.5.2 Quadrupole Vibration and Current Ripple . . . 54

3.5.3 Parasitic Dispersion . . . 55
3.6 Shot-to-shot trajectory jitter . . . 57
3.6.1 Projected Emittance . . . 57
3.6.2 Banana Shape . . . 59
3.6.3 Slice Centroid Amplitude . . . 59
3.7 Conclusion . . . 64
References . . . 66

4 Wakefield induced energy spread in the undulator vacuum chamber 69
4.1 Introduction . . . 70
4.2 Physical model description . . . 70
4.3 Fields in the vacuum . . . 71
4.4 Fields in the resistive wall . . . 75
4.4.1 Longitudinal fields in the conductor . . . 76
4.4.2 Transverse fields in the conductor . . . 78
4.5 Evaluation of the constants . . . 79
4.6 Short-range Wake Functions . . . 82
4.7 Examples and results . . . 83
4.8 Wakefield effects in the FERMI FEL 1 Undulator Vacuum chamber . . . 91
4.8.1 The Resistive Wall Wakes . . . 91
4.8.2 The Surface Roughness Wakefields . . . 96
4.8.3 Induced energy variation for the SLB case with $b = 5mm$ . . . 96
4.9 Conclusion . . . 99
References . . . 101

5 Passive longitudinal phase space linearizer 103
5.1 Introduction . . . 104
5.2 Longitudinal wake function . . . 104
5.3 Rectangular bunch distribution . . . 105
5.4 Tracking results for a rectangular bunch distribution . . . 110
5.4.1 Case 1: $L_b = 3.5mm$ and $C = 3.5$ . . . 110
5.4.2 Case 2: $L_b = 2mm$, and $C = 6$ . . . 112
5.5 Ramped bunch distribution . . . 114
5.6 Tracking results using a passive linearizer and fourth-harmonic system . . . 117
5.7 Conclusion . . . 118
References . . . 120

6 Conclusion and outlook 121
References . . . 126

Summary 127

Acknowledgments 129

Curriculum Vitae 130

Chapter 1

Introduction

1.1 The FERMI@Elettra Facility

The FERMI@Elettra Free Electron Laser (FEL) project is a soft X-ray fourth generation light source under development at the ELETTRA Laboratory of Sincrotrone Trieste [1]. It is one of the FEL based European projects, designed to become the international user facility in Italy for scientific investigations, with ultra high brillance X-ray pulses, of ultra-fast and ultra-high resolution processes in material science and physical biosciences.
The FERMI single-pass FEL facility will be driven by the present ELETTRA injector S-band linac, upgraded by the addition of seven accelerating sections to bring its top energy to 1.5 GeV and of a new photoinjector as a low emittance electron source. The Linac repetition rate will also be ramped up from 10 Hz to 50 Hz. The upgraded Linac 1.5 GeV electron beam energy plus a complex of state-of-the-art undulators will allow FERMI to cover the $100 - 20nm$ wavelength region in a first phase (FEL-1) and to reach down to $4nm$ in a second, later phase (FEL-2). A general layout of the facility is shown in Figure 1.1 and 1.2.
The accelerator and FEL complex comprises the following parts:

- A photoinjector and two short linac sections (S0A and S0B), generating a bright electron beam and accelerating it to $\sim 100MeV$.
- The main linear accelerator, where the electron beam is time-compressed and accelerated to $\sim 1.5GeV$.
- The electron beam transport system to the undulators.
- The undulators complex, in which the FEL radiation is generated.
- The photon beam transport lines from the undulator to the experimental area.
- The experimental area.

The photoinjector is based on the proven 1.6 cell electron gun developed at BNL, SLAC and UCLA. Given the similarities between the LCLS and FERMI photoinjector requirements, this design draws heavily on the LCLS concept to produce a $10ps$ long pulse with $0.8-1$ nC charge and a rms normalized transverse emittance of $1.2mm\ mrad$ at $100MeV$. The repetition rate is $10Hz$

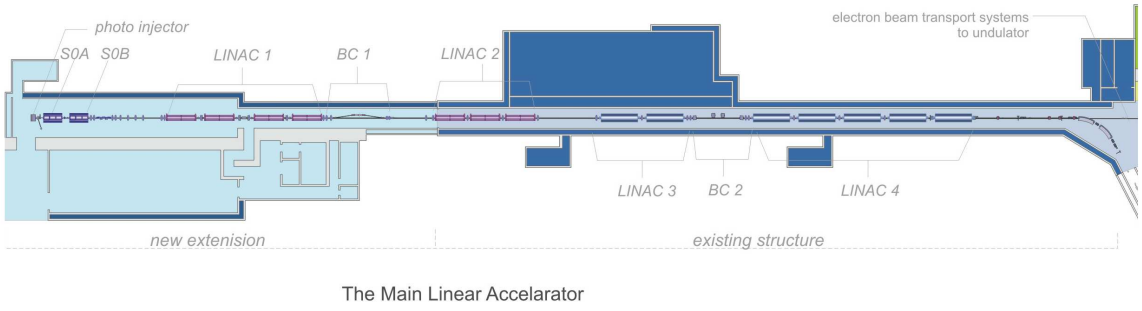

Figure 1.1: The main linear accelerator.

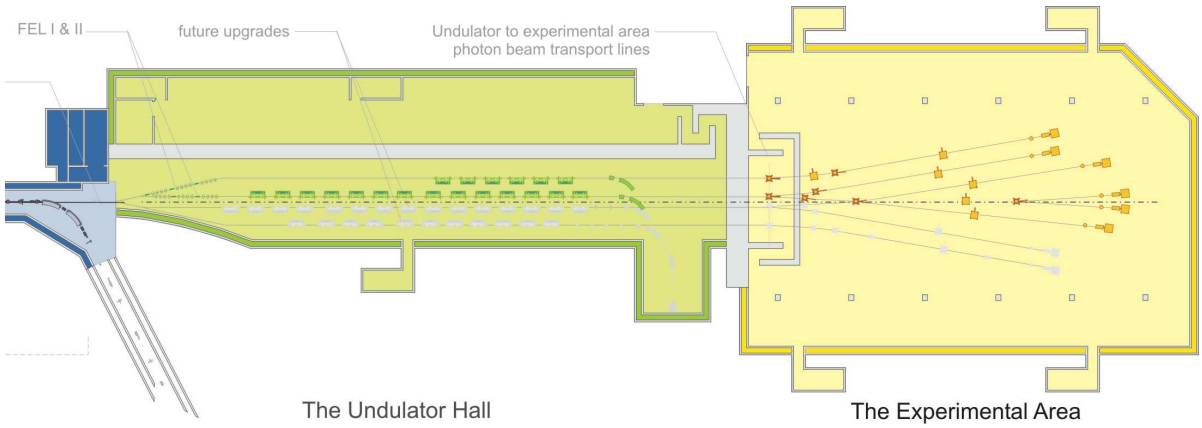

Figure 1.2: The undulator hall and the experimental area.

during the initial stage of operation, but the design allows for upgrading the photoinjector to $50Hz$. Following standard layout schemes, the design includes a solenoid for emittance compensation and acceleration to $100MeV$ with two S-band rf sections. These sections, named $S0A$ and $S0B$, are part of the present ELETTRA injection system. A laser pulse provides temporal and spatial bunch shaping. The FERMI design calls for a novel temporal bunch profile in which the bunch current increases approximately linearly with time (linear ramp) [2]. Such as profile at the start of acceleration produces a more uniform energy and current profile at the entrance to the undulators. The function of the main linear accelerator is to accelerate the $\sim 10ps$ long electron bunch exiting the photoinjector to $\sim 1.5GeV$ and to compress the beam to its final duration and peak current as shown in Figure 1.3. Two FEL layouts are envisaged in FERMI and in both the cases the energy and charge distributions correlated with the distance along the electron bunch should be as flat as possible in order not to broaden the FEL bandwidth. The design values of energy and peak current variations along the useable part of the bunch are specified to be less than 2×10^{-4} and $\sim 100A$ respectively. At the exit of the photoinjector, the electrons enter the L1 linac (four C-type sections) where they are accelerated to $\sim 300MeV$. Acceleration off-crest creates the correlated energy spread along the bunch needed to compress it in the first compressor, BC1. An X-band rf structure tuned at the 4^{th} harmonic of the main (3 GHz) linac frequency is placed half-way between the four C-type sections of L1. The function of the structure is to provide the non-linear quadratic

and, when operated off-crest, cubic corrections of the correlated momentum distribution along the bunch in the presence of the photoinjector, of the non-linearities of the magnetic compressors and of the longitudinal wakefields. The L2 and L3 linac structures, located between the first and second bunch compressors, accelerate the beam from $\sim 300MeV$ to $\sim 650MeV$. They also provide the residual momentum chirp needed for the second compressor, BC2. After BC2 the beam is accelerated to its final $\sim 1.5GeV$ energy in the L4 structure. The rf phases of the linac sections following BC1 are chosen to provide the necessary momentum spread for compression and also to cancel the linear part of the longitudinal wakes. The non-linear correlated momentum spread at the end of the linac is fine-tuned by acting on the amplitude and phase of the x-band structure. The linac focusing system is designed to minimize transverse emittance dilution due to transverse wakefields, momentum dispersion and coherent synchrotron radiation in bends. Figure 1.4 shows the two transfer lines, one assigned to FEL-1 and the other to FEL-2, that transport the electron beam from the linac end to the undulators. This system, called the "Spreader", starts with two

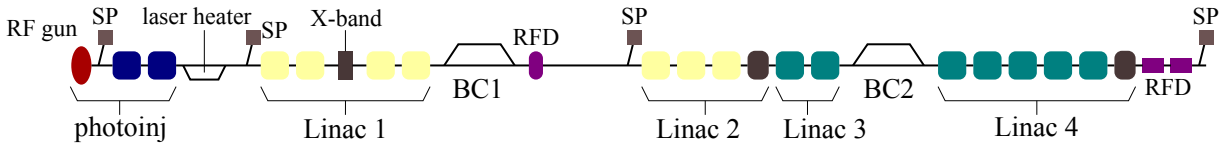

Figure 1.3: The main linac and photoinjector layouts.

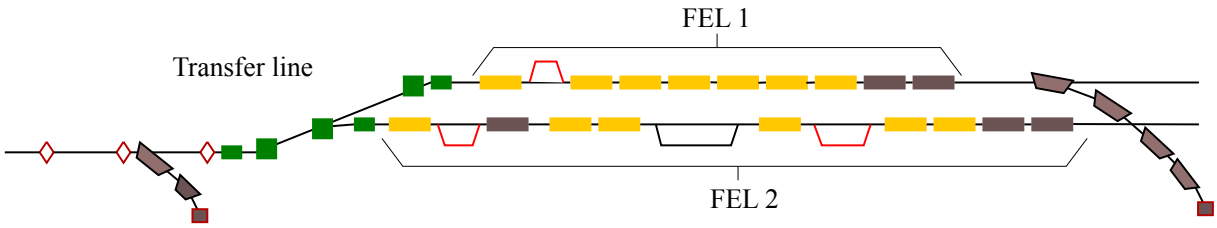

Figure 1.4: Nominal undulator layout for FEL-1 and FEL-2.

three-degree bending magnets that deflect the beam away from the linac. In the line that leads to the FEL-2 undulator, two more three-degree bend dipoles of opposite polarity bring the beam back parallel to the linac at a distance from it of 1 m. When operating the FEL-1 line, one of the afore-mentioned dipoles is switched off and the beam proceeds to a second pair of dipoles that again bend the beam parallel to the linac and displaced from it by 3 m. The two undulator lines are thus parallel and separated by 2 m. The electron optics is designed to cancel any emittance blow up due to the emission of coherent synchrotron radiation in the bends by a suitable choice of the (small) bending angles and of the phase advances between dipoles. The FERMI project is based on the principle of the high gain, harmonic generation FEL amplifier employing multiple undulators, up-shifting an initial seed signal in a single-pass. The initial (master oscillator or seed) signal is provided by a conventional pulsed laser operating at wavelengths in the region $210 - 300nm$. The energy modulation induced by the interaction of the laser with the electron beam in the first undulator (the modulator) is converted to spatial modulation by passing the beam through the magnetic field of a dispersive section. The bunching further increases the initial

bunch modulation at harmonics of the seed wavelength. Thus re-bunched, the electrons emit coherent radiation in a second undulator (the radiator) tuned at a higher harmonic corresponding to the desired FEL output. This scheme broadly describes the FEL-1 layout, down to $20nm$. To reach the shortest design wavelength of $4.2nm$, a second stage (modulator + dispersive section +radiator) is added to produce the FEL-2 configuration, as shown in Figure 1.4. FEL-1 and FEL-2 are required to provide, at all wavelengths, continuously tunable output polarization ranging from linear-horizontal to circular to linear-vertical. The FEL-1 radiator and the final radiator in FEL-2 have therefore been chosen to be of the APPLE-II, pure permanent magnets type. For the modulator a simple, linearly-polarized configuration is best, due to both its simplicity and because the input radiation seed can be linearly polarized. The wavelength will be tuned by changing the undulator gap at constant electron beam energy. After leaving the undulators, while the FEL radiation is transported to the experimental areas, the electron beam is brought to a beam dump by a sequence of bending magnets. Table 1.1 lists some of the basics parameters of the electron beam and of the FEL radiation at $20nm$ (FEL-1) and $4.2nm$ (FEL-2). Figure 1.5 shows the FEL radiation transport system, designed to handle the high peak power of up to $10GW$ in the sub-ps long pulse, including a differentially pumped windowless vacuum system and low-Z material beamline components operating at grazing incidence angles. The photon beam transport system incorporates all provisions and equipment necessary to ensure pulse length and energy resolution preservation, monochromatization, source shift compensation, beam splitting and focusing into the experimental chamber.

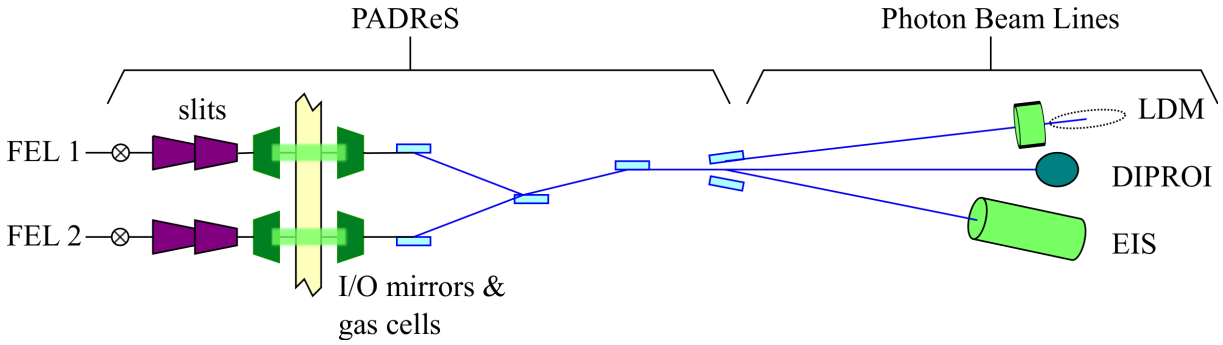

Figure 1.5: Photon beam transport system (PADReS) from the undulator to the experiment chambers. LDM: Low Density Matter, DIPROI: Diffraction and Projection Imaging, EIS: Elastic and Inelastic Scattering.

1.2 Introduction to the wakefields

In this section we give a brief introduction to a concept of wakefields and impedances for relativistic beams interacting with surrounding environment. Among the numerous publications on this subject, we refer here to the following references [3–7].
Let us consider a leading particle of charge q_l moving with velocity v, and a trailing particle of charge q_t moving behind the leading one on a parallel path at a distance s with an offset r_2, as

Table 1.1: Nominal electron beam and FEL parameters.

Parameters	Value at $20nm$	Value at $4.2nm$	Units
Electron beam energy	1.2	1.5	GeV
Peak current	800	800	A
Bunch charge	0.8	0.8	nC
Emittance (slice)	$1.0 - 1.2$	1.0	$mm\ mrad$, rms
Energy spread (slice)	$150 - 400$	150	keV
Bunch duration	$100 - 600$	$100 - 600$	fs, FWHM
Repetition rate	50	50	Hz
FEL peak power	$0.2 - 2.0$	1.7	GW
Seed power	~ 100	100	MW

shown in figure 1.6. In general, we want to find the force which the leading particle exerts on the

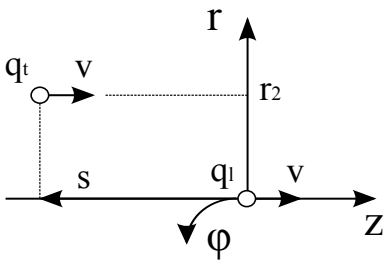

Figure 1.6: A leading point charge q_l and a trailing point charge q_t in free space. A cylindrical coordinate system is used.

trailing one. The electromagnetic field carried by a relativistic charge is Lorentz contracted into a thin disk perpendicular to the particles directions of motion and the opening angle of the field distribution is on the order of $1/\gamma$ where $\gamma = (1 - (v/c)^2)^{-1/2}$ and c is the speed of light. If let us consider the limit $v \to c$ and recalling that $s = vt - z$, we can write the electromagnetic field of the ultra-relativistic point charge q_l in free space as:

$$E_r = \frac{q}{2\pi\varepsilon_0 r}\delta(z - ct), \qquad H_\phi = \frac{E_r}{Z_0} \tag{1.1}$$

where $Z_0 = 377\Omega$ is the free space impedance. Since the electric field is perpendicular to the moving direction all other field components are identically zero both ahead and behind the leading charge and hence there are no forces on the trailing charge. We obtain the same conclusion if the particles move parallel to the axis on a perfectly conducting cylindrical pipe of arbitrary cross section since all electric field lines terminate transversely on the surface of the wall where image charges are induced. The image charge travel in synchronism with the leading charge and hence there is no electromagnetic field behind the leading charge and thus there is no interaction between the leading and trailing charges. Interaction between the particles in the ultra-relativistic limit can occur if the wall is not perfectly conducting or the pipe presents discontinuity in the surface wall which is usually due to the presence of RF cavities, flanges, bellows, beam position monitor, slots etc., in the vacuum chamber.

The electromagnetic interaction of charged particles in accelerators with the surrounding environment can be taken into account solving the Maxwell's equation to find the fields and then estimate the effects of these fields on the particle motion. In the following we assume that the system under consideration has a symmetric axis, and choose it as the z-axis of the coordinate system as indicated in figure 1.7. Let us still consider a leading particle q_l that moves in z-direction with an offset r_1 and a trailing particle q_t that travels parallel to the leading one with offset r_2 relative to the axis, as schematically indicated in figure 1.7. Furthermore the particles have the same velocity close to the speed of light, $v \approx c$. For the leading charge $z = ct$ while for the trailing charge $s = ct - z$. It is worthwhile noting that although the two particles move in vacuum, there are boundary in the problem that scatter the electromagnetic field resulting in interaction between the particles. Assuming that we solved Maxwell's equation and found the electromagnetic field

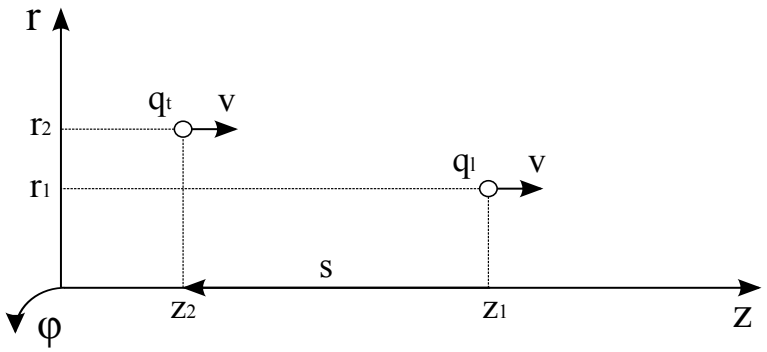

Figure 1.7: The leading point charge q_l and the trailing point charge q_t are offset relative to the axis of the chamber.

generated by the leading charge we can calculate the change of the momentum $\Delta\mathbf{p}$ of the trailing particle caused by this field as a function of the offsets distance s:

$$\Delta\mathbf{p}(r_1, r_2, s) = q_t \int_{-\infty}^{\infty} [\mathbf{E}(r_1, r_2, z, t) + c\hat{\mathbf{z}} \times \mathbf{B}(r_1, r_2, z, t)]_{z=ct-s}\, dt \tag{1.2}$$

Since the beam dynamics is different in the longitudinal and transverse directions, it is useful to separate the longitudinal momentum Δp_z from the transverse component $\Delta\mathbf{p}_\perp$. Now we can introduce the longitudinal and transverse wake functions as:

$$w(r_1, r_2, s) \triangleq \frac{c\Delta p_z}{q_l q_t} = \frac{1}{q_l} \int_{-\infty}^{\infty} [E_z]_{t=(z+s)/c}\, dz \tag{1.3}$$

$$\mathbf{w}_\perp(r_1, r_2, s) \triangleq \frac{c\Delta\mathbf{p}_\perp}{q_l q_t} = \frac{1}{q_l} \int_{-\infty}^{\infty} [\mathbf{E}_\perp + c\hat{\mathbf{z}} \times \mathbf{B}]_{t=(z+s)/c}\, dz \tag{1.4}$$

The longitudinal wake function $w(s)$ is the voltage loss experienced by the trailing particle, per unit charge of the leading particle, typically given in units $[V/pC]$ for a single structure, in $[V/pC/m]$ for a periodic one. Usually the vacuum chamber is designed so that the system axis is the ideal orbit for the beam. Deviations from it are relatively small, and both offsets r_1 and r_2 are typically much smaller than the size of the vacuum chamber. Thus, a longitudinal wake function that only depends on s can be introduced: $w(s) = w(0, 0, s)$.

In a cylindrically symmetric structure or in a vacuum chamber with symmetry elements, such as elliptical or rectangular cross section, the transverse wakefields on the axis, where $r_1 = r_2 = 0$, vanishes that is $\mathbf{w}_\perp(0,0,s) = 0$. In addition for small values of $r = r_1$ it is possible expand $\mathbf{w}_\perp(r, r_1, s)$ keeping only the lowest-order linear terms. This dominant transverse term is the scalar dipole wake function that is defined as $w_1(s) = |\mathbf{w}_\perp(r, r, s)|/r_1$ and is the dipole force experienced by the trailing particle per unit offset of the driving particle, given in $[V/pC/m]$ for a single structure, in $[V/pC/m^2]$ for a periodic one.
It is worthwhile noting that the wake functions do not propagate in front of the leading charge due to the *causality principle* that is $w(s) = 0$ and $w_1(s) = 0$ for $s < 0$. For a bunch of longitudinal charge distribution $\rho(s)$, the longitudinal wake potential $W(s)$ (the voltage lost for a test particle at position s) is given by:

$$W(s) = \int_0^\infty w(s')\rho(s - s')ds' \tag{1.5}$$

The average of the longitudinal wake potential, $\langle W \rangle$, gives the loss factor, the rms W_{rms} gives the energy spread increase: $\Delta E_{rms} = QLW_{rms}$ with Q the total bunch charge, L the length of structure in the periodic case.
In the similar way the transverse wake potential $W_1(s)$ (the transverse kick for a test particle at position s) is given by:

$$W_1(s) = \int_0^\infty w_1(s')\rho(s - s')ds' \tag{1.6}$$

The average of the transverse wake potential, $\langle W_1 \rangle$, gives the kick factor.
Knowledge of the longitudinal and transverse wake functions gives complete information about the electromagnetic interaction of the beam with its environment. In many cases it is more convenient to use the Fourier transform of the wake function that is called the impedance. Sometime it is easier to calculate the impedance for a given geometry of the structure, rather than the wake function. Knowing the impedance and using the inverse Fourier transformation the wake function can be found. The longitudinal Z and transverse Z_1 impedances are defined as Fourier transforms of the wake functions:

$$Z(k) = \frac{1}{c}\int_\infty^\infty w(s)e^{-iks}ds \tag{1.7}$$

$$Z_1(k) = \frac{1}{c}\int_{-\infty}^\infty w_1(s)e^{-iks}ds \tag{1.8}$$

The inverse Fourier transform relates the wake functions to the impedances:

$$w(s) = \frac{c}{2\pi}\int_\infty^\infty Z(k)e^{iks}dk \tag{1.9}$$

$$w_1(s) = \frac{c}{2\pi}\int_{-\infty}^\infty Z_1(k)e^{iks}dk \tag{1.10}$$

It is worthwhile noting that the wake functions can be found if only the real part of the impedance is known. After some simply manipulation and appling the causality principle we obtain:

$$w(s) = \frac{2c}{\pi}\int_0^\infty \Re Z(k)\cos(ks)dk \tag{1.11}$$

$$w_1(s) = \frac{2c}{\pi}\int_0^\infty \Re Z_1(k)\sin(ks)dk \tag{1.12}$$

There are two main effects due to the wakefields and impedances: heating and instabilities. Due to the wakefields a charged particle bunch lost energy which heats the traversed structure. We could distinguish heating effects due to short-range wakes and due to the long-range wake. Short-range wakefield effects are single bunch in a linear accelerator or single turn in a storage ring. The heating due to the single bunch energy loss does not normally give problems for structures with good thermal conductivity. Long-range wakefield effects are important if a single resonant mode is driven by successive bunches, such as in storage rings or in linac with high repetition rate.
Multi-bunch or bunch-to-bunch instabilities depend mainly on narrow resonance at frequencies below or near the cut-off of the beam pipe. Above this frequency, the electromagnetic fields can propagate out of the structure and thus will not build up resonantly. In time domain, such narrow-band resonances correspond to long-range oscillations caused by resonant modes. In linac with low repetition rate, such as FEL based on single-pass linac, could be neglected. Single bunch instabilities depend on the short-range wakefields, corresponding to wide-band impedances which occur at higher frequency. FEL operation requires a high quality beam that is simultaneously short and intense. The knowledge of the short-range wakefields that are induced in different parts of the accelerator are needed to predict the beam quality in term of the single bunch energy spread and emittance. One way of calculating short-range is to take the ratio $\sigma_z/a \ll 1$, where σ_z is the rms bunch length and a is the beam pipe radius. This condition means that the spectrum of the bunch which reaches to spatial frequency of the order of $k \approx 1/\sigma_z$ is greater than the cut-off frequency of the beam pipe. In FERMI@Elettra the ratio σ_z/a is in the range $0.003 - 0.02$ and based on this criterion the bunch in the linac and undulator region is short. In general, as a bunch become shorter the longitudinal wakefields become stronger and transverse wakefields weaker. As bunches become shorter their frequency content becomes higher, new sources of wakefields become important such as the longitudinal resistive wall wake and the longitudinal surface roughness wake. For very short bunches there can be a lag between the generation of radiation by the head of a bunch and its effect on tail particles. When a head particle passes a vacuum chamber object, such as the beginning of a cavity, that information can not arrive at the tail particle until a downstream distance $z = a^2/2s$, namely *catch-up distance*, where a is the beam pipe radius and s is the distance between the two particles. Similarly, for periodic structures, the interaction with a short bunch will have an initial transient region before the steady-state wake is reached, as can be seen in Ch. 2. For a Gaussian bunch distribution with rms length σ_z the transient regime will last $z \sim a^2/2\sigma_z$. As a bunch becomes shorter, the transient become ever more important.
The computational of wake functions and impedances for practical accelerator applications is a rather demanding task. One methods is the direct numerical solution of the Maxwell equations which is called the time domain approach. In general to assure numerical convergence the numerical calculation of the short-range wakefields requires a spatial mesh size equal to a fraction of bunch length. Thus this calculation could become for short bunch very time consuming due to the large number of mesh points required. Several numerical codes exist which perform direct calculation of the electromagnetic fields by solving the discretized Maxwell equations on a large, but finite, number of mesh points in time domain. However direct calculation of the wake function of a point charge is not possible due to its singularity. An alternative method is to first determine the impedance in frequency domain, and to obtain the wake function by an inverse Fourier transformation. To obtain good accuracy with this method at short-range time delay between leading and trailing charges we need to know the impedance up to very high frequencies.
Limitations in numerical calculations justify the development of analytical or semi-analytical meth-

ods. In the following paragraphs some important wake functions obtained by analytical methods are described.

1.2.1 Diffraction wakes

When a short bunch ($\sigma_z/a \ll 1$) passes by an abrupt change in the beam pipe, such as at the beginning of a cavity, waves begin to radiate from the corner in a manner that can be described by the diffraction theory of light. If the corner is part of a shallow step or shallow cavity Fraunhoffer diffraction applies, if it is part of a deep cavity Fresnel diffraction applies. In addition a periodic array of deep cavities is a model for a multi-cell (disk-loaded) accelerator structure. Let us consider a beam pipe of radii a and b with $b > a$ then the short-range longitudinal and transverse wake functions for a pair of shallow transitions or shallow cavity are given by [8, 9]:

$$\begin{aligned} w(s) &= \frac{Z_0 c}{\pi} \ln\left(\frac{b}{a}\right)\delta(s) \\ w_1(s) &= \frac{Z_0 c}{\pi}\left(\frac{1}{a^2} - \frac{1}{b^2}\right) \end{aligned} \tag{1.13}$$

with $Z_0 = 377\Omega$. The short-range longitudinal and transverse wake functions for a deep cavity are given by [4, 10]:

$$\begin{aligned} w(s) &= \frac{Z_0 c}{\sqrt{2}\pi^2 a}\sqrt{\frac{g}{s}} \\ w_1(s) &= \frac{2^{3/2} Z_0 c}{\pi^2 a^3}\sqrt{gs} \end{aligned} \tag{1.14}$$

where g is the gap length (see figure 1.8). Figure 1.8 shows the structure geometry for diffraction wakes. It is worthwhile to note that a cavity is considered shallow (deep) to a bunch of total length l if $g \gg (\ll)[2(b-a)^2/l]$. This is a statement that radiation, generated by the head of the bunch as it enters the cavity, can (cannot) reflect off the outer wall and return in time to meet the bunch tail. Figure 1.9 shows an array of cavities with period L, iris radius a, outer radius b and gap g whose short-range longitudinal wake was numerically obtained. Fitting this to a simple function a longitudinal wake function was obtained that is valid over a larger s range and over a useful range of structure parameters [11]:

$$w(s) = \frac{Z_0 c}{\pi a^2} e^{-\sqrt{\frac{s}{s_1}}} \tag{1.15}$$

with

$$s_1 = 0.41 \frac{a^{1.8} g^{1.6}}{L^{2.4}} \tag{1.16}$$

The result is valid for $s/L \leq 0.15$, $0.34 \leq a/L \leq 0.69$ and $0.54 \leq g/L \leq 0.89$.
As with the longitudinal case, the short-range dipole wake was obtained numerically for a set of parameters and then fit to a simple function [12]:

$$w_1 = \frac{4 Z_0 c s_2}{\pi a^4}\left[1 - \left(1 + \sqrt{\frac{s}{s_2}}\right) e^{-\sqrt{s/s_2}}\right] \tag{1.17}$$

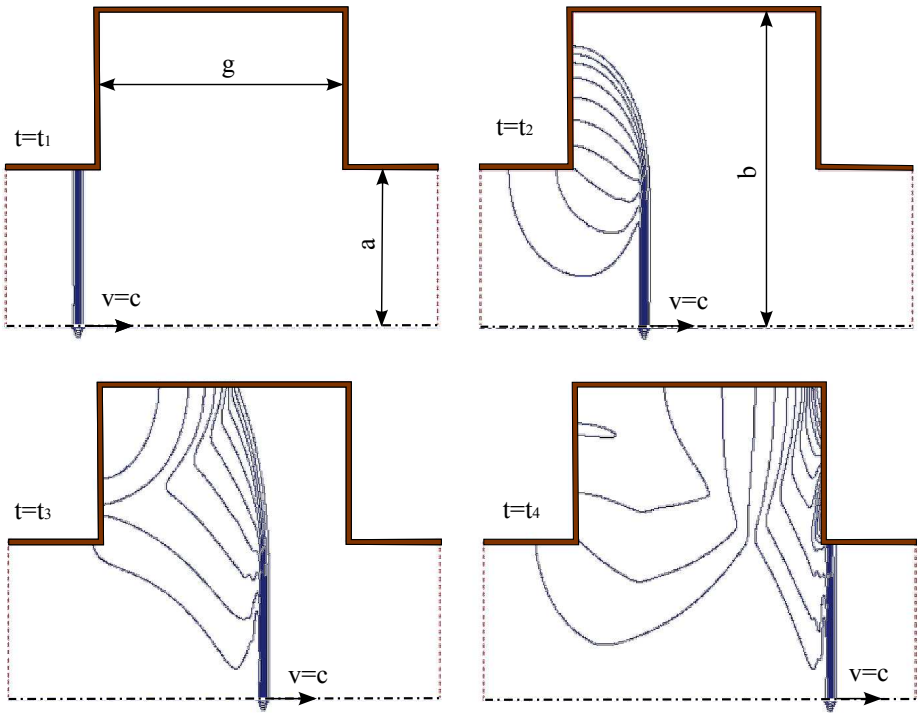

Figure 1.8: Structure geometry for diffraction wakes. a is the beam pipe radius, b and g are the outer radius and the gap of the cavity, respectively. The gaussian bunch is on-axis and the electric field lines are also indicated at four time steps.

with

$$s_2 = 0.17 \frac{a^{1.79} g^{0.38}}{L^{1.17}} \tag{1.18}$$

This formula is valid over the same parameter regime as in the longitudinal case.

1.2.2 Resistive wall wake

The impedance of a round metallic beam pipe of radius a is [4]:

$$Z(k) = \left(\frac{Z_0}{2\pi a}\right)\left[\frac{\lambda}{k} - \frac{ika}{2}\right]^{-1}, \tag{1.19}$$

where the parameter λ is given by

$$\lambda = \sqrt{\frac{Z_0 \sigma |k|}{2}}[i + sign(k)], \tag{1.20}$$

with σ the dc conductivity of the metal. Inverse Fourier transforming the impedance, one obtains the longitudinal wake function [4, 13]:

$$w(s) = \frac{4Z_0 c}{\pi a^2}\left[\frac{e^{-s/s_0}}{3}\cos\left(\frac{\sqrt{3}s}{s_0}\right) - \frac{\sqrt{2}}{\pi}\int_0^\infty \frac{x^2 e^{-x^2 s/s_0}}{x^6 + 8} dx\right] \tag{1.21}$$

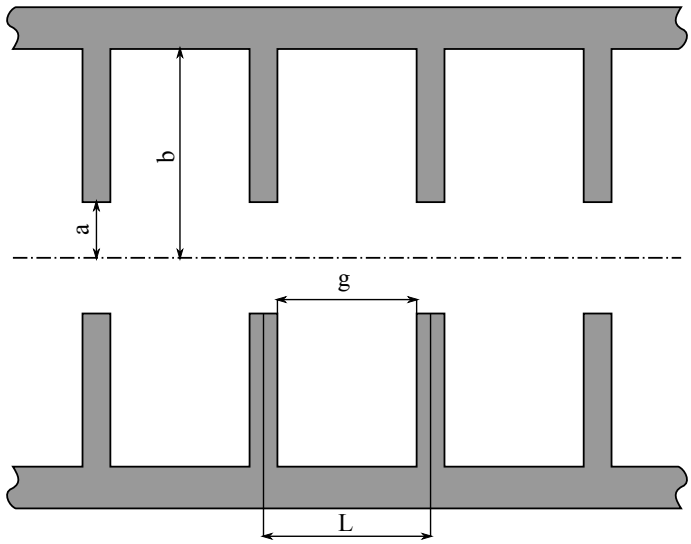

Figure 1.9: Structure geometry for a periodic array of deep cavity.

where the characteristic distance s_0 is given by

$$s_0 = \left(\frac{2a^2}{Z_0\sigma}\right)^{\frac{1}{3}} \tag{1.22}$$

For the special case of the resistive wall wake the transverse wake function can be obtained from the longitudinal wake function using:

$$w_1(s) = \frac{2}{a^2}\int_0^s w(s')ds' \tag{1.23}$$

The problem with using Eq. 1.21 for the short bunch wake is that it assumes that the conductivity of the metal wall is independent of frequency. It is believed that electrical conductivity in normal metals, up to the highest frequencies of interest, is described by the Drude-Sommerfeld free-electron model of conductivity [14, 15]. In this model the ac conductivity, a response to applied oscillating fields, is given by

$$\tilde{\sigma} = \frac{\sigma}{1 - ikc\tau} \tag{1.24}$$

with σ the dc conductivity of the metal and τ the relaxation time. The dc wake equation 1.21 is valid for $c\tau/s_0 \ll 1$.
The impedance of a parallel plates chamber is given by [15, 16]

$$Z(k) = \frac{Z_0}{4\pi}\int_{-\infty}^{\infty}\left[\frac{\lambda(k)}{k}\cosh^2(ax) - \frac{ik}{k}\cosh(ax)\sinh(ax)\right]^{-1}dx \tag{1.25}$$

where the parameter $\lambda(k)$ is the same as in Eq. 1.20, using Eq. 1.24 in case of the ac conductivity model and with a the half-gap of the parallel plates.
The wake function is obtained from the inverse Fourier trasform of the impedance that is

$$w(s) = \frac{2c}{\pi}\int_0^{\infty}\Re\Big[Z(k)\Big]\cos(ks)dk \tag{1.26}$$

1.2.3 Surface roughness wake

A possible model for the wake function of a rough surface is to consider a beam pipe with small periodic corrugations. In fact from numerical simulations of many randomly placed, small cavities on a beam pipe, in steady state, the short range longitudinal wake function is very similar to the truly periodic case [17]. Let us consider a beam pipe with small, rectangular, periodic corrugations, with h the half-depth, g the gap ($= p/2$), and p the period. In the case $h/p \gtrsim 1$ the wake is dominated by one mode of relatively low frequency ($k_0 \ll 1/h$) [18]:

$$w(s) \approx \frac{Z_0 c}{\pi a^2} \cos(k_0 s) \tag{1.27}$$

with $k_0 = 2/\sqrt{ah}$. It is worthwhile to note that the transverse wake function for this model is also given by a single mode at the same frequency.
This single resonator model is valid when the depth-to-period of the surface roughness is not small compared to 1. For a sinusoidally oscillating wall with amplitude h and period p, where $h \ll p$, the longitudinal wake function is given by [19]

$$\begin{aligned} w(s) &= \frac{Z_0 c h^2 k_1^3}{4\pi a} f(k_1 s), \\ f(\zeta) &= \frac{1}{2\sqrt{\pi}} \frac{\partial}{\partial \zeta} \frac{\cos(\zeta/2) + \sin(\zeta/2)}{\sqrt{\zeta}} \end{aligned} \tag{1.28}$$

with $k_1 = 2\pi/p$. The formula is valid for $s \gtrsim k_1 h^{4/3} a^{2/3}$.

1.3 This thesis

This thesis deals with analytical and numerical studies of the short-range longitudinal and transverse wakefields and their effects along the linac and undulator chain of the FERMI@Elettra project. Novel ideas are proposed when the formulas presented in Sec. 1.2 are no longer suitable for specific problems. In Ch. 2 we have estimated the short-range wakefields in the backward traveling wave (BTW) accelerating structure since the formulas in Eq. 1.15 and 1.17 are not valid for these structures. Each section is a backward traveling (BTW) structure composed of 162 nose cone cavities coupled magnetically. Figure 1.10 shows the evolution of the electric field in these structures and the particular shape of the iris. To calculate the effect of the longitudinal and transverse wakefields we have used the time domain numerical approach with a new implicit scheme for calculation of wake potential of short bunches in long structures. The wake potentials of the BTW structure are calculated numerically for very short bunches and analytical approximations for wake functions in short and long ranges are obtained by fitting procedures based on analytical estimations. Finally the single bunch energy spread induced by short-range longitudinal wakefields is analyzed.
In Ch. 3 we have studied these electron beam dynamics in the presence of the linac transverse wakefield.Trajectory manipulation is used to gain control of the transverse wakefield-induced instability and this technique is also validated in the presence of shot-to-shot trajectory jitter. A specific script working with Courant-Snyder variables has been written to evaluate the residual banana shape after instability suppression in the presence of shot-to-shot trajectory jitter.

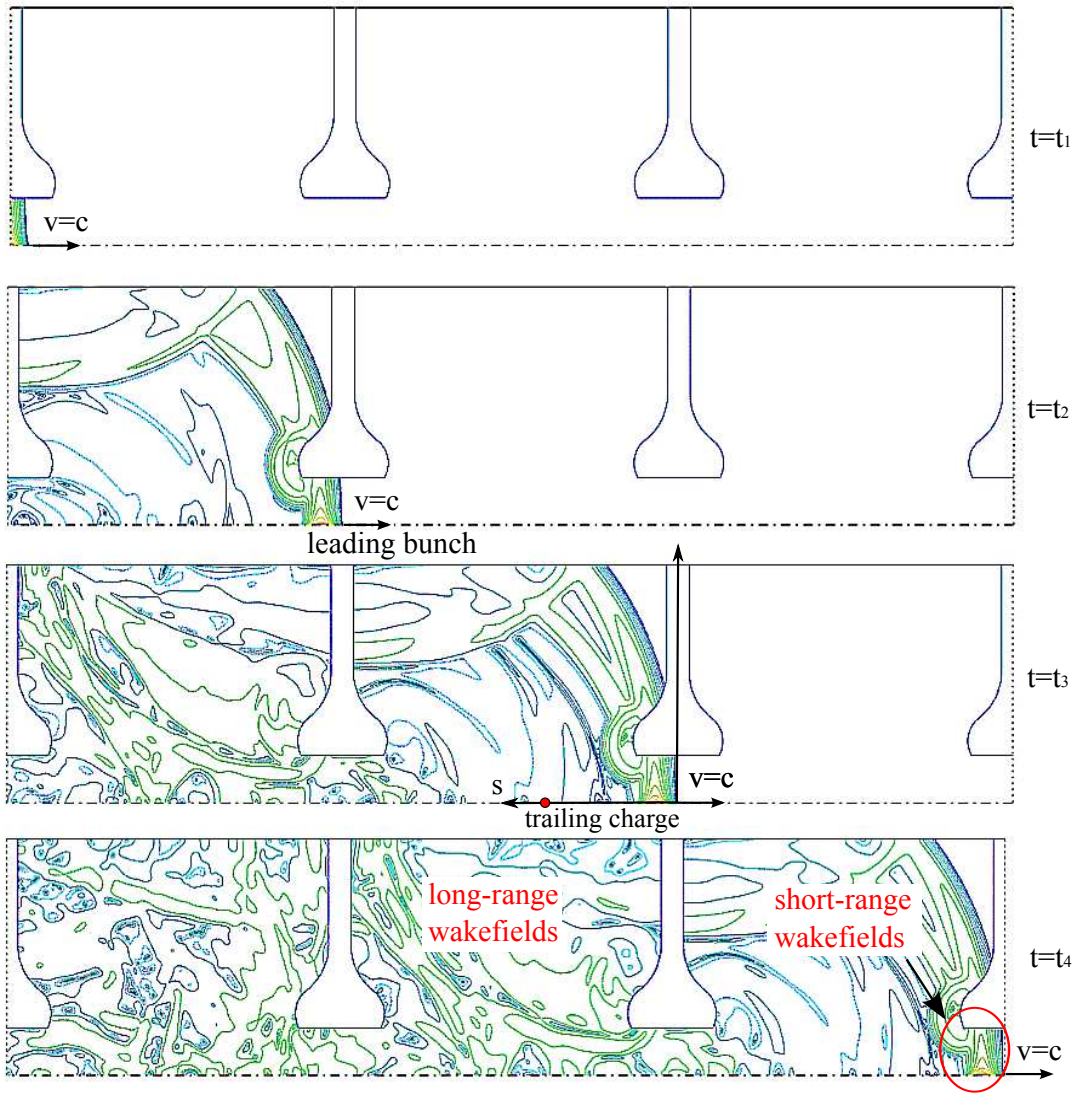

Figure 1.10: Evolution of the wakefields (electric field) in the BTW acceleration structures at four time steps.

In Ch. 4 we have analytically derived expressions for the high-frequency longitudinal and transverse resistive-wall coupling impedance of an elliptical cross-section vacuum chamber. Then, the corresponding longitudinal and transverse wake functions have been obtained by calculating numerically the inverse Fourier transforms of the impedances.
In Ch. 5 we report a novel concept to passively linearize the bunch compression process in electron linacs for the next generation X-ray free electron lasers. This can be done by using the monopole wakefields in a dielectric-lined waveguide. The optimum longitudinal voltage loss over the length of the bunch is calculated in order to compensate both the second-order RF time-curvature and

the second-order momentum compaction terms. Thus, the longitudinal phase space after the compression process is linearized up to a fourth-order term introduced by the convolution between the bunch and the monopole wake function.

1.3.1 Publications

This thesis is based on the following pubblications:

- P. Craievich, T. Weiland and I. Zagorodnov, "The short-range wakefields in the BTW accelerating structure of the ELETTRA linac," *Nucl. Inst. Meth. Phys. Res. A*, vol. 558, p. 58, 2006.
- P. Craievich, R. J. Bakker, G. D D'Auria and S. Di Mitri, "Energy spread in BTW accelerating structures at ELETTRA," in *Proc. of the 22nd Int. Lin. Accel. Conf.*, Lubeck, Germany, p. 159, 2004.
- P. Craievich, S. di Mitri, A. A. Zholents, "Analysis and control of the single bunch beam break up instability in normal conducting linacs," *Nucl. Inst. Meth. Phys. Res. A*, vol. 604, p. 457, 2009.
- S. Di Mitri and P. Craievich, "Beam break-up instability in the FERMI@ELETTRA linac," in *Proc. of the 10th Europ. Part. Accel. Conf.*, Edimburgh, UK, June 2006.
- P. Craievich and S. Di Mitri, "Emittance growth due to short-range transverse wakefields in the FERMI linac," in *Proc. of the 27th Int. FEL Conf.*, Stanford, California, 2005.
- P. Craievich, A. Lutman, R. Vescovo, "Electromagnetic field and short-range wake function in a beam pipe of elliptical cross section" *Phys. Rev. ST Accel. Beams*, vol. 11, p. 074401, 2008.
- P. Craievich et al., "Wakefield Induced Energy Spread in the FERMI Undulator", in *Proc. of the 29th Int. FEL Conference*, Novosibirsk, Russia, 2007.
- P. Craievich, "Passive longitudinal phase space linearizer," *Phys. Rev. ST Accel. Beams*, vol. 13, p. 034401, 2010.

References

[1] "FERMI@Elettra Conceptual Design Report," Sincrotrone Trieste, Tech. Rep. ST/F-TN-07/12, 2007.

[2] M. Cornacchia, S. Di Mitri, G. Penco, and A. A. Zholents, "Formation of electron bunches for harmonic cascade x-ray free electron lasers," *Phys. Rev. ST Accel. Beams*, vol. 9, p. 120701, 2006.

[3] K. L. F. Bane, "Wakefields of sub-picosecond electron bunches," *Int. J. Mod. Phys.*, vol. A22, pp. 3736–3758, 2007.

[4] A. W. Chao, *Physics of collective beam instabilities in high-energy accelerators.* New York: Wiley, 1993.

[5] B. W. Zotter and S. A. Kheifets, *Impedances and Wakes in High-Energy Particle Accelerators.* World Scientific, 1998.

[6] A. W. Chao and M. Tigner, *Handbook of accelerator physics and engineering.* World Scientific, 1999.

[7] G. V. Stupakov, "Wake and Impedance," in *JAS 2000 Accelerator School On Frontiers of Accelerator Technology: High Quality Beams*, St. Petersburg - Moscow, Russia, Jul 2000.

[8] S. A. Heifets and S. Kheifets, "Coupling impedance in modern accelerators," *Rev. Mod. Phys.*, vol. 63, pp. 631–674, 1991.

[9] E. Gianfelice and L. Palumbo, *IEEE Trans. Nucl. Sci.*, vol. 32, no. 2, p. 1084, 1990.

[10] K. L. Bane and M. Sands, "Wake fields of very short bunches in an accelerating cavity," *Part. Accel.*, vol. 25, p. 73, 1990.

[11] K. Bane, A. Mosnier, A. Novokhatski, and K. Yokoya, in *Proc. of Int. Comp. Accel. Phys. Conf.*, Monterey, California, 1998, p. 137.

[12] K. L. F. Bane, "Short range dipole wakefields in accelerating structures for the NLC," SLAC, Tech. Rep. SLAC-PUB-9663, Mar 2003.

[13] K. L. F. Bane and M. Sands, "The short-range resistive wall wakefields," *AIP Conf. Proc.*, vol. 367, pp. 131–149, 1996.

[14] E. Shiles, T. Sasaki, M. Inokuti, and D. Y. Smith, "Self-consistency and sum-rule tests in the kramers-kronig analysis of optical data: Applications to aluminum," *Phys. Rev. B*, vol. 22, no. 4, pp. 1612–1628, Aug 1980.

[15] K. L. F. Bane and G. Stupakov, "Resistive Wall Wakefield in the LCLS undulator," in *Proc. of the Part. Accel. Conf.*, Knoxville, Tennessee, USA, May 2005.

[16] H. Henke and O. Napoly, "Wake fields between two parallel resisitive plates," in *Proc. of 2nd Europ. Part. Accel. Conf.*, Nice, June 1990, p. 1046.

[17] A. Novokhatski and A. Mosnier, "Wakefields of Short Bunches in the Canal Covered with Thin Dielectric Layer," in *Proc. of the 17th IEEE Part. Accel. Conf.*, Vancouver, Canada, May 1997.

[18] K. L. F. Bane and A. Novokhatsky, "The resonator impedance model of surface roughness applied to the LCLS parameters," SLAC, Tech. Rep. SLAC-AP-117, March 1999.

[19] G. V. Stupakov, "Surface roughness impedance," in *Proc. of the 18th Advanced ICFA Beam Dynamics Workshop on the Physics of and the Science with X-Ray Free Electron Lasers*, Arcidosso, Italy, Sep 2000.

Chapter 2

Short-range wakefields in the BTW accelerating structures

Abstract
Future FEL operations in the ELETTRA LINAC require a high quality beam with an ultra short bunch. Knowledge of the short-range wakefields in the backward traveling wave (BTW) accelerating structure is needed to predict the beam quality in terms of the single bunch energy spread and emittance. To calculate the effects of the longitudinal and transverse wakefields we have used the time domain numerical approach with a new implicit scheme for the calculation of the wake potential of short bunches in long structure [1, 2]. The wake potentials of the BTW structure are calculated numerically for very short bunches and analytical approximations for wake functions in short and long ranges are obtained by fitting procedures based on analytical estimations[1] Finally the single bunch energy spread induced by short-range longitudinal wakefields is analyzed for the first phase of the project FEL-1[2].

[1]P. Craievich, T. Weiland and I. Zagorodnov *Nucl. Inst. Meth. Phys. Res. A*, vol. 558, p. 58, 2006.

[2]P. Craievich, G. DAuria, T. Weiland and I. Zagorodnov *Proceedings of the 26th International FEL Conference and 11th FEL Users Workshop*, Trieste, Italy, p. 403, 2004.

2.1 Introduction

The FERMI@ELETTRA project will use the existing ELETTRA linac. In order to increase the beam energy after the pre-injector from 100 MeV to 1.2 GeV, the linac includes seven accelerating sections. Each section is a backward traveling (BTW) structure composed of 162 nose cone cavities coupled magnetically. Furthermore, there are input and output cavities specially designed to match the structure to the RF source and load [3]. The BTW accelerating structure works with $3/4\pi$ mode chosen to optimize the structure efficiency and to achieve a simple RF tuning setup [4]. A schematic view of the BTW accelerating section geometry is shown in figure 2.1. In order to optimize the axial electrical field behavior two different nose shaped geometries are used. The structure consists of 109 type II cells and 53 type I cells. Type II cells have been designed for a higher shunt impedance value to compensate for the attenuation along the structure. The

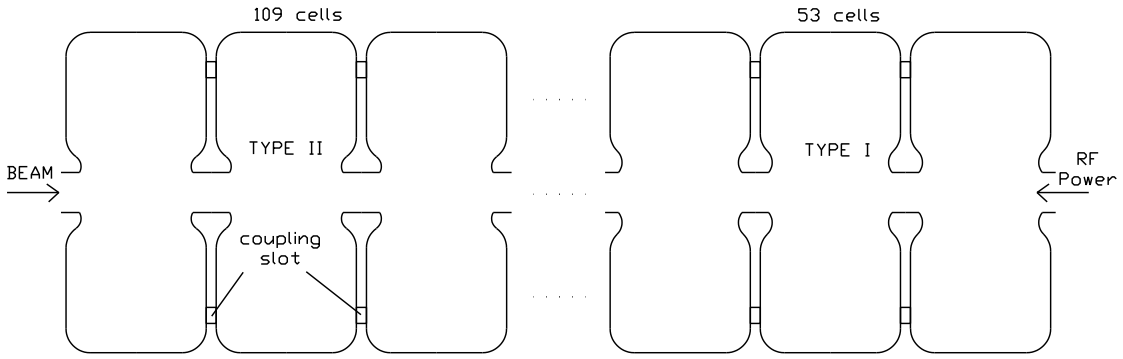

Figure 2.1: Schematic view of the BTW geometry.

input and output cells are not considered in our numerical calculations. The total length of the remaining accelerating structure is 6.075 m. The basic geometric parameters of the BTW accelerating structure are shown in figure 2.2. Here L is a period of the structure, a is an iris radius, h is a depth of the coupling slot and b is an outer radius. The structure does not have rotational symmetry because of the coupling slots. However, a short enough bunch does not see the slots and the outer walls of the cavities. The above statement is true if the following relation holds

$$\left(L + \frac{L_{bunch}}{2}\right)\frac{L_{bunch}}{2} < \Big[(b \ or \ h) - a\Big]^2 \tag{2.1}$$

where L_{bunch} is a length of the Gaussian bunch truncated at $\pm 5\sigma$. Figure 2.3 shows the dependence of the maximum height seen by the bunch from its RMS length σ. Since the FEL project requires bunches with length from $50\mu m$ to $200\mu m$, the BTW structure can be approximated with axially symmetric geometry, which allows to use 2.5D codes for wakefield calculations. The cavities in BTW accelerating structures are coupled magnetically, which demands a small iris radius compared to custom traveling wave structures. Thus, for long bunches a single cell approach to the wake potential calculation can be used. It is based on the fact that the bunch has the same field pattern before and after the cavity cell. In this case, the total energy loss in the multi-cell structure is simply a sum of the energy losses in the individual cells. However, for short bunches

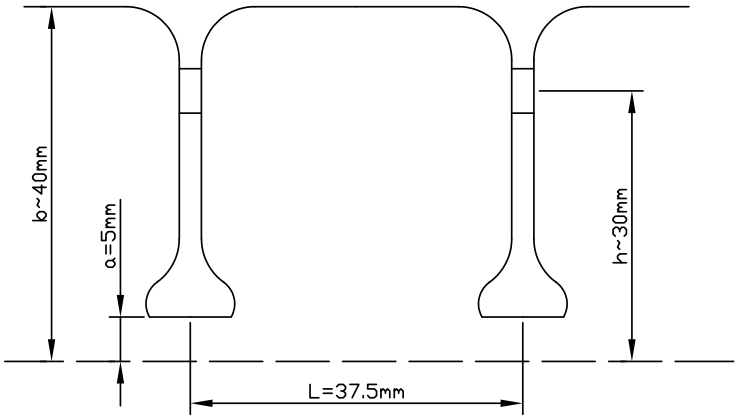

Figure 2.2: Basic dimensions of the BTW accelerating structure.

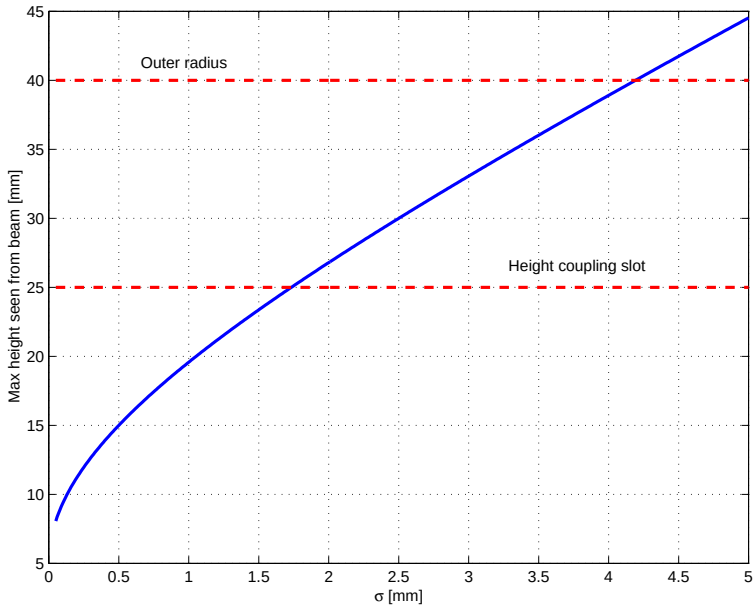

Figure 2.3: Maximum height seen from the beam vs. bunch length.

the field pattern changes drastically after a passage through the first cell and reaches a steady state regime only after several cells. The number of cells inversely inversely on the bunch length. In this paper, we estimate the behavior of the wake potentials for the complete BTW accelerating structure. We study the longitudinal and transverse cases using the time domain codes MAFIA T2 [5] and ECHO [2]. The latter uses a new implicit scheme for calculating the wake potential of short bunches in long structures [2]. We have calculated the wakefields for bunches of several lengths passing through single cell, multi-cell and complete accelerating structures. From fitting the numerical data, we have found an analytical approximation of the point charge longitudinal and transverse wake functions.

For the complete structure, the MAFIA T2 code has serious problems. The dispersion error of

the conventional FDTD algorithm leads to wrong results if a coarse mesh is used. To confirm it we have calculated longitudinal wake potentials for 20 cells of BTW structure. Figure 2.4 shows the comparison of the results calculated with MAFIA T2 (blue lines) and ECHO (red lines) codes for three bunch lengths ($50\mu m$, $120\mu m$ and $200\mu m$). The MAFIA T2 calculations are done with 20 mesh points per σ. The ECHO uses only 5 points per σ and obtains accurate results as it was checked by densening of mesh. The difference between the MAFIA T2 and ECHO results can be explained by the accumulation of the grid dispersion error [2]. Figure 2.5 shows the comparison of the longitudinal (left) and transverse (right) wake potentials obtained from code ECHO with 5 and 10 mesh steps (h) per $\sigma = 200\mu m$. We can see that ECHO indeed gives results of high accuracy with only 5 mesh points per σ. The calculated loss factors are respectively $1947.1V/pC$ for $\sigma/h = 5$ and $1947.6V/pC$ for $\sigma/h = 10$. The calculated kick factors are respectively $30.7V/pC/mm$ for $\sigma/h = 5$ and $30.6V/pC/mm$ for $\sigma/h = 10$. The dispersion error in the MAFIA code can be

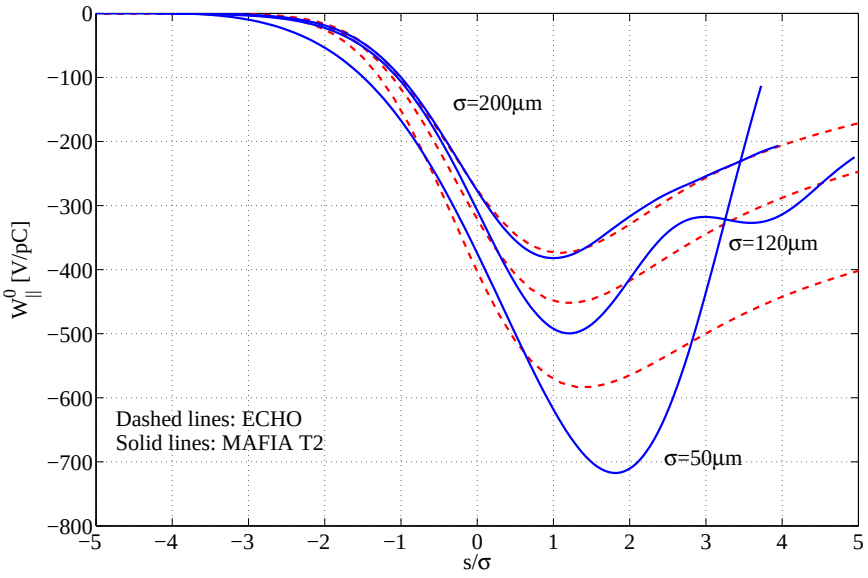

Figure 2.4: Comparison of MAFIA (dashed lines) and ECHO (solid lines) wake potential calculations.

suppressed if the following condition [6] holds:

$$\frac{\Delta z^2 \cdot L}{\sigma^3} \leq 1 \tag{2.2}$$

where Δz is a mesh size in the bunch path direction, L is a total length of the structure and σ is a bunch length. With L=6.075m and $\sigma = 50\mu m$ the required mesh size Δz has to be less than $0.14\mu m$ and enormous computational resources are needed. On the other hand, the ECHO code obtains accurate results with only 5 points per σ which allows to carry out the calculation on only custom personal computer.

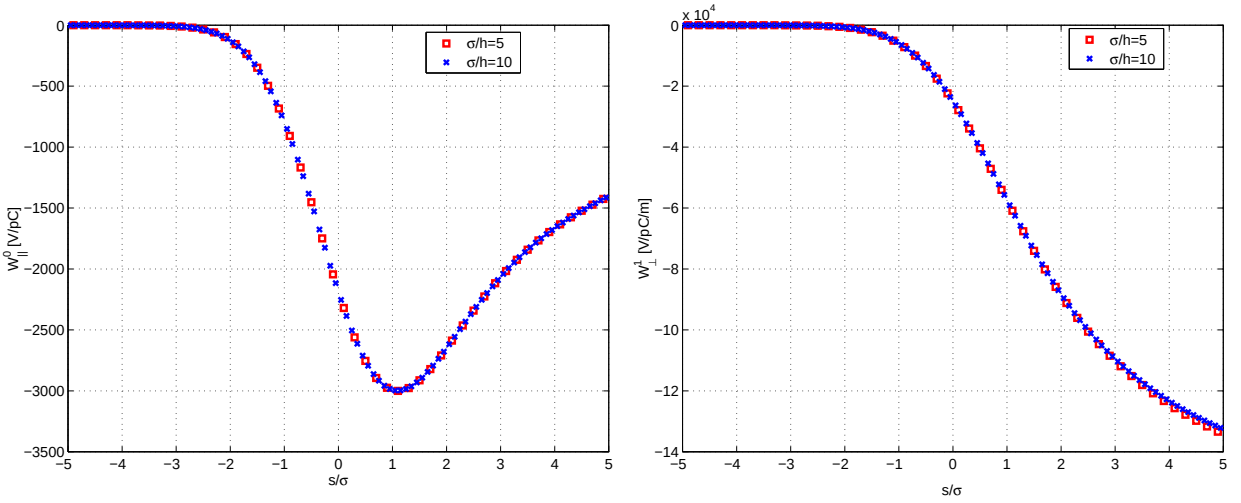

Figure 2.5: Comparison of the longitudinal (left) and transverse (right) wake potentials for the bunch with $\sigma = 200\mu m$ obtained with several mesh resolutions using ECHO (h is the mesh step).

2.2 Analytical estimations

In this section definitions and formulas used for estimation of wake functions have been collected. Let us consider an ultra-relativistic Gaussian bunch with longitudinal distribution $q(s)$ and charge Q. It travels parallel to the axis of the axially symmetric structure. The electromagnetic field of the charge bunch interacts with the surrounding accelerating structure generating the wakefields that act back on the bunch itself. If the bunch travels near to the axis, the longitudinal loss factor, dominated by monopole fields, is

$$K_{\parallel} \cong \langle W_{\parallel}^0 \rangle = \frac{1}{Q} \int_{-\infty}^{\infty} W_{\parallel}^0(s) q(s) ds \tag{2.3}$$

and the transverse kick factor, dominated by dipole fields, is

$$K_{\perp} \cong \langle W_{\perp}^1 \rangle = \frac{1}{Q} \int_{-\infty}^{\infty} W_{\perp}^1(s) q(s) ds \tag{2.4}$$

where $W_{||}^0(s)$ and $W_{\perp}^1(s)$ are respectively the longitudinal and transverse wake potentials generated by the bunch. The wake potentials can be derived from the point charge wake function $w_{||}^0(s)$ and $w_{\perp}^1(s)$ and by convolution with the charge distribution $q(s)$:

$$W_{\parallel}^0(s) = \frac{1}{Q} \int_{-\infty}^{s} w_{\parallel}^0(s - s') q(s') ds' \tag{2.5}$$

$$W_{\perp}^1(s) = \frac{1}{Q} \int_{-\infty}^{s} w_{\perp}^1(s - s') q(s') ds' \tag{2.6}$$

Short bunches interact with single cavity and periodic structures in a different way. This difference can be important if the bunch length σ is small compared to the iris radius.

In a single cavity for short bunches the wake functions are [7](for s small):

$$w_{\parallel}^{0}(s) = \frac{Z_0 c}{\sqrt{2}\pi^2 a}\sqrt{\frac{g}{s}} \tag{2.7}$$

$$w_{\perp}^{1}(s) = \frac{2}{a^2}\frac{\sqrt{2}Z_0 c}{\pi^2 a}\sqrt{gs} \tag{2.8}$$

where a is an iris radius, g is a cavity gap, Z_0 is the resistance of free space and c is the speed of light. In a periodic structure the wake functions are [8](for s small):

$$w_{\parallel}^{0}(s) = A\frac{Z_0 c}{\pi a^2}e^{-\sqrt{\frac{s}{s_0}}} \tag{2.9}$$

$$w_{\perp}^{1}(s) = \frac{2}{a^2}A\frac{Z_0 c}{\pi a^2}2s_1[1-(1+\sqrt{\frac{s}{s_1}})e^{-\sqrt{\frac{s}{s_1}}}] \tag{2.10}$$

where A, s_0 and s_1 are fitting parameters.
The wake potentials of the Gaussian bunch with severa bunch lengths are calculated up to $50\mu m$ for single-cell, multi-cell and complete BTW accelerating structures. From the fit of the numerical data to the above formulas, analytical approximations of the point charge wake functions can be obtained. The fit is done by minimizing the sum of the relative mean square deviations of the loss factors and energy spreads (analytical from the numerical) regarding the coefficients in the analytical formula.

2.3 Single-Cell Structure

In this section the wakefields in a single type II cell are studied. Figures 2.6 and 2.7 show the longitudinal and transverse wake potentials (blue lines) calculated with MAFIA T2. The mesh size Δz in the longitudinal direction fulfills the relation (2.2) for each bunch length (i.e. with $\sigma = 50\mu m$, $\Delta z = 1\mu m$). From the fit of the numerical data to relations (2.7) and (2.8) we obtain the analytical expressions approximating the point charge wake functions:

$$w_{\parallel}^{0}(s) = 0.249 \cdot \sqrt{\frac{1}{s}} \qquad [V/pC] \qquad 0 < s \leq 1.5mm \tag{2.11}$$

$$w_{\perp}^{1}(s) = 40000 \cdot \sqrt{s} \qquad [V/pC/m] \qquad 0 < s \leq 0.3mm \tag{2.12}$$

From figures 2.6 and 2.7 it can be seen that the longitudinal wake function fits the data better than the transversal one.
Figure 2.28 (left) shows the numerical (boxes) and analytical loss factor (blue line) and energy spread (red line) as functions of bunch length σ. It can be seen that the longitudinal loss factor varies as $\sigma^{-0.5}$ when σ approaches zero. In figure 2.28 (right) the transversal kick and kick spread are shown. The transversal kick factor varies as $\sigma^{0.5}$ when σ approaches zero. In table 2.1 the numerical and analytical values are compared. The analytical ones are obtained from the formulas (2.3) and (4.36) using the analytical wake functions (2.11) and (2.12). There is a good coincidence for the longitudinal case while for the transversal case the errors increase with bunch length.
To get a comparison of the computer codes used, we have calculated the wakes on the same BTW

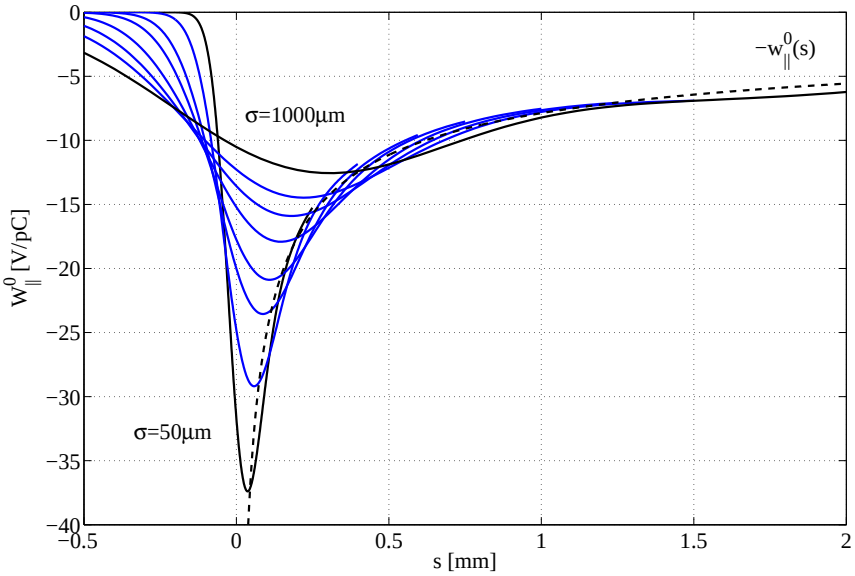

Figure 2.6: Longitudinal wake potentials (solid lines) and the longitudinal wake function (black dashed line)

.

single type II cell. Figure 2.9 shows the longitudinal (left) and transverse (right) wake potentials for several bunch lengths calculated with MAFIA T2 (blue crosses) and ECHO (red boxes). In the longitudinal case, the difference between the MAFIA T2 and ECHO results is below 0.2%. In the transverse case, the difference does not exceed 3%. The code ECHO uses 5 points for each σ while MAFIA T2 uses 50 points for $\sigma = 50\mu m$, 24 points for $\sigma = 120\mu m$ and 16 points for $\sigma = 200\mu m$ to respect the relation (2.2).

Table 2.1: Comparison of the numerical and analytical loss factors and kick factors.

σ $[\mu m]$	Numerical Loss Factor $[V/pC]$	Analytical Loss Factor $[V/pC]$	Error [%]	Numerical Kick Factor $[V/pC/m]$	Analytical Kick Factor $[V/pC/m]$	Error [%]
50	26.54	25.47	4.0	143.46	138.37	3.6
80	20.74	20.13	2.9	178.58	174.90	2.1
120	16.72	16.44	1.7	214.86	214.42	0.3
150	14.83	14.70	0.9	236.93	239.49	1.1
200	12.73	12.73	0.0	268.87	276.54	2.9
250	11.33	11.39	0.5	294.95	309.18	4.8
300	10.28	10.40	1.1	317.79	338.69	6.6
400	8.86	9.00	1.6	355.43	391.08	10.0

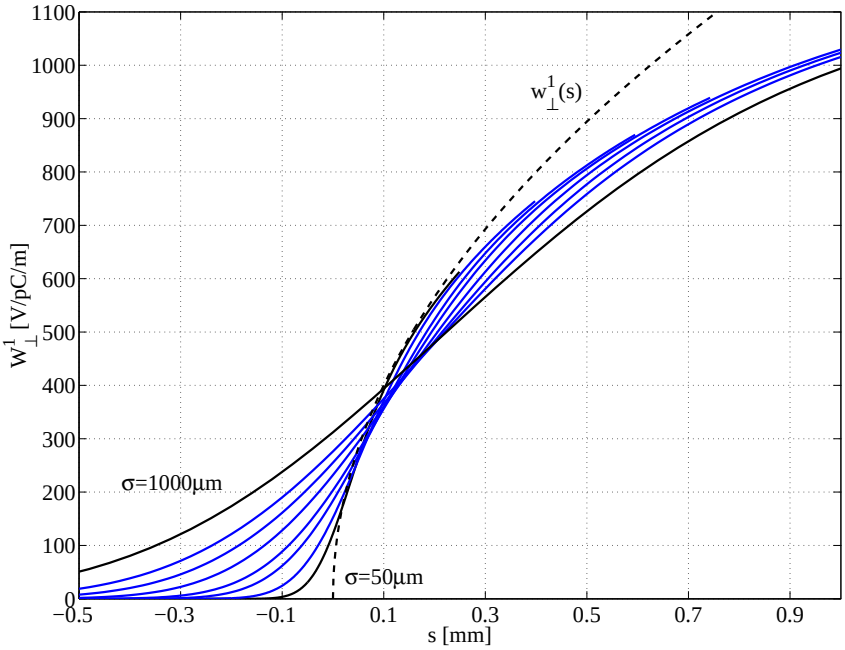

Figure 2.7: Transverse wake potentilas (solid lines) and transverse wake function (black dashed line).

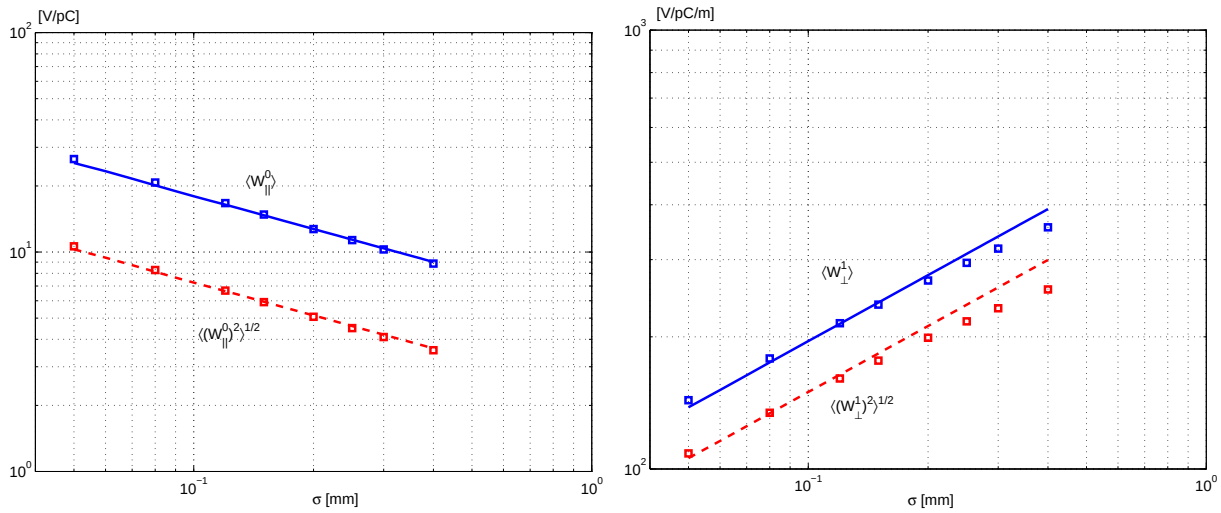

Figure 2.8: Left: comparison of numerical (box) and analytical (line) loss factor $\langle W_{||}^0 \rangle$ and energy spread $\langle (W_{||}^0)^2 \rangle^{1/2}$ as functions of bunch length σ. Right: comparison of numerical (box) and analytical (line) kick factor $\langle W_{\perp}^1 \rangle$ and kick spread $\langle (W_{\perp}^1)^2 \rangle^{1/2}$ for BTW single cell type II.

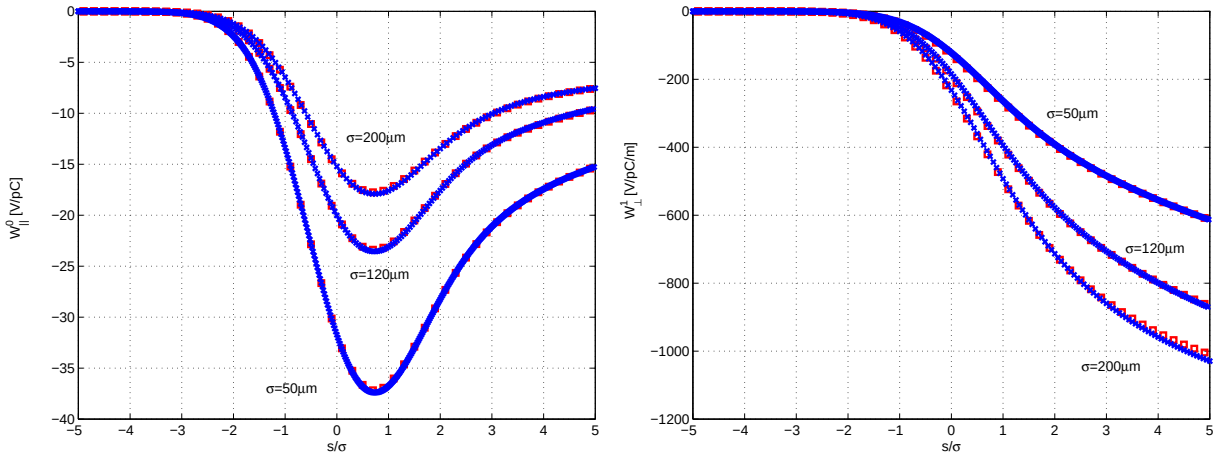

Figure 2.9: Longitudinal (left) and transverse (right) wake potentials for several bunch lengths calculated by MAFIA T2 (blue crosses) and ECHO (red boxes).

2.4 Multi-Cell Structure

In this section we have studied the evolution of the wakefields generated by a short bunch passing through the multi-cell structure which is composed by repeating type II cells. As usual, the structure is supplied by infinitely long ingoing and outgoing tubes. In this structure the wake filed pattern of the first cell changes as the bunch passes along the structure and gradually reaches the steady state form. The number of cells determining the transition between the single cell and the periodic solution for a given bunch length σ can be estimated by the expression

$$N = \frac{L_c}{L} = \frac{a^2}{2\sigma L} \tag{2.13}$$

where L_c is a "catch-up" length and L is a period of the structure. After the bunch has crossed the N cells, we can obtain the wake potential of remaining cells from the steady state solution. Code MAFIA T2 is used to study the steady state solution in the multi-cell structures with bunch length $\sigma = 200\mu m$. Figure 2.10 shows modification of the longitudinal wake potential (left), the loss factor and energy spread (right) along the first 10 cells. The loss factor converges to the steady state value after ~ 3 cells while for the stabilization of the wake potentials ~ 7 cells are needed. Figure 2.11 shows modification of the transverse wake potentials (left), the kick factor and kick spread (right) along the first 10 cells. In this case, at least 10 cells are needed for the kick factor convergence and stabilization of the wake potential.

2.5 Longitudinal wake function

In this section we study the longitudinal wakefields of the complete BTW accelerating structure. The code ECHO is used. Figure 2.12 shows the calculated longitudinal wake potentials (solid lines) for several bunch lengths σ. To find an analytical approximation of the wake function, we have chosen a combination of periodic (2.9) and one cell dependence (2.7) since the BTW

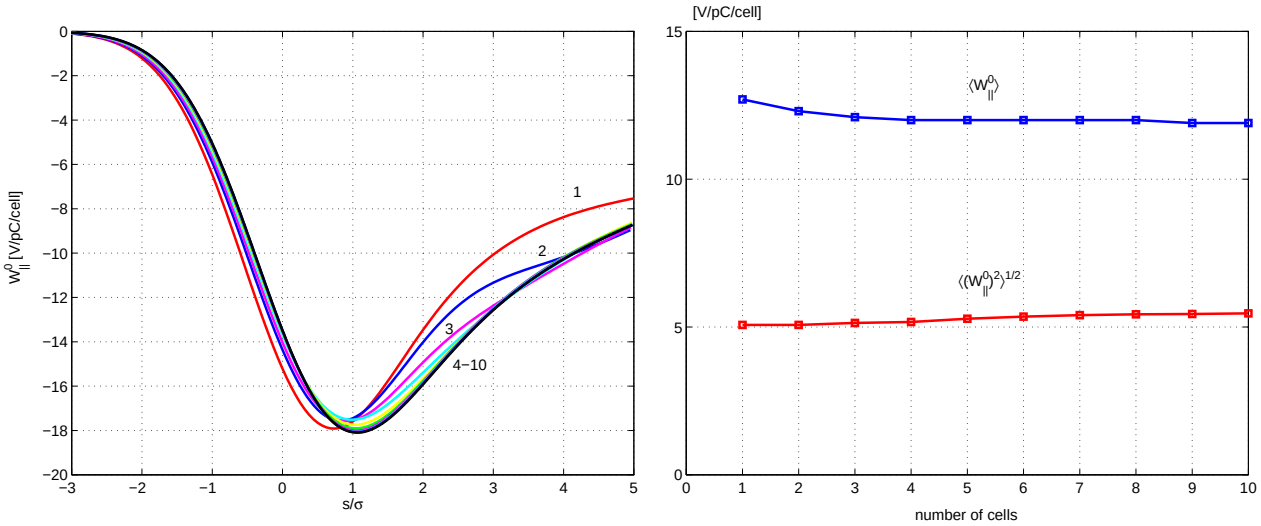

Figure 2.10: Modification of the longitudinal wake potentials (left) and the loss factor and energy spread (right) for $\sigma = 200\mu m$ in the multi-cell structure.

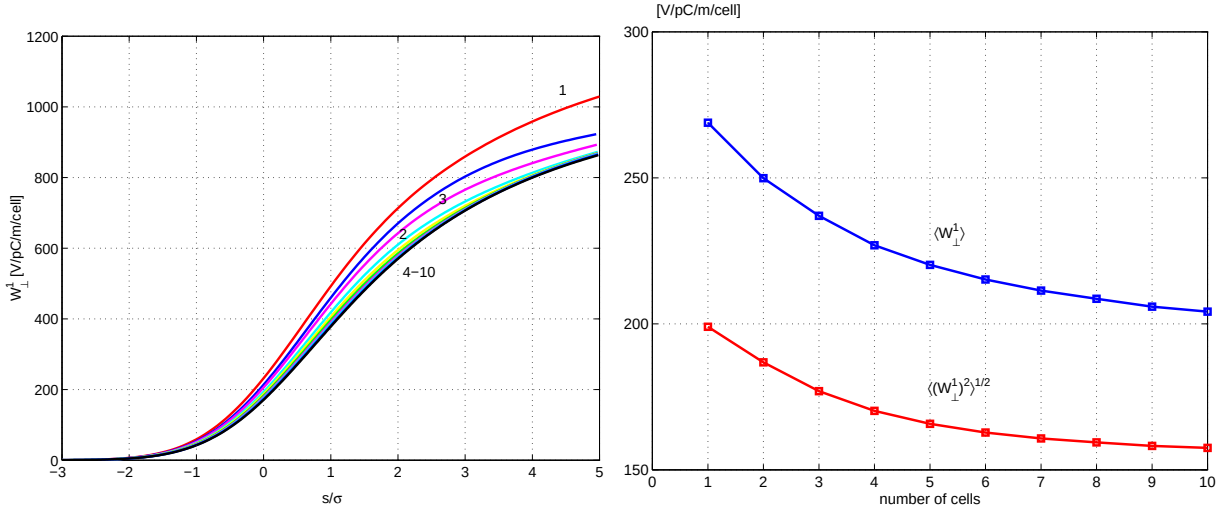

Figure 2.11: Modification of the transverse wake potentials (left) and the kick factor and kick spread (right) for $\sigma = 200\mu m$ in the multi-cell structure.

structure can be treated as a periodic structure of finite length. From the fit of the numerical wake potentials we obtain an analytical expression approximating the wake function:

$$w_\parallel^0(s) = 7300 \cdot e^{-\sqrt{\frac{s}{3.2 \cdot 10^{-4}}}} + \frac{3.4}{\sqrt{s}} \quad [V/pC] \qquad 0 < s \leq 1.5mm \tag{2.14}$$

Figure 2.12 shows the longitudinal wake function (2.14),which for small s tends to be an envelope function to the wakes. Figure 2.13 plots the numerical (box) and analytical (line) loss factor (blue) and energy spread (red) as a function of bunch length σ. Figure 2.14 presents the calculated

longitudinal wake potentials (blue solid lines) together with analytical approximations (2.14) (red dashed lines). In Figure 13 the coincidence of the numerical and analytical loss factors and

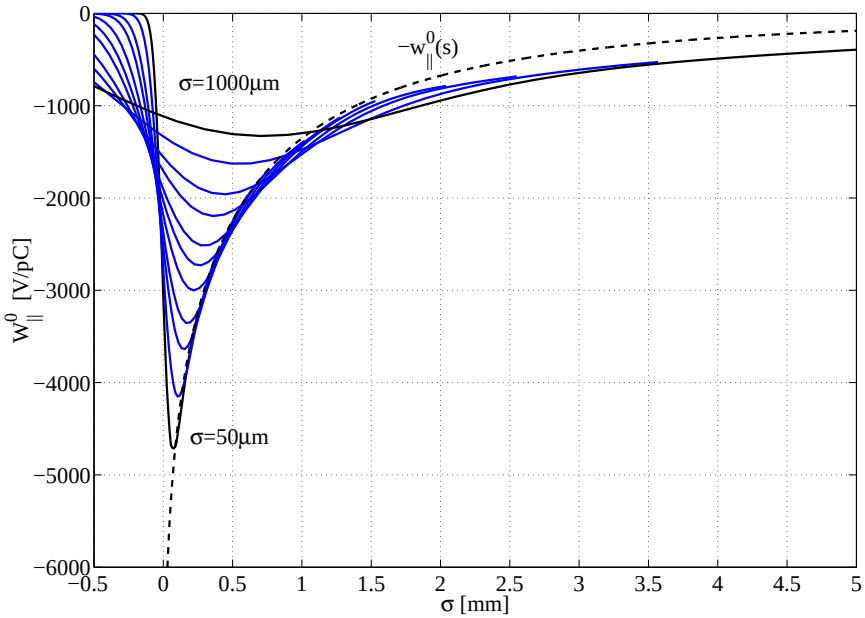

Figure 2.12: Longitudinal wake potentials (solid lines) and longitudinal wake function (black dashed line) of the BTW structure.

energy spreads can be seen. However, the "analytical" wake potentials fit the numerical results only up to $1.5mm$ (see Figures 2.12 and 2.14). To find an analytical approximation up to $5mm$, we have added to expression (2.14) an additional term with $\sqrt{s}$ dependence. From the fit of the numerical wake potentials the following analytical expression was obtained

$$w_{\parallel}^{0}(s) = 7450 \cdot e^{-\sqrt{\frac{s}{3\cdot 10^{-4}}}} + \frac{3}{\sqrt{s}} + 3000\sqrt{s} \quad [V/pC] \qquad 0 < s \leq 5mm \qquad (2.15)$$

It approximates the longitudinal wake function on a wider range compared to expression (2.14). Figure 2.15 shows the calculated wake potentials (solid lines) together with the longitudinal wake function (2.15). The wake function tends to be an envelope function to the wakes up to $5mm$. Figure 2.16 shows the numerical (boxes) and analytical loss factor (blue line) and energy spread (red line) as a function of bunch length σ. Figure 2.17 presents the calculated longitudinal wake potentials (blue solid lines) together with analytical approximations (2.15) (red dashed lines). It can be seen from Figures 2.15 and 2.17 that the analytical expression (2.15) approximates very well the longitudinal wake function up to $5mm$. In Table 2 we compare the numerical values of loss factors with analytical ones obtained from analytical expression (2.14) and (2.15). It can be seen that the relative errors are below 0.6% for analytical expression (2.14) and do not exceed 1.4% for the analytical expression (2.15). To estimate long-range wakefields, the wake potential for a Gaussian bunch with $\sigma = 5mm$ is calculated for a distance up to 2 meters after the bunch. The calculation is carried out with code ECHO for complete $\sim 6m$ long BTW structure. The long-

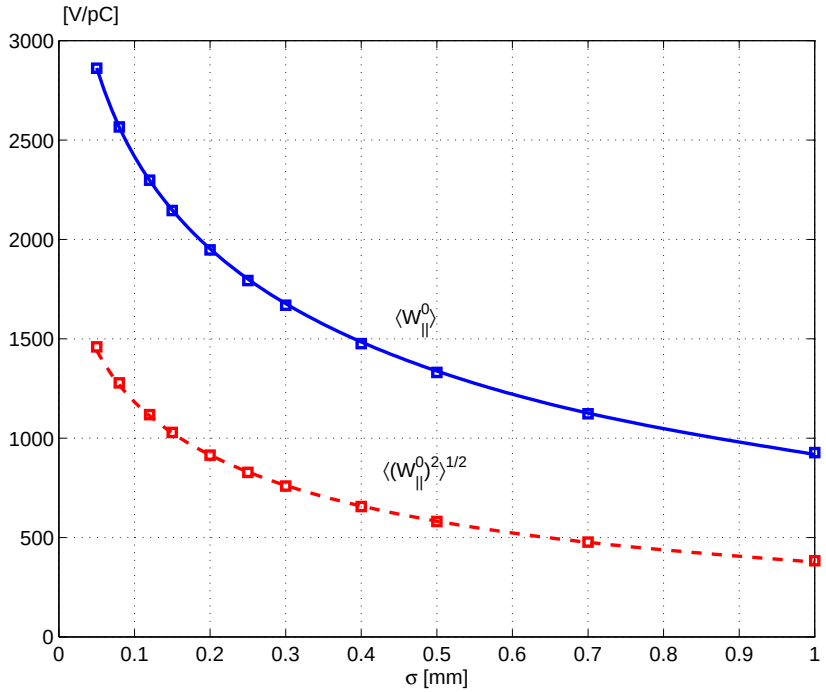

Figure 2.13: Comparison of numerical (box) and analytical (line) loss factor $\langle W_{||}^{0} \rangle$ and energy spread $\langle (W_{||}^{0})^{2} \rangle^{1/2}$ as functions of bunch length σ.

Table 2.2: Comparison of the numerical and analytical loss factors. Analytical loss factors 1 are calculated using the wake function (2.14) while analytical loss factors 2 are calculated using the wake function with additional addend (2.15).

σ $[\mu m]$	Numerical Loss Factor $[V/pC]$	Analytical Loss Factor 1 $[V/pC]$	Error [%]	Analytical Loss Factor 2 $[V/pC]$	Error [%]
50	2861.7	2863.2	0.1	2854.3	0.3
80	2565.9	2564.0	0.1	2557.9	0.3
120	2298.3	2297.5	0.0	2293.0	0.2
150	2145.5	2147.8	0.1	2144.2	0.1
200	1947.1	1952.9	0.3	1950.5	0.2
250	1793.4	1801.0	0.4	1800.0	0.4
300	1669.0	1677.3	0.5	1677.6	0.5
400	1475.7	1484.3	0.6	1487.6	0.8
500	1330.8	1338.1	0.5	1344.3	1.0
700	1123.1	1126.5	0.3	1138.8	1.4
1000	927.5	918.7	1.0	938.5	1.3

range wake function may be considered as a superposition of the contributions of the individual modes. Hence, the following expression should approximate the long-range longitudinal wake

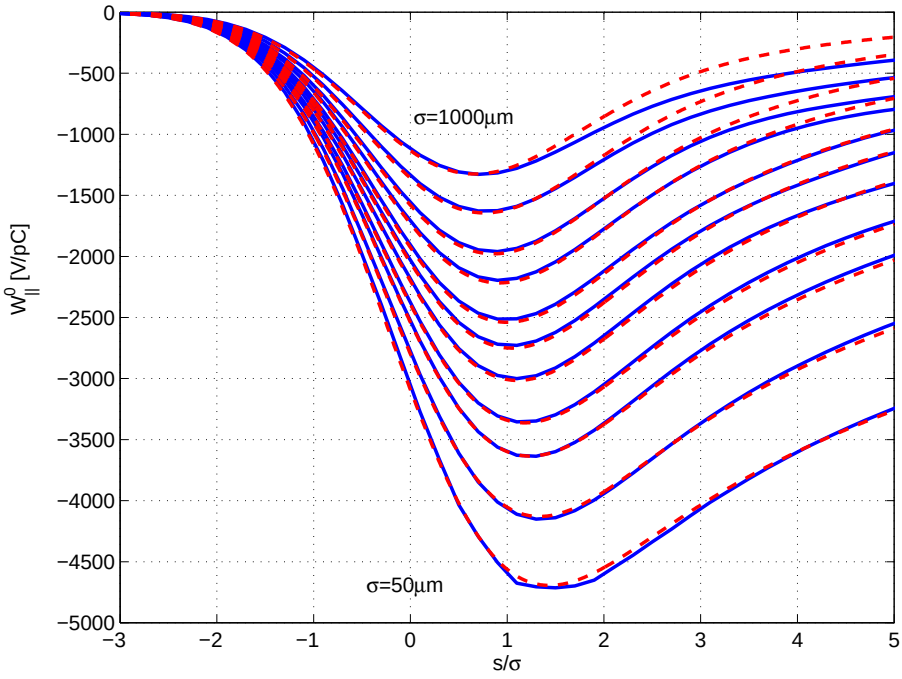

Figure 2.14: Longitudinal numerical (solid lines) and analytical (dashed lines) wake potentials of BTW structure.

function:

$$w_{\parallel}(s) = -\theta(s)[2\sum_{i=1}^{\infty} K_{i,II}\cos(\frac{2\pi}{c} f_{i,II} s)] - \theta(s)[2\sum_{i=1}^{\infty} K_{i,I}\cos(\frac{2\pi}{c} f_{i,I} s)] \tag{2.16}$$

where $K_{i,II}$ and $K_{i,I}$ are modal loss factors of type II and type I cells, respectively. The modal loss factors have been calculated in frequency domain with MAFIA solver for one cell. To obtain an approximation of the long-range wake function we only keep in (2.16) a finite number (N=11) of addends corresponding to the lowest frequencies. The results are shown in table 2.3 and figure 2.18. Figure 2.19 shows the long-range numerical (black solid line) and "analytical" (2.16) (red

Table 2.3: The lowest frequencies and their amplitudies for long-range transverse wake function in the BTW structure obtained from the MAFIA eigenmode solver.

$f_{i,II}$	[GHz]	2.98	5.38	6.79	8.25	9.36	10.72
$K_{i,II}$	[V/pC]	123.52	31.27	44.23	75.54	9.97	9.77
$f_{i,II}$	[GHz]	11.63	11.93	13.62	14.46	14.69	
$K_{i,II}$	[V/pC]	13.04	24.81	1.55	40.71	12.34	
$f_{i,I}$	[GHz]	3.00	5.41	6.87	8.38	9.36	10.87
$K_{i,I}$	[V/pC]	57.92	15.58	18.68	35.95	4.73	6.60
$f_{i,I}$	[GHz]	11.64	12.03	13.68	14.60	14.66	
$K_{i,I}$	[V/pC]	6.78	9.76	0.95	24.51	4.57	

dashed line) longitudinal wake potentials for the Gaussian bunch with RMS length $\sigma = 5mm$. An

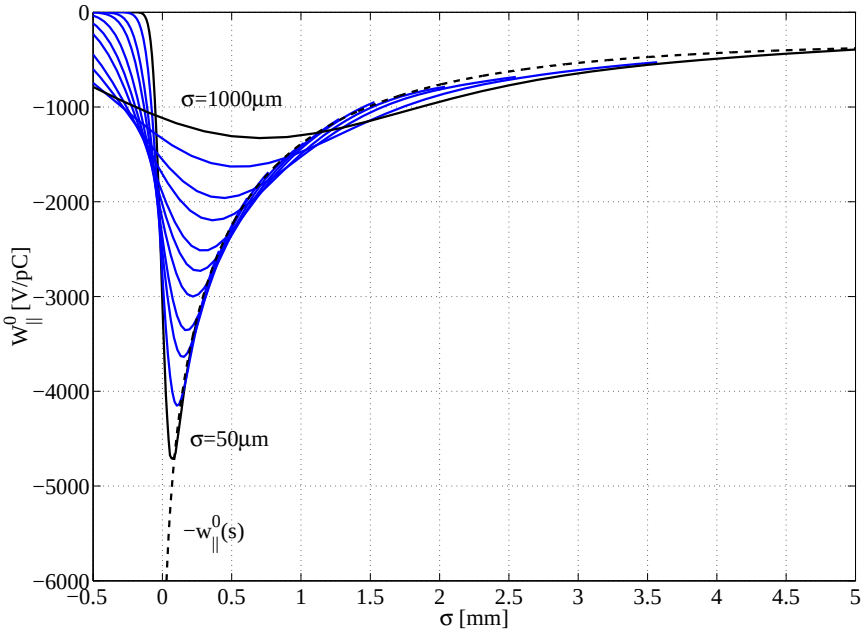

Figure 2.15: Longitudinal wake potentials (solid lines) and longitudinal wake function (black dashed line) with additional addend of the BTW structure.

excellent coincidence of the curves can be seen.
As an alternative method to modal loss calculations, a direct analysis of the numerical wake potential can be used. The longitudinal wake function is approximated by expression

$$w_{\parallel}(s) = -\theta(s)2\sum_{i=1}^{\infty} K_i \cos(\frac{2\pi}{c} f_i s) \tag{2.17}$$

where the frequencies and amplitudes are obtained using the Prony-Pisarenko algorithm [9] and are shown in table 2.4. The Prony-Pisarenko algorithm is a method to fit a set of decaying oscillation characterized by amplitudes, phases and damping constants to a given curve or data set and it is used in this example as alternative to the discrete Fourier transformation. A very

Table 2.4: The lowest frequencies and their amplitudies for long-range longitudinal wake function of the BTW structure obtained with the help of Prony-Pisarenko method applied to the wake potential (f_i in GHz and K_i in [V/pC]).

f_i	2.98	3.00	5.38	5.41	6.77	6.85	8.24	8.37	9.36	10.68
K_i	123.18	57.84	32.24	15.57	37.14	14.46	75.69	35.73	14.48	9.65
f_i	10.82	11.61	11.86	12.00	14.38	14.59	16.51	17.32	17.68	20.22
K_i	6.44	23.11	26.09	8.19	33.11	25.04	14.08	21.31	21.51	30.90

good agreement between the data sets of the tables 2.3 and 2.4 can be seen. The frequencies in table 2.4 retain their splitting between different cells type as it is explicitly shown in table 2.3.

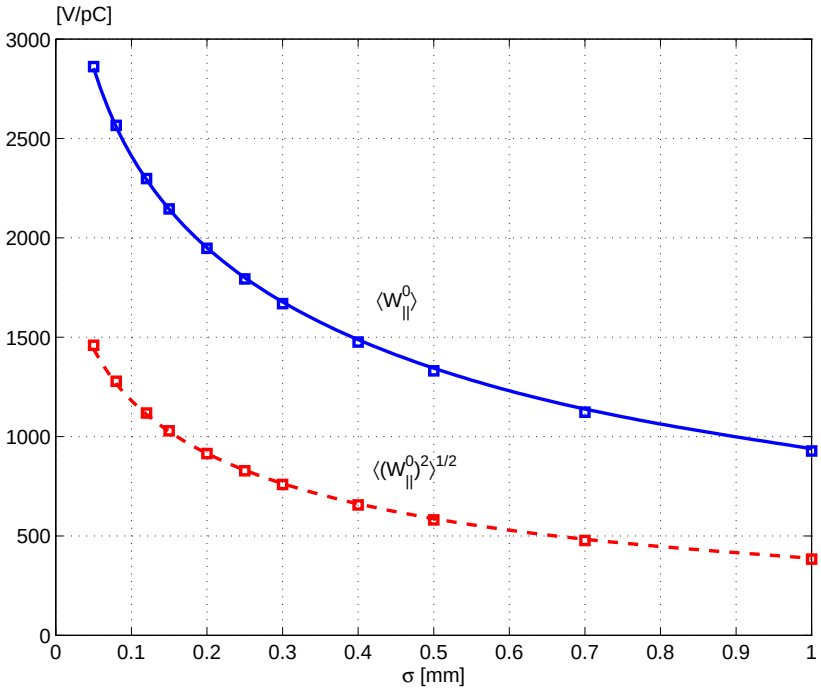

Figure 2.16: Comparison of numerical (box) and analytical (line) loss factor $\langle W_{||}^0 \rangle$ and energy spread $\langle (W_{||}^0)^2 \rangle^{1/2}$ as functions of bunch length σ.

2.6 Transverse wake function

In this section the transverse wakefields of the complete BTW accelerating structure are studied. The numerical results are obtained with code ECHO. Figure 2.20 shows the calculated transverse wake potentials (solid lines) for several bunch length σ. To find an analytical approximation for the transverse wake function a combination of periodic (2.10) and one cell dependence (2.8) was chosen. As in the longitudinal case, in this analytical model the BTW structure is treated as a periodic structure of finite length. From the fit of numerical wake potentials to the analytical model the analytical expression for the wake function is obtained (for $0 < s \leq 2mm$):

$$w_{\perp}^{1}(s) \quad = \quad 1.7 \cdot 10^5 [1 - (1 + \sqrt{\frac{s}{1.2 \cdot 10^{-4}}}) \cdot e^{-\sqrt{\frac{s}{1.2 \cdot 10^{-4}}}}] + 8.5 \cdot 10^4 \cdot \sqrt{s} \, [\frac{V}{pC \cdot m}] \qquad (2.18)$$

Figure 2.20 shows the transverse wake function (2.18), which tends to be an envelope function to the wakes up to distance $s = 2mm$ after the bunch center. Figure 2.21 presents the numerical (box) and analytical kick factor (blue line) and kick spread (red line) as functions of bunch length σ. Figure 2.22 plots the calculated transverse wake potentials (blue solid lines) together with the analytical approximation (2.18)(red dashed lines). For transverse case no additional term is introduced and the wake function fits the results up to $2mm$.
In Table 2.5 we compare the numerical results with analytical ones obtained from the expression (2.18). It can be seen that the relative error does not exceed 0.7%. To estimate the long-range transverse wakefields, the wake potential for a Gaussian bunch with $\sigma = 5mm$ is calculated for

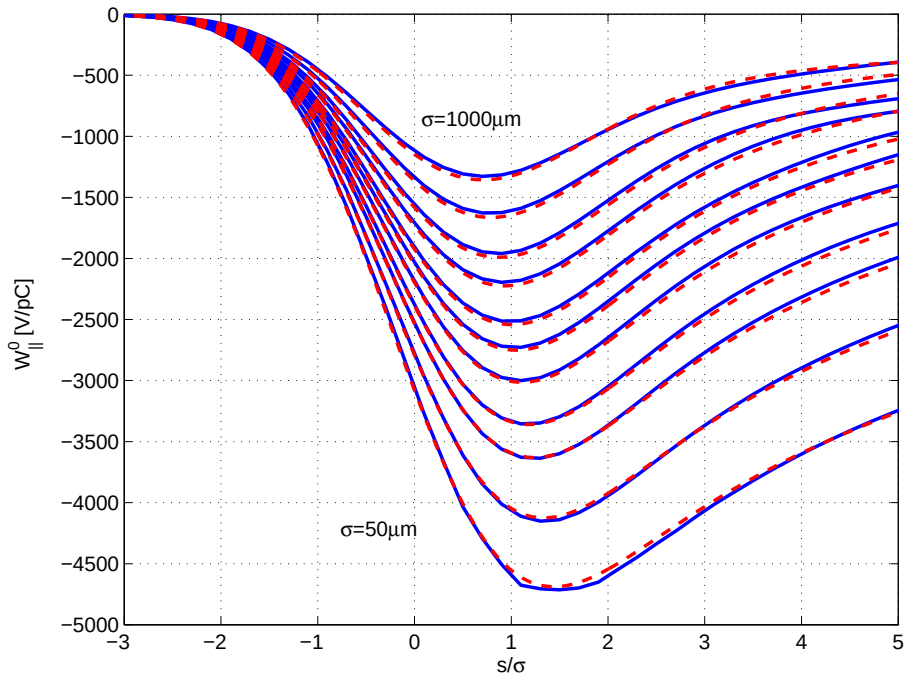

Figure 2.17: Longitudinal numerical (blue solid lines) and analytical (red dashed lines) wake potentials of the BTW structure.

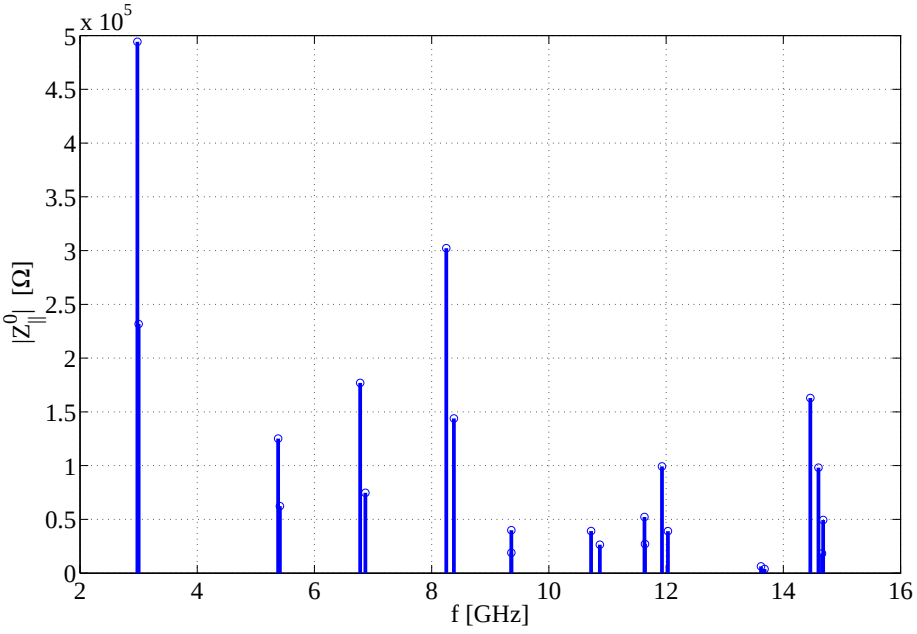

Figure 2.18: Longitudinal low frequency impedance in the BTW structure.

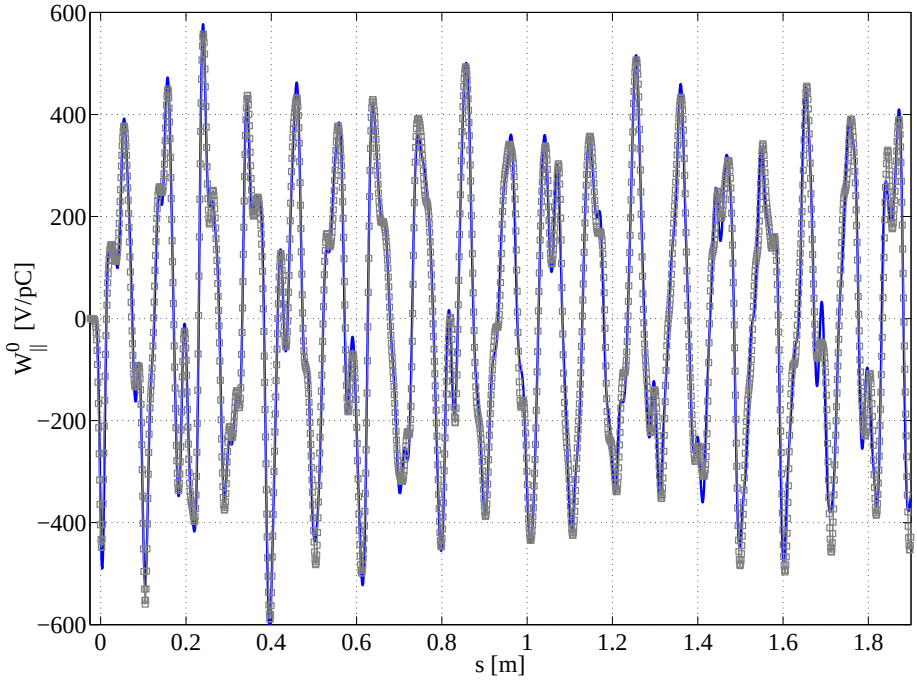

Figure 2.19: The long-range numerical (grey squares) and "analytical" (solid line) longitudinal wake potentials for a Gaussian bunch with $\sigma = 5mm$ in the BTW structure.

Table 2.5: Comparison of the numerical and analytical kick factors.

σ $[\mu m]$	Numerical Kick Factor $[V/pC/mm]$	Analytical Kick Factor $[V/pC/mm]$	Error [%]
50	12.26	12.17	0.7
80	17.19	17.11	0.5
120	22.53	22.45	0.4
150	25.90	25.82	0.3
200	30.69	30.58	0.4
250	34.72	34.56	0.5
300	38.04	37.96	0.2
400	43.73	43.51	0.5
500	48.07	47.89	0.4
700	54.48	54.42	0.1
1000	60.98	60.98	0.0

a distance up to 2 meters after the bunch. The long-range transverse wake function may be considered as a superposition of the contributions of the individual dipole modes. Hence, the

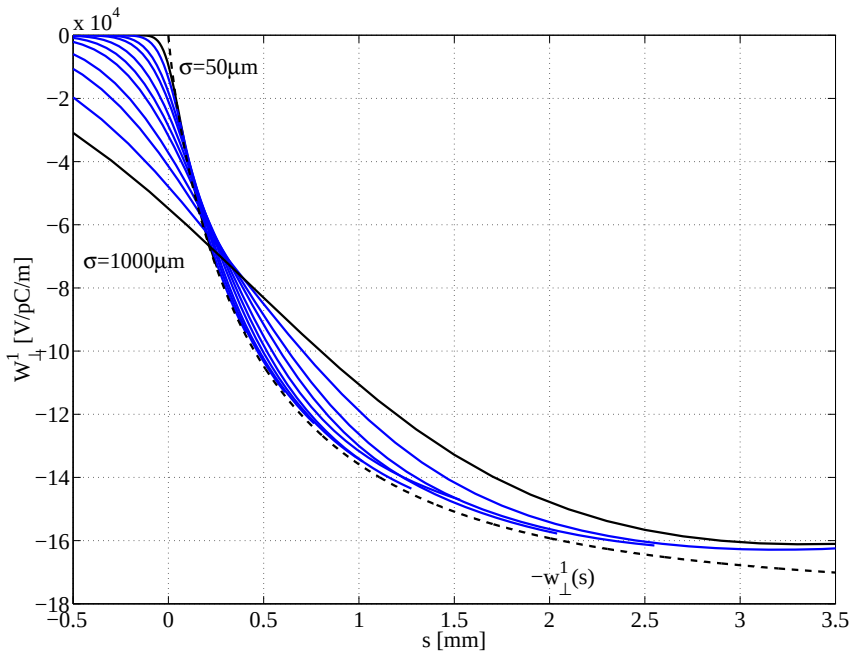

Figure 2.20: Transverse wake potentials (solid lines) and transverse wake functions (black dashed line) of the BTW structure.

following expression should approximate the transverse wake function:

$$w_\perp(s) = \theta(s)[2\sum_{i=1}^{\infty} K_{i,II}\frac{c}{2\pi f_{i,II}}\sin(\frac{2\pi}{c}f_{i,II}s)] + \theta(s)[2\sum_{i=1}^{\infty} K_{i,I}\frac{c}{2\pi f_{i,I}}\sin(\frac{2\pi}{c}f_{i,I}s)] \qquad (2.19)$$

where $K_{i,II}$ and $K_{i,I}$ are the modal kick factors of type II and type I cells, respectively. The modal kick factors are calculated in frequency domain with code MAFIA. To obtain an approximation of the long-range wake function we keep in (2.19) only a finite number (N=16) of addends corresponding to the lowest frequencies. The results are shown in table 2.6 and figure 2.23. Figure

Table 2.6: The lowest frequencies and their amplitudies for long-range transverse wake function of the BTW structure obtained from MAFIA eigenmode solver.

$f_{i,II}$	[GHz]	4.94	6.94	8.54	9.97	10.42	12.23	12.93	13.27
$K_{i,II}$	10^{17}	5.92	5.56	0.65	26.83	0.90	26.19	5.44	1.80
$f_{i,II}$	[GHz]	13.96	15.17	15.22	16.35	16.59	17.09	17.20	17.27
$K_{i,II}$	10^{17}	1.88	23.87	0.08	2.83	1.59	0.15	1.19	22.63
$f_{i,I}$	[GHz]	4.93	6.90	8.56	9.92	10.41	12.10	13.02	13.25
$K_{i,I}$	10^{17}	2.77	3.16	0.10	10.58	0.74	14.02	0.95	0.57
$f_{i,I}$	[GHz]	13.89	15.08	15.28	16.29	16.60	17.04	17.10	17.44
$K_{i,I}$	10^{17}	0.54	1.05	7.56	2.45	0.21	0.43	3.78	7.81

2.24 shows the long-range numerical (blue line) and "analytical" (2.19) (red line) transverse wake

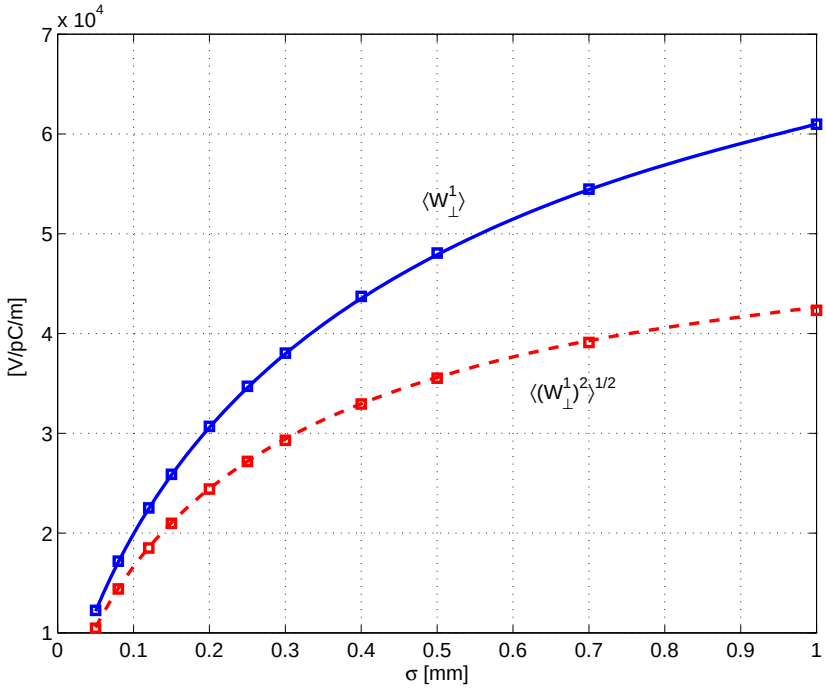

Figure 2.21: Comparison of numerical (box) and analytical (line) kick factor $\langle W_\perp^1 \rangle$ and kick spread $\langle (W_\perp^1)^2 \rangle^{1/2}$ as function of bunch length σ.

potentials for a Gaussian bunch with $\sigma = 5mm$. We can see that the wake function (2.19) approximates the transverse wake adequately.
As in longitudinal case, a direct analysis of the numerical wake potential can be done. The transversal wake function is approximated by the expression

$$w_\perp(s) = \theta(s) 2 \sum_{i=1}^{\infty} K_i \frac{c}{2\pi f_i} \sin(\frac{2\pi}{c} f_i s) \tag{2.20}$$

where the frequencies and amplitudes have been obtained with the help of the Prony-Pisarenko algorithm and are shown in Table 2.7. The wake function (2.20) approximates the wake a little better as compared to expression (2.19). This can be seen in figure 2.25. The figure shows the long-range numerical (blue line) and the new "analytical" (2.20) (red line) transverse wake potentials for a Gaussian bunch with $\sigma = 5mm$.

Table 2.7: The lowest frequencies and their amplitudies for the long-range transverse wake function of the BTW structure obtained with the help of Prony-Pisarenko method applied to the wake potential (f_i in GHz and $K_i \times 10^{17}$).

f_i	4.94	6.89	6.92	8.53	9.91	10.41	12.03	12.15	12.91
K_i	8.67	3.41	5.96	0.72	39.67	1.46	15.51	23.09	5.96
f_i	14.04	15.02	15.14	16.14	16.67	17.21	18.94	20.62	21.47
K_i	2.81	18.44	20.13	11.32	24.10	5.43	8.23	19.28	4.88

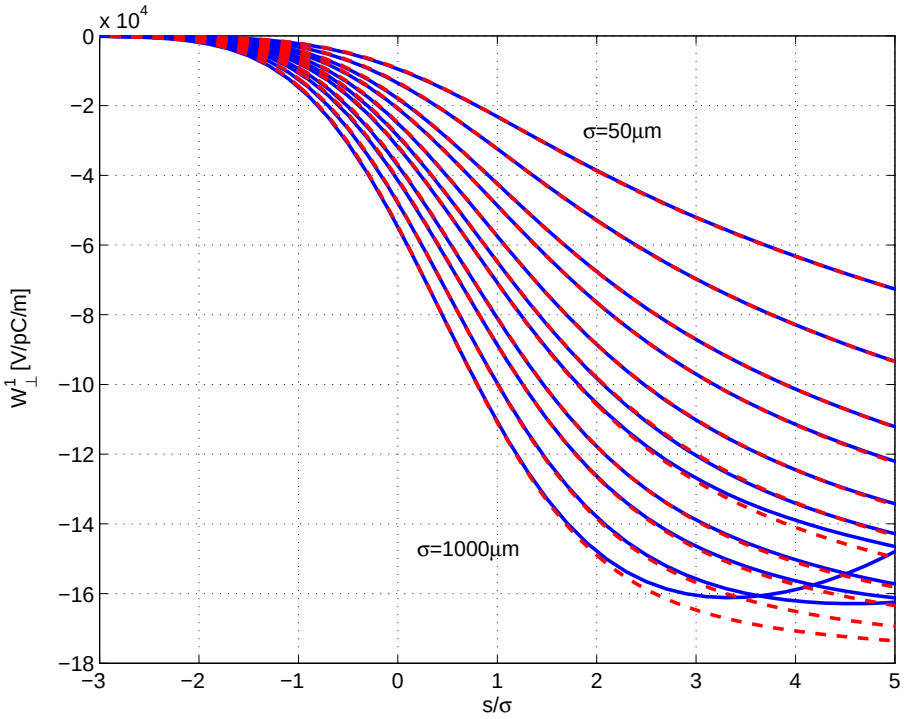

Figure 2.22: Transverse numerical (solid lines) and analytical (dashed lines) wake potentials of the BTW structure.

2.7 Single bunch energy spread

In this section the single bunch energy spread induced by the short-range longitudinal wakefields has been analyzed and a preliminary optimization of the energy spread has been carried out by varying the energy gain and RF phase of the accelerating structure. At the exit of each BTW accelerating module, the single bunch energy spread is determined by the RF accelerating fields produced by the external generator and the wakefields excited by the beam in the accelerating structure. As already shown in [10], for a Gaussian bunch the RMS energy spread can be evaluated by knowing four integral parameters of the wakefields: the loss factor $K_{||}$, the average wake energy spread $\sqrt{\Delta W^2}$, the cosine-Fourier part I_{cos} and the sine-Fourier part I_{sin}. The last two parameters are needed to take into account the correlation between the wake potentials and the accelerating voltage. Table 2.8 summarizes the four integral parameters for bunches of several lengths obtained with numerical time domain simulation (a), and analytical calculations (b) using (1): an excellent agreement between the two sets of data is shown. Figure 2.26 shows the relative energy spread $\Delta U/\langle U\rangle$ while figure **??** shows the relative average energy gain $\langle U\rangle/U_0$ (right) as a function of the RF phase ϕ, for several energy gains per section U_0. The calculations have been made under the assumption that the energy spread is negligible with respect to the total energy gain for acceleration section and considering a maximum energy gain for section up to 170 MeV. We can see that the average energy gain at optimum phase ϕ_{opt} is approximately 27% lower than the corresponding value on crest, $\phi = 0^o$, for each value of the peak of the acceleration voltage. Table 2.9 contains the relative energy spread when the beam is accelerated on crest, RF phase

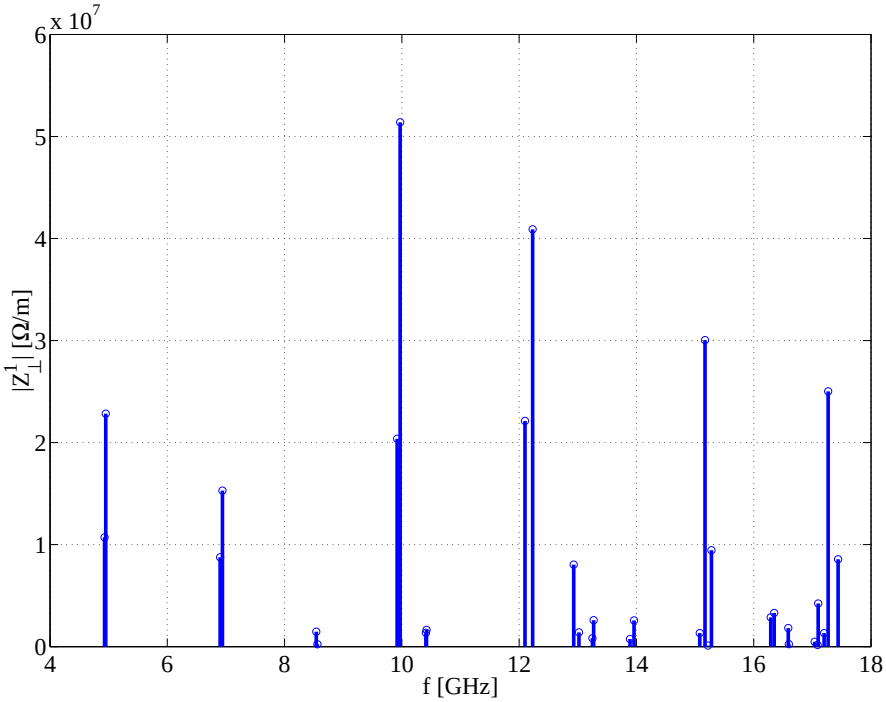

Figure 2.23: Transverse low frequency impedance in the BTW structure.

$\phi = 0^o$, and the minimum relative energy spread at the optimum phase ϕ_{opt}. These parameters are given for several peaks of the accelerating voltage. The relative energy spread decreases with the increase of the accelerating voltage. With an maximum energy gain of 170 MeV the minimum relative energy spread is about 2 times lower than the corresponding at $\phi = 0^o$. Figure 2.28

Table 2.8: Numerical and analytical integral parameters of the wake potentials of Gaussian bunches in the BTW structure.

σ $[\mu m]$	$K_{\|\|}$ $[V/pC]$	I_{cos} $[V/pC]$	I_{sin} $[V/pC]$	$\sqrt{\Delta W^2}$ $[V/pC]$
Numerical integral parameters (a)				
50	-2861.7	-0.001477	-4.368020	1459.8
120	-2298.3	-0.009598	-7.860948	1118.4
150	-2145.5	-0.015227	-8.964911	1029.0
Analytical integral parameters (b)				
50	-2861.2	-0.001546	-4.307913	1441.2
120	-2295.4	-0.009476	-7.831107	1112.5
150	-2145.8	-0.014982	-8.961020	1026.3

shows different behaviors of the relative energy spread as a function of the electric field gradient (changing the RF phase from -50^o to 10^o) for several peaks accelerating voltage U_0, for a bunch

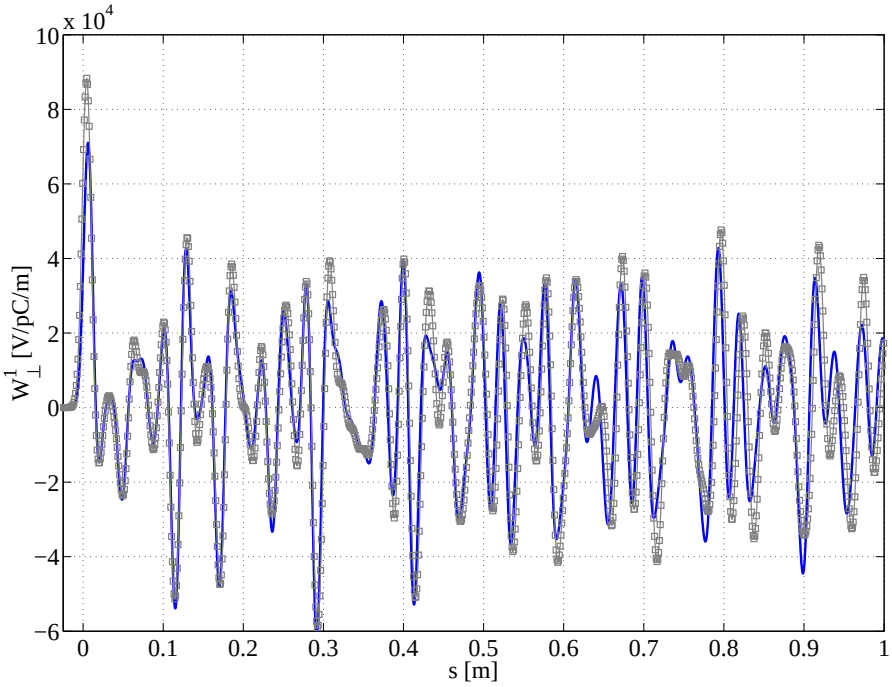

Figure 2.24: The long-range numerical (gray squares) and "analytical" (solid line) transverse wake potentials for Gaussian bunch with $\sigma = 5mm$ in the BTW structure. The "analytical" wake calculated with coefficients of Table 2.6.

with length $\sigma = 120\mu m$ with a charge $Q = 1nC$. Considering the $21MV/m$ as required for FEL-1, we can see that the relative energy spread is near its minimum value only for $U_0 = 170MeV$. In addition, with lower values of U_0 the relative energy spread does not get its minimum value through the tuning of the RF phase.

2.8 Conclusion

In this chapter, the wakefield calculations for short bunches passing through the complete BTW accelerating structure are presented. The cavity has been treated as an axially symmetric periodic structure of finite length. In the beginning of the paper single-cell wakefields were calculated. Then an estimation of the evolution of the wakefields in the multi-cell structure was done. It was shown that for the stabilization of the longitudinal and transverse wake potentials for a bunch with RMS length $200\mu m$ at least ~ 7 and ~ 10 cells are needed, respectively.
Then, the short-range longitudinal and transverse wake potentials of the complete BTW accelerating structure were calculated. From the numerical results, analytical approximations of the point-charge wake functions were found. The used analytical model was chosen as a combination of periodic and one-cell dependences. In the longitudinal case, the term that describes the finite structure (one cell behavior) is very small compared to the periodic structure term. Hence, in the studied range of σ, the longitudinal wakes mainly shows periodic structure behavior. To fit the

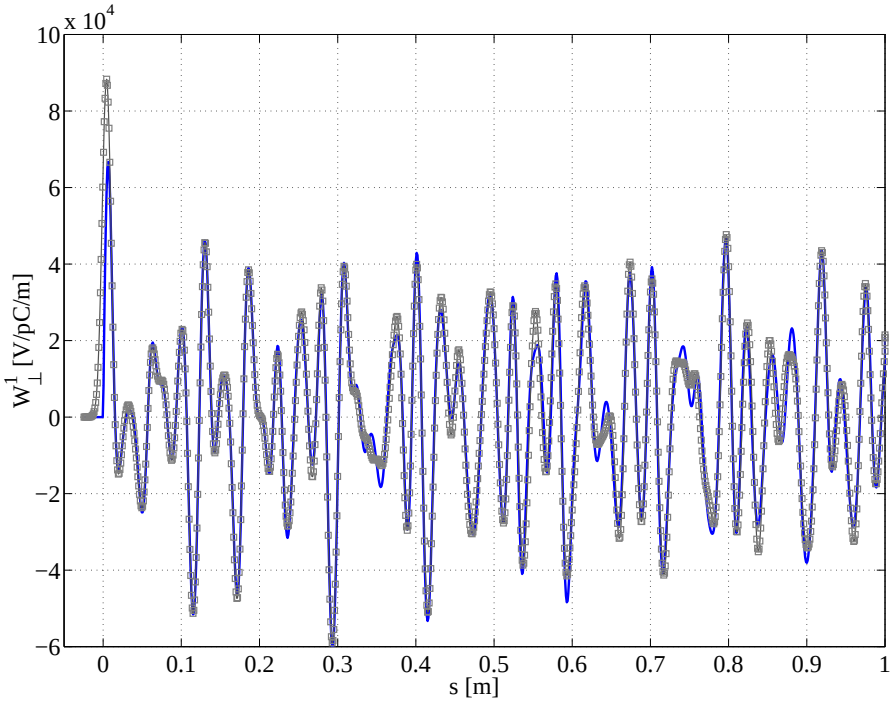

Figure 2.25: The long-range numerical (grey squares) and "analytical" (solid line) transverse wake potentials for a Gaussian bunch with $\sigma = 5mm$ in the BTW structure. The "analytical" wake calculated with coefficients of Table 2.7.

Table 2.9: Energy gain and energy spread in the BTW structure (bunch length $\sigma = 120\mu m$ and $Q = 1nC$).

U_0 $[MeV]$	RF phase	$\langle U \rangle$ $[MeV]$	$\Delta U/\langle U \rangle$ %
130.0	$\phi = 0.0^o$	127.70	0.87
	$\phi_{opt} = -41.6^o$	94.96	0.59
140.0	$\phi = 0.0^o$	137.70	0.81
	$\phi_{opt} = -42.6^o$	100.69	0.51
150.0	$\phi = 0.0^o$	147.70	0.76
	$\phi_{opt} = -43.0^o$	107.48	0.45
160.0	$\phi = 0.0^o$	157.70	0.71
	$\phi_{opt} = -42.6^o$	115.44	0.40
170.0	$\phi = 0.0^o$	167.70	0.67
	$\phi_{opt} = -41.8^o$	124.47	0.36

data up to $5mm$ we have used an additional term in the model.
The above formulas for the wake function are calculated from the numerical results for the com-

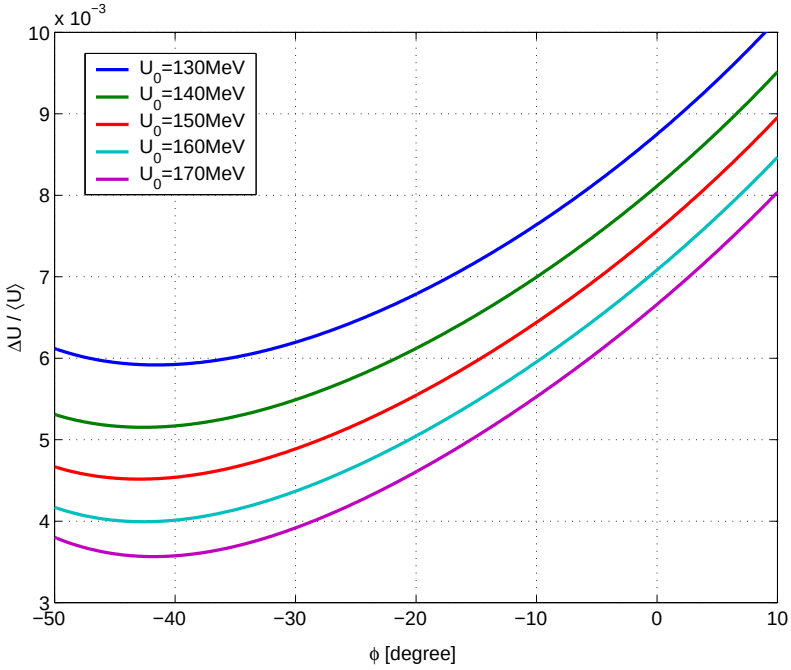

Figure 2.26: Relative energy spread as a function of the RF phase (left) in the BTW structure (bunch length $\sigma = 120\mu m$ and $Q = 1nC$).

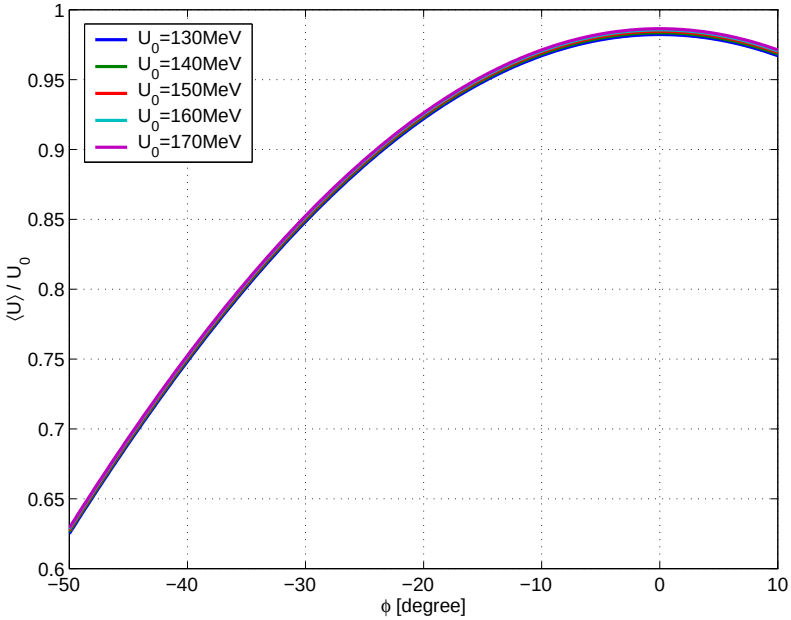

Figure 2.27: Relative energy gain as a function of the RF phase in the BTW structure (bunch length $\sigma = 120\mu m$ and $Q = 1nC$).

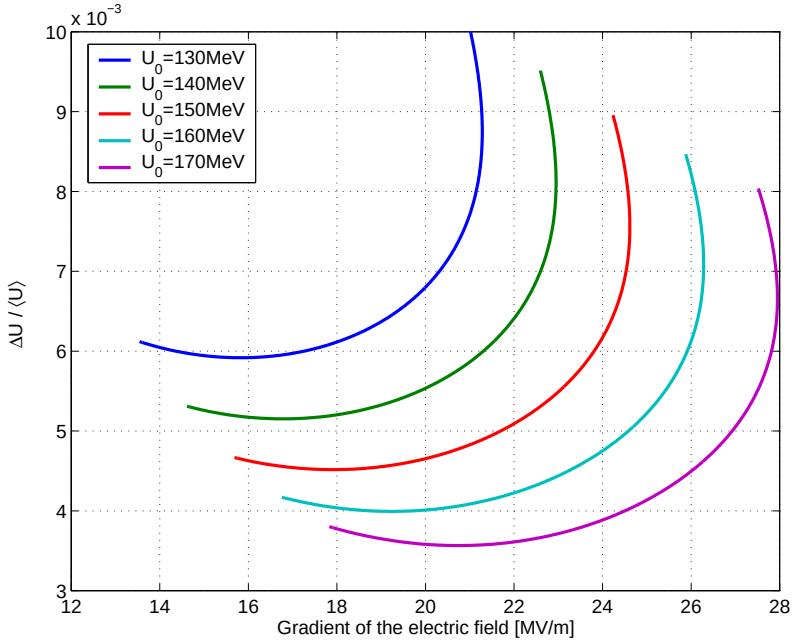

Figure 2.28: Relative energy spread as a function of the gradient of the electric field in the BTW structure (bunch length $\sigma = 120\mu m$ and $Q = 1nC$).

plete BTW structure. To obtain the wake function on the unit of active length the relations should be divided by structure length $L_{tot} = 6.075[m]$:

$$w_{\parallel}^{0}(s) = 1202 \cdot e^{-\sqrt{\frac{s}{3.2\cdot 10^{-4}}}} + \frac{0.560}{\sqrt{s}} \quad [\frac{V}{pC \cdot m}] \quad 0 < s \leq 1.5mm \tag{2.21}$$

$$w_{\parallel}^{0}(s) = 1226 \cdot e^{-\sqrt{\frac{s}{3\cdot 10^{-4}}}} + \frac{0.494}{\sqrt{s}} + 494\sqrt{s} \quad [\frac{V}{pC \cdot m}] \quad 0 < s \leq 5mm \tag{2.22}$$

$$\begin{aligned} w_{\perp}^{1}(s) &= 2.8 \cdot 10^{4}[1 - (1 + \sqrt{\frac{s}{1.2 \cdot 10^{-4}}}) \cdot e^{-\sqrt{\frac{s}{1.2\cdot 10^{-4}}}}] + \\ &+ 1.4 \cdot 10^{4} \cdot \sqrt{s} \quad [\frac{V}{pC \cdot m \cdot m}] \quad 0 < s \leq 2mm \end{aligned} \tag{2.23}$$

In addition, we have estimated the long-range longitudinal and transverse wakefields. We have used two alternative methods: model loss factor calculations in frequency domain with MAFIA solver for single cell and a direct analysis of the numerical wake potential for a Gaussian bunch calculated for a distance up to 2 meters after the bunch. In the longitudinal case there is a good agreement between the methods while in the transverse case the direct analysis provides a wake function that approximates the long-range wake a little better than with the frequency domain method.
Furthermore, the single bunch energy spread induced by longitudinal wakefields has been analyzed for the first phase of the FEL-I project. We have seen that the wakefield effects can be compensated by shifting the bunch injection phase to optimum values, decreasing the energy gain of about 27%.

For the energy design of FEL-I and an energy gain of 170 MeV per section this means operating at $\phi = -41.8^o$ and a gradient of $21MV/m$.

References

[1] A. Novokhatsky, M. Timm, and T. Weiland, "Transition dynamics of the wake fields of ultra short bunches," in *Proc. of the 5th Int. Comp. Accel. Phys. Conf.*, Monterey, California, USA, 1998, p. 132.

[2] I. Zagorodnov and T. Weiland, "Calculation of transverse wake potential for short bunches," in *Proc. of the 7th Int. Comp. Accel. Phys. Conf.*, East Lansing, Michigan, USA, 2002, p. 343.

[3] G. D'Auria and C. Rossi, Sincrotrone Trieste, Trieste, Tech. Rep. ST/M-TN-91/15, 1991.

[4] P. Girault, "The $3\pi/4$ Backward TW Structure for the ELETTRA 1.5 GeV Electron Injector," in *Proc. of the IEEE Part. Accel. Conf.*, San Francisco, California, 1991, p. 3005.

[5] T. Weiland *et al.*, "MAFIA Version 4," *AIP Conf. Proc.*, vol. 391, pp. 65–70, 1997.

[6] F. Zhou and M. Dohlus, "Wakefield induced correlated energy spread and emittance growth at TTF FEL," in *Proc. of the 21st Int. FEL Conf.*, Hamburg, Germany, Aug 1999.

[7] K. L. Bane and M. Sands, "Wake fields of very short bunches in an accelerating cavity," *Part. Accel.*, vol. 25, p. 73, 1990.

[8] K. L. F. Bane, "Short range dipole wakefields in accelerating structures for the NLC," SLAC, Tech. Rep. SLAC-PUB-9663, Mar 2003.

[9] T. W. Park and C. S. Burrus, *Digital Filter Design.* John Wiley and Sons, Inc., 1987.

[10] A. Novokhatsky, M. Timm, and T. Weiland, "Single bunch energy spread in the TESLA cryomodule," DESY, Tech. Rep. DESY-TESLA-99-16, 1999.

Chapter 3

Beam break-up instability in the FERMI@Elettra linac

Abstract
The electron beam dynamics in the presence of the linac structural wakefield is studied. Trajectory manipulation is used to gain control of the transverse wakefield-induced instability and this technique is also validated in the presence of shot-to-shot trajectory jitter. A specific script working with Courant-Snyder variables has been written to evaluate the residual banana shape after instability suppression in the presence of shot-to-shot trajectory jitter[1][2][3].

[1]P. Craievich, S. di Mitri and A. A. Zholents *Nucl. Instr. Meth. Phys. Res. A*, vol. 604, p. 457, 2009.

[2]P. Craievich and S. Di Mitri *Proceeding of the 10th European Particle Accelerator Conference*, Edinburgh, UK, p. 26, 2006.

[3]P. Craievich and S. Di Mitri *Proceeding of the 27th International Free Electron Laser Conference*, Stanford, California, 2005.

3.1 Introduction

The operation of x-ray free electron lasers (FELs) requires small emittance electron beams. Although both self amplified spontaneous emission (SASE) FELs [1–5] and harmonic cascade (HC) FELs [6–9] are mostly sensitive to slice emittance, it is also important that relative transverse offsets of different slices or slice-to-slice variations along the electron bunch remain within defined limits in order to avoid significant growth of the projected emittance under the influence of the linac structural (also called geometric) wake fields.
The single bunch projected emittance dilution and the banana shape distortion induced by short range transverse wake field have been extensively treated for linear colliders with regard to the luminosity performance, like in [10–13]. Trajectory bumps to minimize the projected emittance growth have been introduced in [13–17]. Furthermore, the impact of the trajectory jitter on the single bunch dynamics in the presence of transverse wake field has been investigated in [12, 18–21], still with regard to luminosity loss and projected emittance growth in colliders.
Just as for colliders, the HC seeded FELs are sensitive to the projected emittance growth because it has an impact on the FEL peak power. The FEL power relies on the energy exchange of electrons and photons along the undulator chain; for this interaction to occur the two beams must overlap. This happens in the first undulator, called modulator, where the external seeding laser has to superimpose on the electron bunch, as well as in the succeeding undulators, called radiators, where the electrons should overlap with the coherent radiation emitted by themselves. The overlapping requirement causes the FERMI@elettra seeded FEL [22] to be sensitive to the projected emittance growth generated by the transverse displacement of the longitudinal slices of the bunch [23]. This situation is mitigated by the fact that $\sim 50fs$ seeded laser is much shorter than the $\sim 0.7ps$ electron bunch, so that some projected emittance growth can still be tolerated if the slice transverse offset is sufficiently small in the region of the bunch where photons and electrons overlap. These considerations must be verified in the presence of the electron beam trajectory jitter and this is the subject of this study.
Codes like PLACET, MTRACK and MBTRACK [24–27] adopt Courant-Snyder variables to calculate the bunch slice coordinates and finally to evaluate the coherent trajectory growth due to a betatron motion component in the presence of transverse wake field. The incoherent trajectory growth due to random misalignment of machine elements and its compensation via trajectory bumps is carried out in most modern linear accelerators that require high brightness electron beams. In a similar way, the authors have shown in [28, 29] that the single bunch emittance growth in the FERMI@elettra linac, computed by the Elegant particle tracking code [30] through longitudinal slice treatment, is in a good agreement with the prediction of the theory developed in [31, 32]. Building on the work referred to in the above paragraphs, this paper addresses the impact of trajectory jitter on the degradation of the projected emittance induced by short range geometric transverse wake fields during a single pass of the electron bunch through the FERMI@elettra normal conducting, S-band linac. Special care has been devoted to the incoherent part of the trajectory growth due to random misalignment of quadrupole magnets and accelerating sections. This paper will show that control over the single bunch instability is achievable in the FERMI@elettra linac by applying local trajectory bumps even in the presence of a shot-to-shot trajectory jitter.
The instability analysis is focused on the correlation of the slice transverse offset with its longitudinal position along the bunch. A specific Self-Describing Data Sets (SDDS) [30] script working

with Courant-Snyder variables has been written to evaluate the residual banana shape after time-averaged instability suppression in the presence of shot-to-shot trajectory jitter. A statistical parameter for each bunch slice has been introduced whose maximum value over all the slices determines the projected emittance growth.
For completeness, well known methods of evaluation of the projected emittance and of the banana shape are included and the consistency of all methods is demonstrated for FERMI@elettra. The practical end product of this study is the capability of specifying the tolerances on trajectory jitters for the FERMI@elettra linac FEL.

3.2 Study outline

The basis of the single bunch instability induced by short range geometric transverse wake field in the FERMI@elettra linac are recalled in the first Section of this article as an introductory part to the following study. The equations of motion describe the evolution of the banana shape along the accelerator under the influence of the FERMI linac wake functions. The FERMI@elettra linac and the electron beam main parameters are listed for reader's benefit.
As a first step, the FERMI@elettra trajectory correction scheme is presented and the contributions to the trajectory distortion are discussed; they are:

(i) misalignment of magnetic elements, linac RF phase and voltage errors, beam launching error. These errors determine the machine error budget;

(ii) trajectory distortion induced by the emission of Coherent Synchrotron Radiation (CSR) in dispersive regions of the linac lattice;

(iii) trajectory distortion induced by the banana shape.

Simulations including all these effects show that a global trajectory correction provided through a Response Matrix algorithm is not sufficient to damp the single bunch instability; for this reason, local trajectory bumps are the preferred method of correction.
The effectiveness of the trajectory manipulation described above is verified in presence of shot-to-shot trajectory jitter. Firstly, the trajectory jitter budget is evaluated by considering the following error sources: beam launching error jitter, quadrupole magnet mechanical vibration and current ripple, jitter of the parasitic dispersion induced by misaligned quadrupoles. Once the jitter budget is found, the analysis of the single bunch instability in the presence of shot-to-shot trajectory jitter is documented.
The projected emittance at the linac end is evaluated and its dependence on the beam launching error jitter is shown. The distribution of the banana shapes for all the jittered runs is presented. Finally, the Courant-Snyder variables are introduced to describe the phase space mismatch of each longitudinal slice of the bunch in the presence of trajectory jitter. All the three methods projected emittance, banana shape, Courant-Snyder amplitude provide consistent results. The conclusion reports about the expected impact of the instability on the FERMI@elettra FEL performance.

3.3 Theoretical background

3.3.1 Equation of motion

An electron traveling off axis in an accelerating module excites the short range geometric transverse wake field that affects trailing electrons. This has a result that the bunch tail oscillates with respect to the bunch head forming in the (t-x) and in the (t-y) planes a characteristic banana shape.
Persistence of the slice oscillations along the linac and their amplification may cause the conversion of the bunch length into the transverse dimension (beam break up). So, the displaced bunch tail adds a contribution to the projection of the beam size on the transverse plane, thus increasing the projected emittance.
The transverse motion of a relativistic electron in the linac in the presence of the short-range transverse wake field is described by the following equation [31–33]:

$$\frac{1}{\gamma(\sigma)}\frac{\partial}{\partial\sigma}\left[\gamma(\sigma)\frac{\partial}{\partial\sigma}x(\sigma,\zeta)\right]+\kappa(\sigma)^2x(\sigma,\zeta)= \\ =\varepsilon(\sigma)\int_{-\infty}^{\zeta}w_n(\zeta-\zeta_1)F(\zeta')\left[x(\sigma,\zeta')-d_c(\sigma)\right]d\zeta' \quad (3.1)$$

γ is the relativistic factor, $\sigma = s/L$ is the distance from entrance of the linac normalized with respect to the total linac length L, $\zeta = z/l_b$ is the normalized coordinate measured after the arrival of the head of the beam at location σ, where l_b is the full width (FW) electron bunch length, $F(\zeta) = I(\zeta)/I_{max}$ is the normalized current, I_{max} is the maximum peak current, $\kappa = kL$, k is the product of the RF focusing strength, $w_n(\zeta)$ is the normalized transverse wake function and d_c is the misalignment of the accelerating modules of the linac. The term $\varepsilon(\sigma) = \varepsilon_r/[\gamma(\sigma)/\gamma(0)]$ is defined by:

$$\varepsilon_r = \frac{4\pi\epsilon_0 W_0 I_{max} l_b L^2}{\gamma(0) I_A} \quad (3.2)$$

$I_A = 17020A$ is the Álfen current, ε_0 is the dielectric constant of the vacuum and $W_0 = w(1)$ is the wake function amplitude at $\zeta = 1$. That formalism shown so far is valid, independently, in the vertical and horizontal planes.

3.3.2 Wake function

When the electron bunch travels near the axis of the accelerating structures, the transverse wake field is dominated by the dipole field. FERMI@elettra linac employs Backward Traveling Wave structures (BTW) whose transverse wake function can be approximated with the following analytical expression [34]:

$$w(\zeta) = 1.7\cdot 10^5\left[1-\left(1+\sqrt{\frac{\zeta}{\zeta_1}}\right)e^{-\sqrt{(\zeta/\zeta_1)}}\right]+8.5\cdot 10^4\sqrt{\zeta} \quad (3.3)$$

with $\zeta_1 = 1.2\dot{1}0 - 4m/l_b$. Let us define the normalized wake function as:

$$w_n = \frac{w(\zeta)}{W_0} \quad (3.4)$$

W_0, ζ_1 and $w_n(\zeta 1)$ depend on the full width bunch length l_b.
A successful benchmarking of simulations and theoretical predictions of the projected emittance growth induced by the single bunch instability in case of beam launching error and linac misalignment is reported in [28]; the main parameters used in those studies are adopted in this paper and reported in Table 3.1 for the reader's reference.

Table 3.1: Parameters of the electron bunch used for the study of the single bunch instability in the FERMI@elettra linac.

	Value	Units
Average initial energy at entrance of BTW linac	600	MeV
Average final energy	1200	MeV
BTW linac total length	30.375	m
Full width bunch length	200	μm
Peak current in bunch core	800	A
Normalised emittance, rms	1.5	$mm\ mrad$
Final slice energy spread, rms	150	keV
W_0	$1.048 \cdot 10^{16}$	$V/C/m^2$
ζ_1	0.600	-
ε_r	8.620	-

3.4 Static trajectory distorsion

This Section defines the static machine error budget and shows the beam trajectory along the FERMI@elettra linac to be taken as reference for the following shot-to-shot jitter studies. The on-axis trajectory is distorted by the machine errors and by the beam launching error. The trajectory correction scheme is implemented but collective effects like CSR and transverse wake field diminish its efficacy. Local bumps are finally applied to the trajectory to suppress the instability.

3.4.1 Machine Error Budget

The FERMI@elettra linac layout is shown in Figure 3.1. The photoinjector includes an RF gun followed by two traveling wave accelerating structures that accelerate the beam to 95 MeV. The rest of the linac is based upon two different types of accelerating structures:

(a) seven 4.5 m long, SLAC-type, constant gradient structures (C1-C7). They are grouped in the so called Linac 1 and Linac 2, as shown in Figure 3.1. The maximum energy gain per cavity is $47MeV$;

(b) seven 6.1 m long Backward Traveling Wave (BTW) structures (S1-S7), grouped in the so called Linac 3 and Linac 4, as shown in Figure 3.1. They are equipped with a SLED RF pulse compression system. The maximum energy gain per cavity is $140MeV$.

In addition to the previously described accelerating structures, FERMI will require the use of an X-band 4th harmonic ($12GHz$), $0.6m$ accelerating structure, located in the middle of Linac 1.

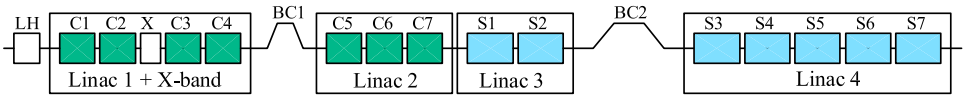

Figure 3.1: Schematic of the FERMI@elettra linac layout. Simulations presented in this paper concern the beam dynamics from the 100 MeV laser heater (LH) area to the end of Linac 4 at 1.2 GeV. BTW structures are in Linac 3 and Linac 4; they start at the linac longitudinal coordinate of $80m$.

The bunch length is then compressed in two stages by means of the achromatic magnetic chicanes BC1 and BC2, also shown in Figure 3.1.
This study covers the electron beam dynamics from the photoinjector end to the linac end. The FERMI@elettra linac lattice has been simulated in Elegant by adopting the static machine error setting shown in Table 3.2. The emittance growth induced by the single bunch instability depends on the errors affecting the machine optics (quadrupole misalignment and strength error) and the acceleration parameters (phase and voltage errors change the beam energy). Realistic error values typically adopted in linear colliders and linacs for FELs have been chosen. The trajectory

Table 3.2: Machine error setting for the FERMI@elettra linac. It includes errors on dipoles and quadrupoles main integrated field component ($b_i l$), element misalignments, magnet tilt angles, beam launching error and accelerating module phase and voltage errors. All values are rms taken over a Gaussian distribution with a 3 sigma cut-off.

	$\Delta(b_i l)/(b_i l)$ [%]	$\Delta x, \Delta y$ $[\mu m]$	Δz $[\mu m]$	Roll $[mrad]$
Dipoles	0.01	150	150	0.5
Quadrupoles	0.01	150	150	0.5
BPMs	-	150	150	-
Acc. Modules	-	300	150	-
Acc. Mod. Voltage error	0.1%			
Acc. Mod. Phase error	$0.1^\circ S-band$			
Launching error	$\Delta x = 150\mu m, \Delta x' = 1\mu rad, \Delta y = 150\mu m, \Delta y' = 1\mu rad$			

correction scheme foresees 24 steering magnets (correctors) in both the transverse planes and 31 Beam Position Monitors (BPMs) whose rms resolution is assumed to be $20\mu m$. A pair of horizontal and vertical correctors and one BPM are placed after each accelerating structure. The Elegant "global" method for trajectory correction has been implemented that minimizes the BPM position readings by using the trajectory Response Matrix.
For illustration of trajectory distortion and single bunch instability development, only one set of errors randomly chosen over a realistic sample of error seeds is shown in the following Sections. A discussion of the statistical distribution of the trajectory distortion over a large number of random seeds can be found in [29, 35, 36].
Simulations have been performed with 200.000 macroparticles, divided into 30 longitudinal slices.

The particle spatial distribution is approximately Gaussian in the transverse dimensions; the initial current profile is approximately a linear ramp [37] from the bunch head to the tail and it becomes flatter after the bunch length compression. The longitudinal phase space has an energy chirp that increases to $\sim 1\%$ in the first bunch compressor and decreases to $\sim 0.1\%$ as the bunch travels through the linac.

3.4.2 Trajectory Distortion by Collective Effects

CSR is emitted in the dipoles of the magnetic chicanes of the Laser Heater (LH), first (BC1) and second (BC2) compressor; they are shown in Figure 3.1. CSR has been simulated with Elegant [38, 39]; its emission causes a reduction of the beam average energy at the dispersive regions. Hence, the bunch centroid shifts to a trajectory that is a few hundreds of micrometer far from the one defined by the nominal energy. In other words, CSR emission distorts the trajectory at the exit of the magnetic chicanes.
Another contribution to the trajectory distortion comes from the transverse wake field. An ideal trajectory correction sets the centroid trajectory to zero, but, due to the wake field, head and tail particles perform uncorrected betatron oscillations. The correction efficiency that can be maximized for a rigid beam is therefore degraded by the banana shape dynamics. The residual centroid dispersion generated by a misaligned structure grows resonantly with s and becomes large at the end of the $150m$ long FERMI linac [40].
Figures 3.2, 3.3, 3.4 compare the trajectory distortion in a bare lattice with the one simulated in the presence of CSR and transverse wake field. The comparison shows that CSR induced trajectory distortion can be neglected with respect to the wake field contribution, particularly in the latter part of the linac, which is made of the high impedance BTW accelerating modules.

3.4.3 Trajectory Local Bumps

Even after the correction, the residual trajectory distortion shown in Figure 3.5 induces an emittance dilution at the linac end; the projected emittances in Figure 3.6 blow up as the beam enters the BTW structures, at a distance of about $80m$ (see Figure 3.1). The emittance blow up can be avoided by applying trajectory local bumps [13–16]. Their simulation is shown in Figure 3.7. The bumps technique looks for an empirical "golden" trajectory for which all the kicks generated by the transverse wake field compensate each other and the banana shape is finally cancelled. When applying the local bumps, the steering magnets force the beam on a distorted trajectory while keeping the beam off axis excursion to less $500\mu m$. Six steerers and six BPMs distributed along the BTW linac have been used for the bumps. The maximum variation of the steerer strengths with respect to the nominal set up is $0.2mrad$ (about 20% of the nominal steerer set up). The emittances are finally compensated, as shown in Figure 3.8.
The implementation of the local bumps in the FERMI@elettra linac foresees the characterization of the transverse beam profile as a function of the bunch longitudinal coordinate projected on screens separated by a proper phase advance. This will be done in the diagnostic section downstream of the linac by means of an RF deflector [41], both in the horizontal and vertical planes.

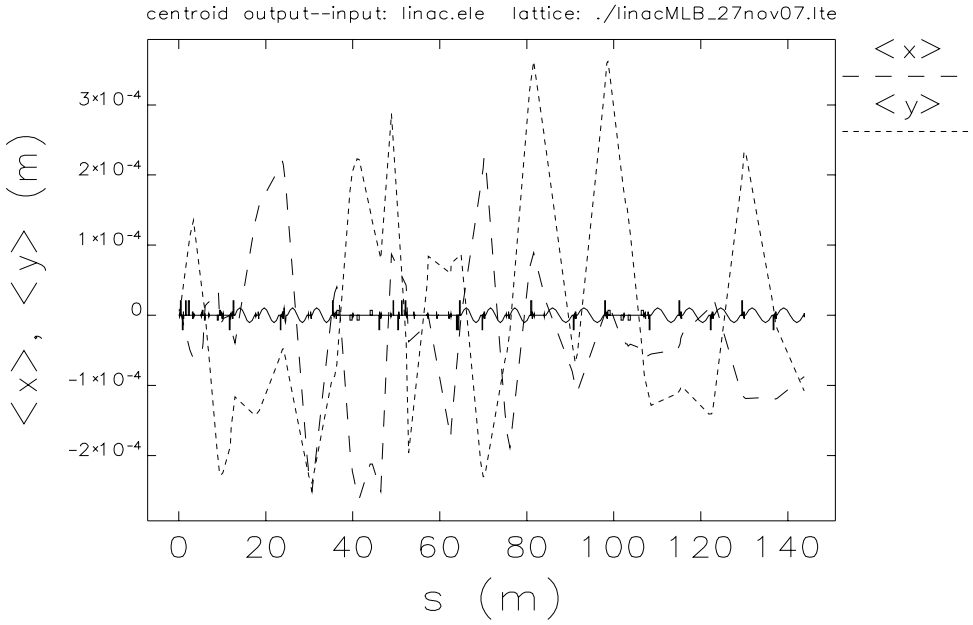

Figure 3.2: Bunch centroid position along the FERMI@elettra linac after the trajectory correction has been performed with Elegant by using the global correction method. Field errors, gradient errors and element misalignments have been implemented. Neither CSR nor wake fields have been included. Solid line at the plot centre is a sketch of the machine layout.

3.5 Trajectory Jitter Budget

Owing to its local property, the efficacy of the local bumps technique depends on the specific machine configuration (i.e., misalignment of elements) and beam optics (i.e., bunch centroid position and angular divergence) at the locations where the bumps are applied. Accordingly, shot-to-shot trajectory jitter may affect the scheme efficacy by changing the bunch centroid transverse coordinates at the location of the bumps. The first aim of this Section is to evaluate a realistic budget for the sources of trajectory jitter in the FERMI@elettra linac.

3.5.1 Launching Error

The reference machine lattice and the reference trajectory are defined by the ensemble of errors in Table 3.2 with the exception of the launching error and by the steerers setting as shown in Figure 3.6. Shot-to-shot jitters cause variations around the reference trajectory. One of its main sources is the launching error jitter, which may be generated by the jitter of the photo-cathode laser pointing.
The jitter budget has been estimated by considering that the shot-to-shot jitter of the bunch centroid position at the injector end should not exceed a small fraction of the beam size, if the machine is properly tuned. For example, the betatron functions at the FERMI linac entrance are $\beta_x = \beta_y = 19m$. Those values coupled with the rms geometric emittances of $\varepsilon_x = \varepsilon_y =$

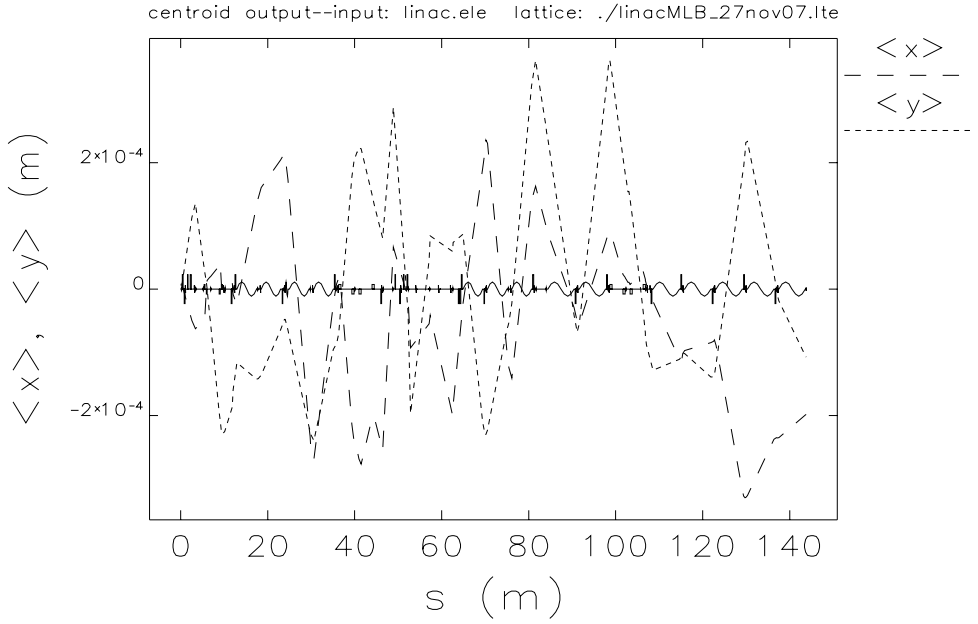

Figure 3.3: Bunch centroid position along the FERMI@elettra linac after the trajectory correction has been performed with Elegant by using the global correction method. CSR has been added to the scenario in Figure 1. Solid line at the plot centre is a sketch of the machine layout.

$7.65\mu m\ mrad$ give an rms beam size in both planes. The rms launching position variation is assumed to be 10% of the rms beam size; that is, $38\mu m$. The launching angular divergence is related to the launching position through the injector optics. The trajectory distortion generated by an angular kick θ_k at a longitudinal position s_k in the lattice and observed at a downstream position s_0 is given by (likewise in the vertical plane):

$$x_0 = \theta_k \sqrt{\beta_k \beta_0}\, \sin(\Delta\mu_{k0}) \tag{3.5}$$

where β_k and β_0 are the betatron functions in the plane of interest at the locations s_k and s_0, respectively, and $\Delta\mu_{k0}$ is the corresponding betatron phase advance. The corresponding distortion of the angular divergence at position s_0 is therefore given by:

$$x_0' = \frac{dx_0}{ds_0} = -\theta_k \frac{\sqrt{\beta_k}}{\sqrt{\beta_0}} \left[\alpha \sin(\Delta\mu_{k0}) + \cos(\Delta\mu_{k0})\right] \tag{3.6}$$

In FERMI $\alpha_0 = 0$ and $\Delta\mu_{k0} \approx 45°$; these values reduce 3.6 to $x_0' = (x_0/\beta_0) ctg(\Delta\mu_{k0}) = x_0/19m$. Thus, the launching error jitter was simulated by moving the position and the angular divergence of the bunch centroid at the linac entrance over a Gaussian distribution with standard deviation and with a 3 sigma cut-off.

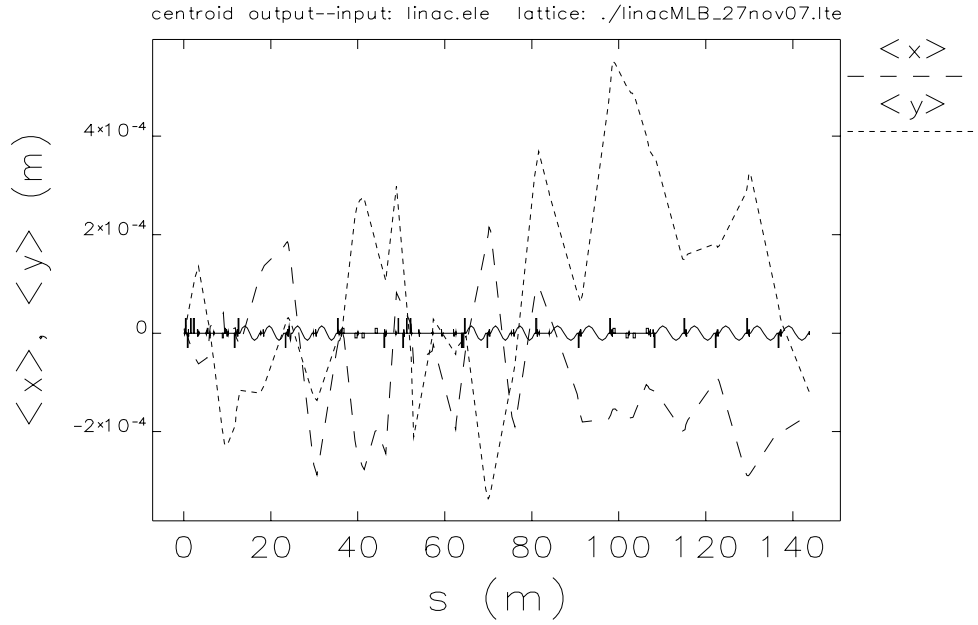

Figure 3.4: Bunch centroid position along the FERMI@elettra linac after the trajectory correction has been performed with Elegant by using the global correction method. Structural transverse wake fields have been additionally included to the scenario in Figure 2. Solid line at the plot centre is a sketch of the machine layout.

3.5.2 Quadrupole Vibration and Current Ripple

Other contributions to the trajectory jitter are: quadrupole vibrations, short-term magnetic field stability and shot-to-shot variation of the parasitic dispersion. As for the quadrupole vibrations, rms vibration amplitude of $0.5\mu m$ in the range $1 - 100Hz$ (FERMI will nominally operate at $50Hz$) leads to an rms variation of the induced angular kick per quadrupole of:

$$\theta_{k,\nu} = \frac{\Delta \int B(s)ds}{B_0\rho} = kl_q\Delta r \approx 0.2mm\ mrad \tag{3.7}$$

where k is the quadrupole normalized strength, typically equal to $2m^{-2}$, $l_q = 0.2m$ is the quadrupole magnetic length and $\Delta r = 0.5\mu m$ is the rms vibration amplitude.
The relative short term ($< 100Hz$) stability of the quadrupole gradient is essentially the stability of the current signal provided by the power supply; reasonably, it is in the range $10^{-4}10^{-5}$. The rms variation of the induced angular kick is therefore:

$$\Delta\theta_{k,ps} \leq 10^{-4}\theta_k = 10^{-4}kl_qR \simeq 20\mu m\ mrad \tag{3.8}$$

where a particle offset $R = 0.5mm$ inside the quadrupole magnet is considered.

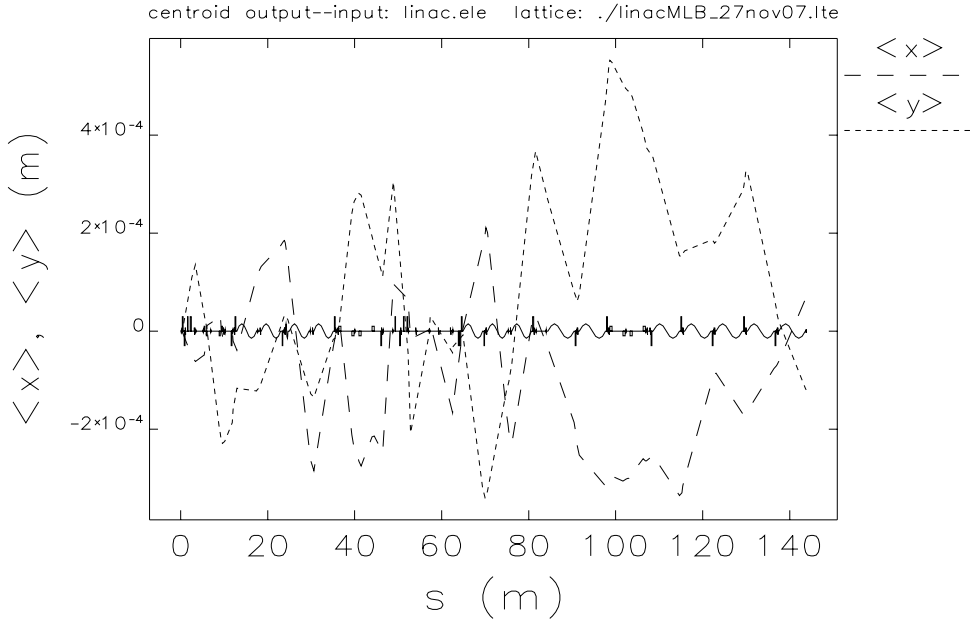

Figure 3.5: Bunch centroid position along the FERMI@elettra linac after the trajectory correction has been performed with Elegant by using the global correction method. No local bumps have been implemented. Solid line at the plot centre is a sketch of the machine layout.

3.5.3 Parasitic Dispersion

When the quadrupole magnet is traversed off axis, a shot-to-shot variation of its integrated gradient excites parasitic dispersion that contributes to the shot-to-shot trajectory distortion. Dispersion induced in both transverse planes by the quadrupole gradient variation is estimated in thin lens approximation by:

$$\begin{aligned} D &= \frac{1}{\rho(1/\rho^2 - k)} \left[1 - \cos\left(\sqrt{\left(\frac{1}{\rho^2} - k \right)} l_q \right) \right] \\ &\simeq \frac{1}{\rho(1/\rho^2 - k)} \left[\frac{1}{2} \left(\frac{1}{\rho^2} - k \right) l_q^2 \right] = \frac{l_q^2}{2\rho} = \frac{l_q \theta_k}{2} \end{aligned} \tag{3.9}$$

where $\rho = l_q/\theta_k$ is the curvature radius induced by the quadrupole magnetic field when the magnet is traversed off axis. A similar consideration gives for the derivative of the parasitic dispersion $\Delta D' \approx \theta_k$. Given 3.8, the maximum induced parasitic dispersion and its derivative is therefore of the order of:

$$\begin{aligned} \Delta D &\simeq \frac{l_q}{2} \Delta\theta_{k,ps} \simeq 2nm \\ \Delta D' &\simeq \theta_{k,ps} \approx 200mm\ mrad \end{aligned} \tag{3.10}$$

The particle position and angular offset are equal to, respectively, the parasitic dispersion and its derivative times the relative energy spread. The relative energy spread in the FERMI@elettra

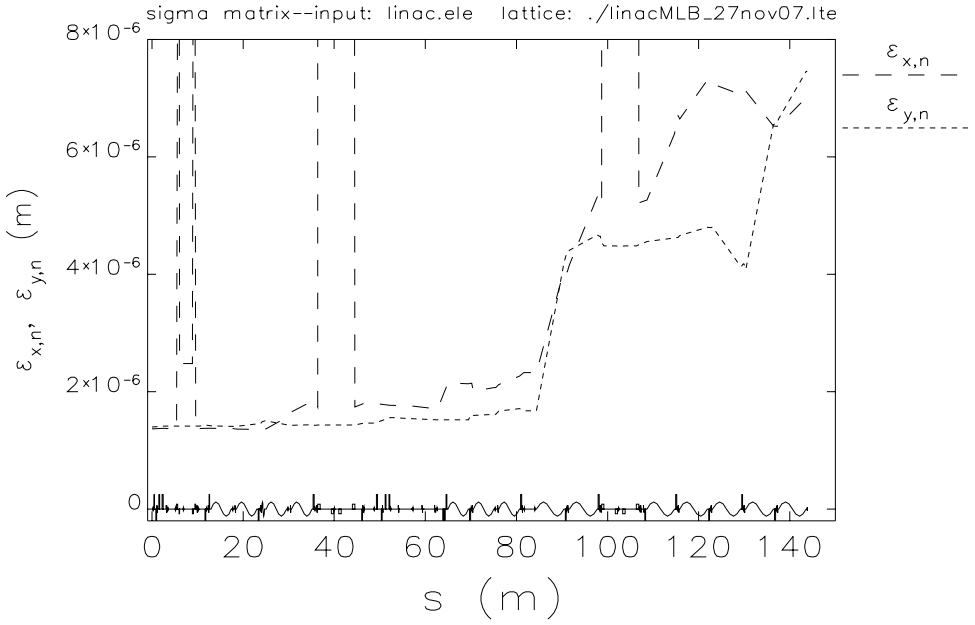

Figure 3.6: Single bunch wake field instability in the FERMI linac, before the application of local trajectory bumps. The emittances blow up as the bunch enters the first BTW module (approximately at $80m$ of the abscissa). Emittance bumps (out of scale) around abscissa values 10, 40 and $100m$ should be ignored; they correspond to the dispersive contribution in magnetic chicanes. Solid line at the bottom is a sketch of the machine layout.

linac does not exceed $2 \cdot 10^{-2}$, so that the maximum trajectory variation induced by parasitic dispersion and its derivative never exceeds the sub-nanometer level for the particle position and a few μrad for the divergence.
Elegant simulations have been performed with the trajectory jitter budget listed in Table 3.3: the jitter budget includes the launching error jitter and the quadrupole vibrations. The parasitic dispersion functions and their induced trajectory distortion are taken into account.

Table 3.3: Trajectory jitter budget including the launching error jitter and the quadrupole vibration. The values apply both to horizontal and vertical planes.

	Position jitter (rms) (μm)	Divergence jitter (rms)
Launching error	38	$2mm\ mrad$
Quadrupole vibration	0.5	-

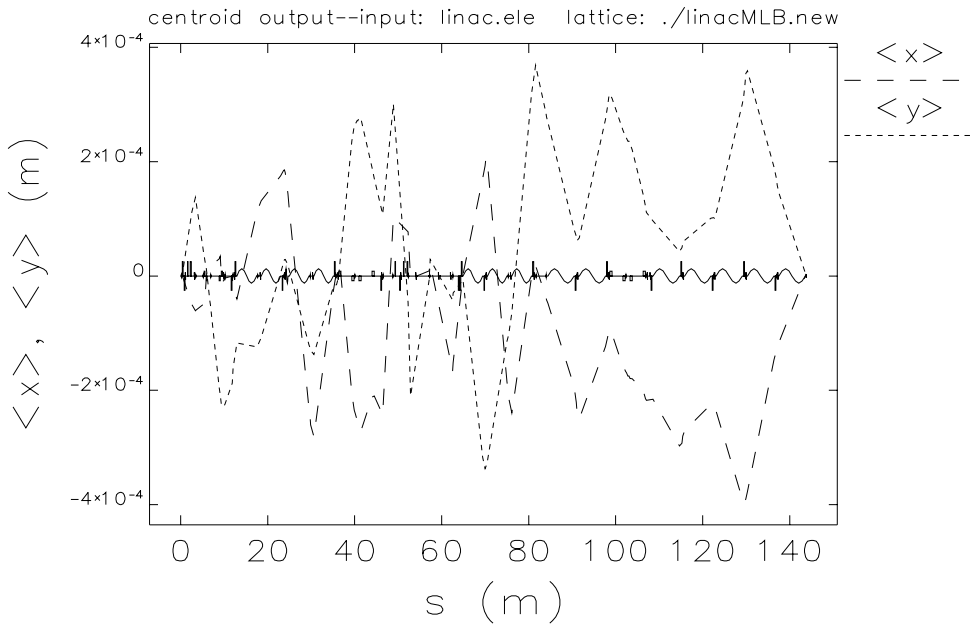

Figure 3.7: Bunch centroid position along the FERMI@elettra linac after the trajectory correction has been performed with Elegant by using the global correction method. Local trajectory bumps have been switched on; the trajectory is manipulated along the last part of the linac allowing the instability suppression. Solid line at the plot centre is a sketch of the machine layout.

3.6 Shot-to-shot trajectory jitter

In the previous Sections the reference trajectory along the FERMI@elettra linac has been defined. Subsequently, shot-to-shot trajectory jitter was added. The aim of this Section is to evaluate whether the single bunch instability remains suppressed by the trajectory local bumps in the presence of trajectory jitter. Three methods for evaluating the effect of the instability on the electron distribution are presented: evaluation of the projected emittance, of the banana shape and the definition of a new parameter for each slice of the bunch that is linked to the slice phase space mismatch induced by the instability.

3.6.1 Projected Emittance

A rotational symmetry of the accelerating modules around their longitudinal axis was assumed in the simulations. The geometric transverse wake field in the accelerating sections is taken as uniform over the whole transverse beam size, that is, we use a simple dipole wake. Hence, the slice emittance is preserved, while the projected emittance is not because the wake field drives a bunch tail oscillation relative to the bunch head; in this way, a correlation is established between the longitudinal slice position and its lateral displacement (banana shape).
Let us reasonably assume the following approximation that is the full width transverse beam size, in each plane, is covered by four standard deviations (σ) of the particle position distribution. The

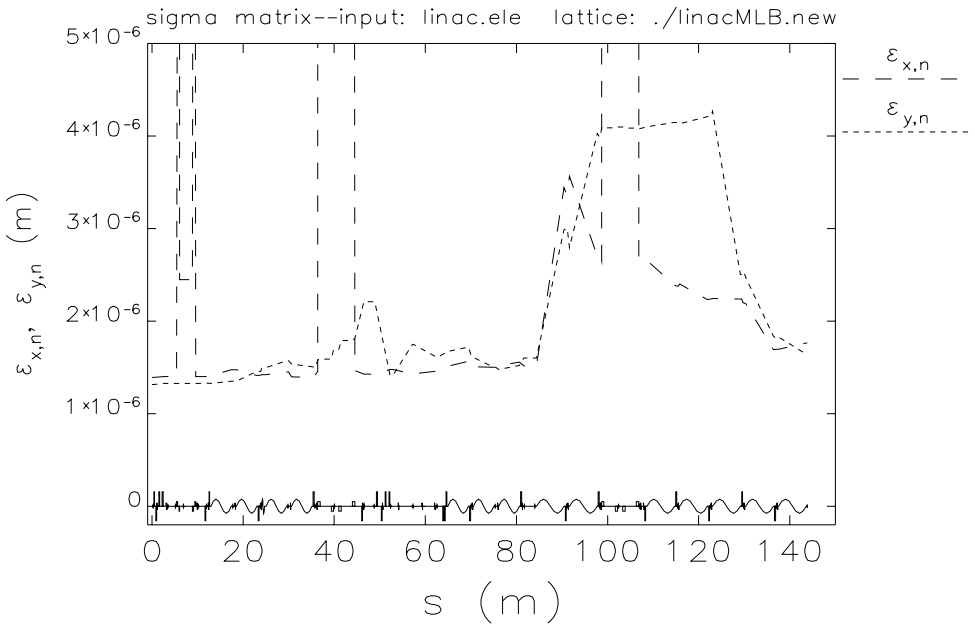

Figure 3.8: Single bunch wake field instability suppressed by local trajectory bumps. The final normalized emittance values are slightly larger than the initial one ($\sim 1.4mm\ mrad$). Emittance bumps (out of scale) around abscissa values 10, 40 and $100m$ should be ignored; they correspond to the dispersive contribution in magnetic chicanes. Solid line at the bottom is a sketch of the machine layout.

beam standard deviation at the linac end is approximately $100\mu m$. The tolerance on the beam size growth induced by instability is now fixed so that it is sufficiently smaller than the total beam size, namely the bunch tail centroid should not laterally exceed the head centroid by more than 1σ [23], as it is sketched in Figure 3.9. In this limit case, the total projected beam size becomes $5\sigma_0$ that we re-define equal to $4\sigma_{eff}$. The relative growth of the beam size is therefore:

$$\frac{\Delta\sigma}{\sigma} = \frac{\sigma_{eff} - \sigma_0}{\sigma_0} = 25\% \tag{3.11}$$

Figure 3.9 shows the schematic of the beam size growth described by (3.11). Since $\sigma = \sqrt{\varepsilon\beta}$, where ε is the projected geometric emittance and β the betatron function, the relative variation of the beam size is half of relative variation of the emittance. In other words, the projected emittance growth after instability suppression must be less than 50%.
Particle tracking simulations were performed to evaluate the sensitivity of the projected emittance growth, specified at the linac end, on the launching error jitter. Figure 3.10 shows the normalized emittances when the launching coordinates of the bunch centroid move along an ellipse of semi-axes $x = 76\mu m$ and $x' = 4\mu rad$ (two times greater than the rms launching error specified in Table 3.3) in the (x, x') phase space. The same considerations apply to the vertical plane. The maximum emittance growth is 44% in the horizontal plane and 64% in the vertical plane. The lack

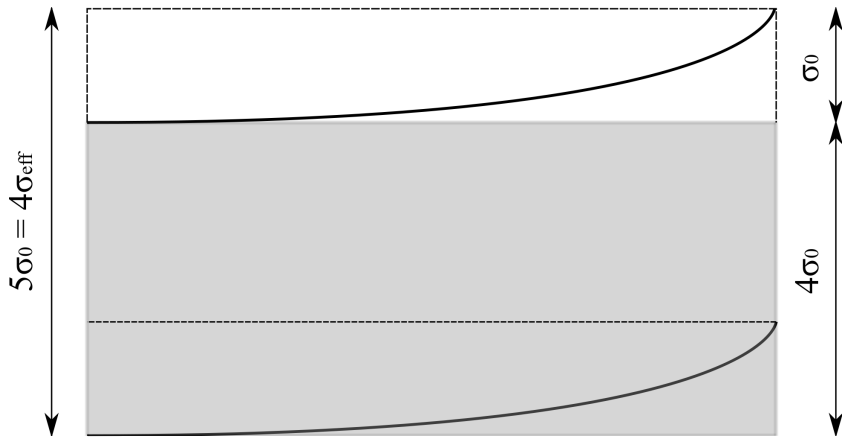

Figure 3.9: Schematic top view of a beam affected by SBBU instability; bunch head is on the left. The horizontal full width unperturbed beam size is $4\sigma_0$. The bunch tail deviation of $1\sigma_0$ is also shown. The projected beam size due to the banana shape is then defined in terms of an effective rms beam size σ_{eff} so that $4\sigma_{eff} = 5\sigma_0$.

of periodicity in the data results from the static errors in our initial configuration; in other words, the machine errors mask the dependence of the trajectory on the periodic launching condition; this fact in turn results into a non-periodic dependence on the wake field effect and on the projected emittance growth on the initial betatron phase.

3.6.2 Banana Shape

The emittance dilution can be quantified by means of the transverse deviation of the bunch tail with respect to the head, in units of unperturbed rms beam size (same applies to the vertical plane): $R_x = |x_{head} - x_{tail|}/\sigma_x$. Figure 3.11 shows the banana shape jitter over 50 runs generated by the trajectory jitter budget in Table 3.3. Averaging over all these runs gives $R_x = 0.2 \pm 0.7$ for the horizontal plane and $R_x = 0.8 \pm 0.8$ for the vertical plane.
To be consistent with the constraint (3.11) for the suppressed single bunch instability, $R_{x,y} \leq 1$, R should be less than 1. Thus, for this specific static error seed, the instability in the presence of shot-to-shot trajectory jitter affects more the vertical plane than the horizontal one; this result is consistent with the projected emittance growth observed in Figure 3.10.

3.6.3 Slice Centroid Amplitude

If the instability is suppressed at the linac end, then the slice centroid transverse offset and divergence are small. Hence the bunch tends to maintain its shape in the (t, x) and (t, y) plane at any point of the downstream line. On the contrary, if the banana shape is pronounced (instability not suppressed) the slice optics in the bunch tail is mismatched with respect to the magnetic lattice. In this case, the bunch tail starts develop betatron oscillations around the head axis and the banana shape at any point downstream will depend on the Twiss parameters at the point of observation. Therefore, the Courant-Snyder amplitude of the slice centroid is here introduced as

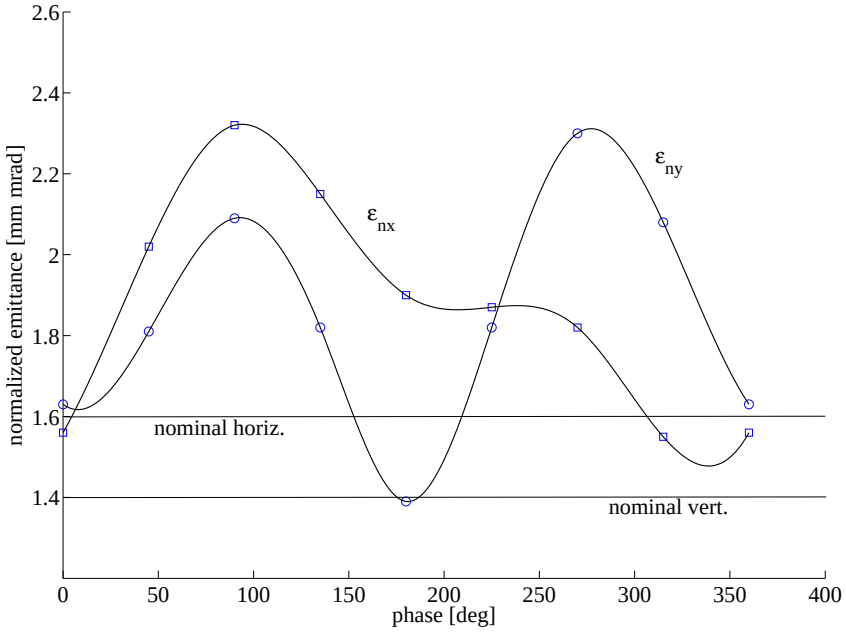

Figure 3.10: Normalized emittance growth at the linac end in presence of trajectory jitter listed in Table 3.3. The MLB centroid launching coordinates move along an ellipse of semi-axes $x = 76\mu m$ and $x' = 4\mu rad$ in the (x, x') phase space. The abscissa is the betatron phase that moves the launching error along the (x, x') ellipse. Same considerations apply to the vertical plane. Dynamics in the x and y plane has been studied separately that is the geometric coupling is neglected.

a parameter to characterize the instability (same applies to the vertical plane):

$$\varepsilon_{SC,u} = \gamma_x x_{cm}^2 + 2\alpha_x x_{cm} x'_{cm} + \beta_x x'^2_{cm} \tag{3.12}$$

ε_{SC} is a constant of motion in absence of frictional forces such as geometric wake fields and emission of radiation; this is the case for the beam transport downstream of the linac when coherent and incoherent synchrotron radiation is neglected. This quantity provides a measure of the amplitude of motion that is independent of betatron phase. Its square root is proportional to the amplitudes of the slice centroid motion x_{SC} that represents the banana shape:

$$\begin{aligned} x_{SC}(s) &= \sqrt{\varepsilon_{SC,x}\beta_x(s)}\cos(\Delta\mu_x) \\ x'_{SC}(s) &= -\sqrt{\frac{\varepsilon_{SC,x}}{\beta_x(s)}}\Big[\alpha_x(s)\cos(\Delta\mu_x) + \sin(\Delta\mu_x)\Big] \end{aligned} \tag{3.13}$$

In general, x_{SC} is the linear superposition of the three main contributions sketched in Figure 3.12:

(i) the betatron motion, $x_{s\beta}$, generated by focusing of misaligned quadrupoles;

(ii) the trajectory distortion, x_{ST};

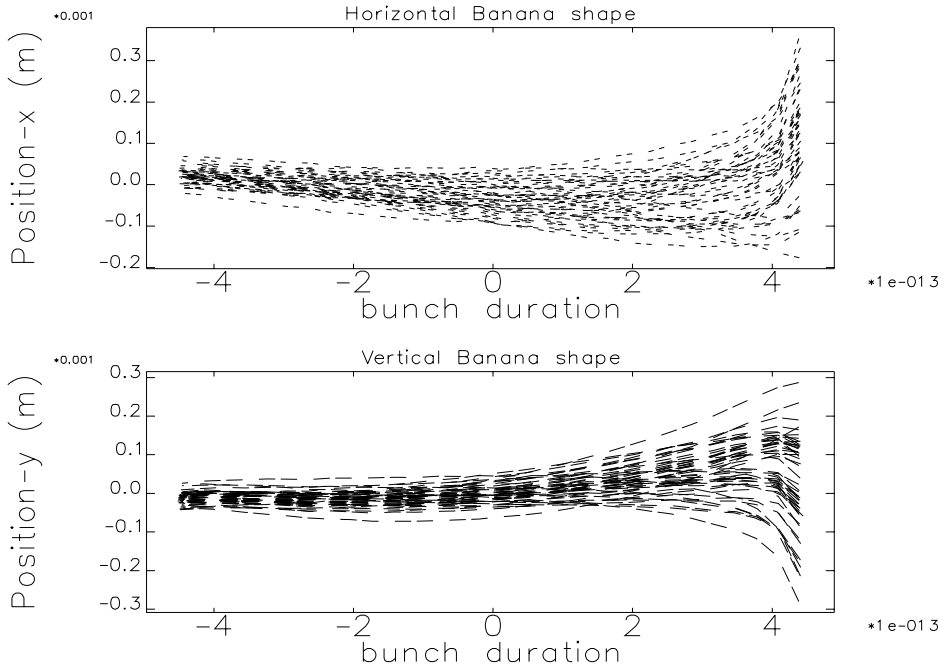

Figure 3.11: Banana shape (slice centroid lateral deviation vs. bunch duration in $100fs$ units) of the MLB at the FERMI linac end affected by trajectory jitter over 50 runs performed with Elegant. The jitter budget is specified in Table 3.2. Bunch head is on the left. The maximum head-tail deviation is $180\mu m$ in the horizontal plane and $240\mu m$ in the vertical plane. Particle tracking has been performed with 200.000 macro particles subdivided into 30 longitudinal slices.

(iii) the transverse wake field effect, x_{SW}.

Notice that $x_{offset} = x_{s\beta} + x_{ST}$ is approximately the same for all slices along the bunch. Regarding the instability, only the motion relative to the bunch head is of interest:

$$x_{SW} = x_{SC} - x_{s\beta} \equiv x_{SC} - x_{offset} \tag{3.14}$$

We now define new slice centroid amplitude relative to the bunch head motion as follows:

$$\varepsilon_{SW,x} = \gamma_x(x_{SC} - x_{offset})^2 + 2\alpha_x(x_{SC} - x_{offset})(x'_{SC} - x'_{offset}) + \beta_x(x'_{SC} - x'_{offset})^2 \tag{3.15}$$

The effect of the trajectory jitter on the scheme of instability suppression can be evaluated by looking at the shot-to-shot variations of the centroid amplitude ε_{SW} over the bunch duration. In fact, we require that the standard deviation (over all jittered runs) of the slice lateral deviation $\sigma_{x,SC}$ be less than the rms (over all particles) beam size $\sigma_x = \sqrt{\varepsilon_x \beta_x}$:

$$\frac{\sigma_{x,SC}}{\sigma_x} \leq 1 \tag{3.16}$$

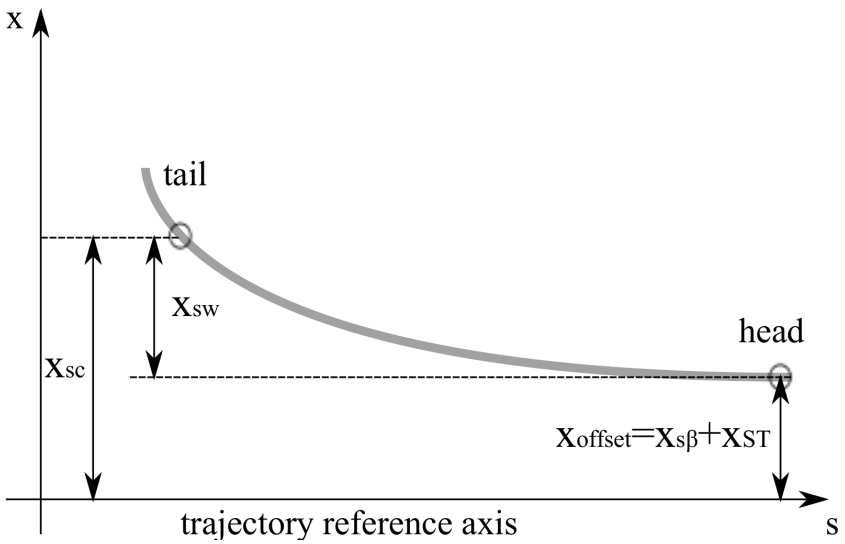

Figure 3.12: Contributions to the transverse motion of the slice centroid in presence of SBBU instability; x_{SW} describes the slice centroid displacement relative to the bunch head.

Since x_{offset} is a constant and, we can write:

$$\begin{aligned}\sigma_{x,SC} &= \sqrt{\langle x_{SC}^2 - \bar{x}_{SC}^2\rangle} \cong \sqrt{\frac{1}{N}\sum_{i=1}^{N}(x_{SW}^i - \bar{x}_{SW})^2} \\ &= \sqrt{\frac{1}{N}\sum_{i=1}^{N}\left[\sqrt{\beta_x^i \varepsilon_{SW,x}^i}\cos\varphi_x - \frac{1}{N}\sum_{i=1}^{N}\sqrt{\beta_x^i \varepsilon_{SW,x}^i}\cos\varphi_x\right]^2} \\ &= \sqrt{\beta_x}\cos\varphi_x\sqrt{\frac{1}{N}\sum_{i=1}^{N}\left[\sqrt{\varepsilon_{SW,x}^i} - \frac{1}{N}\sum_{i=1}^{N}\sqrt{\varepsilon_{SW,x}^i}\right]^2}\end{aligned} \tag{3.17}$$

In equation (3.17) the betatron function has been extracted from the summation under two reasonable assumptions: firstly, the slice Twiss parameters are the same as the projected ones even in case of slice lateral displacement; secondly, the slice Twiss parameters remain constant over all jittered runs.
We now define a new variable $\sqrt{\varepsilon_{SW,x}^i} \equiv Q_x^i$. Given $\cos\varphi_x \leq 1$, it is possible to make the condition (3.16) more stringent by defining the new instability threshold as the ratio between the standard deviation of Q_x^i and the square root of the rms projected (unperturbed) emittance:

$$\frac{\sigma_{Q,x}}{\sqrt{\varepsilon_x}} \leq 1 \tag{3.18}$$

Figure 3.13 shows the ratio defined by (3.18) along the bunch duration for the jitter budget specified in Table 3.3. Again, the reduced effectiveness of the instability suppression due to trajectory jitter is more pronounced in the vertical plane than in the horizontal plane. The same phenomenon is observed in the calculation of the projected emittance and of the banana shape.

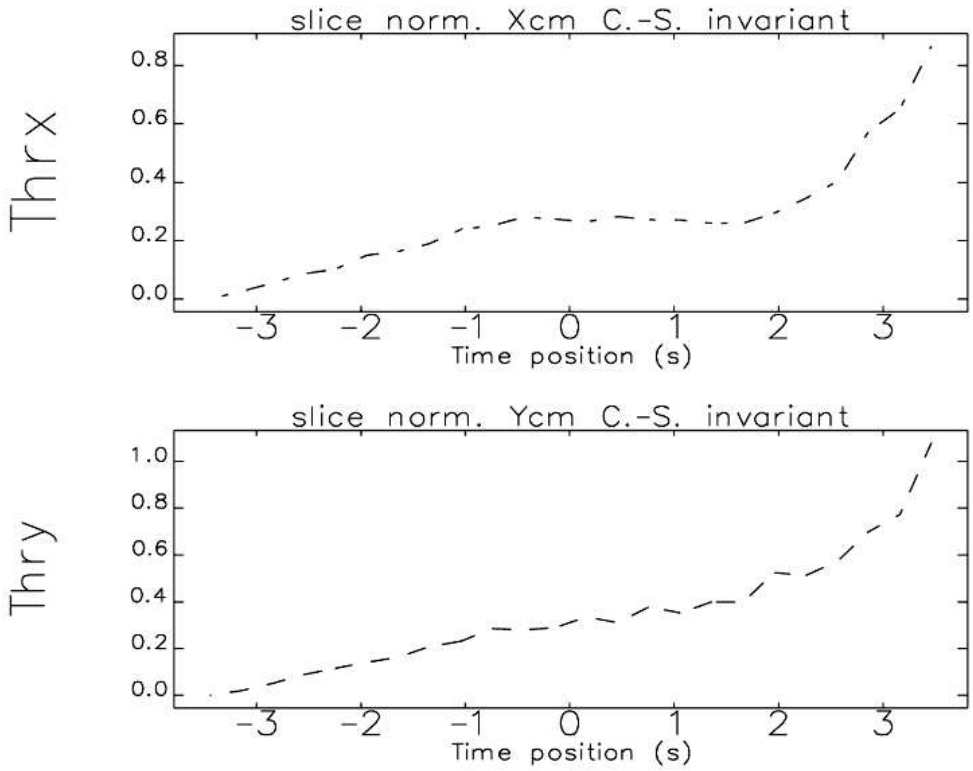

Figure 3.13: Ratio defined in (3.18) vs. MLB duration (in $100fs$ unit) at the linac end, affected by trajectory jitter specified in Table 3.3.

In addition to these two methods, the slice centroid amplitude offers a deeper and more complete understanding of the instability behavior in the presence of trajectory jitter. That is, the projected emittance analysis does not contain the information on the slice particle distribution. The emittance growth, more pronounced in the vertical plane than in the horizontal, could be due to a small portion of the bunch tail that does not participate in the seeded FEL process, since only a few hundreds of femtoseconds in the bunch core over a total duration of approximately $1ps$ are seeded in the FERMI@Elettra modulator. If the emittance growth predicted by the simulation comes from the bunch tail slice offset, then it would not affect the FERMI FEL performance.
The same considerations apply to the parameter $R_{x,y}$ since it deals with the projection of the banana shape onto the plane of interest and not with individual slice dynamics. Moreover, the jitter of the slice centroid position and divergence are treated separately. In this case, the instability suppression can only be evaluated by means of a function properly defined in terms of both the slice centroid position and divergence.
This function is expressed by $\varepsilon_{SW,x}$ in (3.15). The condition (3.18) applied to each slice of the bunch is able to predict which portion of the electron bunch can be safely used for the seeded FEL operation even in the presence of trajectory jitter. Figure 3.13 shows that the vertical plane is more affected from the single bunch instability than the horizontal. However, the transverse motion of only a very small portion of the bunch tail is really affected by the trajectory jitter. Owing to the fact that the condition (3.18) is widely satisfied ($< 50\%$) for most of the bunch slices

(about 80% of the bunch duration in both planes), we do not expect any important effect of the jitter on the FERMI FEL performance.

3.7 Conclusion

The effect of the transverse wake field instability on the electron beam quality in the S-band, normal conducting linac of FERMI@Elettra FEL has been discussed. A specific study of the instability in the presence of trajectory jitter has been presented together with a novel interpretation of the slice optics mismatch related to the seeded FEL option.
As a first step, a simulation of the projected emittance growth under the combined influence of transverse wake field, launching error and misaligned machine elements has been carried out using the Elegant tracking code applied to the FERMI@Elettra linac. The last part of this linac is composed of accelerating modules with particularly strong geometric wake fields that make it particularly suitable for the study of the instability. A static machine error budget has been given. Since the instability affects the transverse particle distribution (banana shape), a variation of the bunch centroid transverse coordinate with respect to the bare lattice case is expected. Accordingly, simulations show that the instability affects the BPM readings so that the trajectory control may depend in turn on the wake field effect.
It has been found that a global trajectory correction provided through a Response Matrix algorithm is not sufficient to completely damp the instability; for this reason local trajectory bumps have been applied with success to suppress it. The validity of this trajectory manipulation has been checked in the presence of shot-to-shot trajectory jitter. According to analytical estimates, the trajectory jitter is dominated by the jitter of the launching error and by quadrupole vibrations; the parasitic derivative of dispersion may also provide a contribution.
Threshold values for the longitudinal slices of the bunch have been defined that, if met, will avoid the dilution of the projected emittance in the presence of trajectory jitter. The threshold is given in (18) as the ratio of the standard deviation of the square root of the slice centroid Courant-Snyder amplitude to the square root of the projected emittance. This threshold is a function of the bunch slice number and it represents the expected mismatch of the slice transverse phase space in the presence of trajectory jitter.
For completeness, (3.18) has been compared with other two well known methods for the instability analysis that look, respectively, at the projected emittance growth and at the distortion of the particle distribution (banana shape).
The rms projected emittance growth at the linac end has been evaluated as a function of the launching error. An asymmetry between the horizontal and the vertical plane has emerged.
The jitter of the banana shape has been simulated and the deviation of the bunch head-tail lateral deviation has been calculated. As in the previous case, the instability effect exceeds the threshold only in the vertical plane.
Finally, the jitter of the slice centroid Courant-Snyder amplitude along the bunch has been studied. In this case the projected emittance growth exceeds the given threshold only in the vertical plane. Actually, in both planes only a very small portion of the bunch tail contributes to the instability and thus the transverse phase space mismatch of the majority of the bunch slices is not critically affected by the trajectory jitter. The conclusion is that the trajectory jitter does

not affect the local bumps scheme for the instability suppression; therefore, no important negative effect on the FERMI@Elettra seeded FEL performance is anticipated.

References

[1] S. V. Milton *et al.*, "Exponential gain and saturation of a self-amplified spontaneous emission free-electron laser," *Science*, vol. 292, no. 5524, pp. 2037–2041, 2001.

[2] C. Pellegrini, "High power femtosecond pulses from an x-ray sase-fel," *Nucl. Instr. Meth. Phys. Res. A*, vol. 445, no. 1-3, pp. 124–127, May 2000.

[3] A. Tremaine, X. J. Wang, M. Babzien, I. Ben-Zvi, M. Cornacchia, H.-D. Nuhn, R. Malone, A. Murokh, C. Pellegrini, S. Reiche, J. Rosenzweig, and V. Yakimenko, "Experimental characterization of nonlinear harmonic radiation from a visible self-amplified spontaneous emission free-electron laser at saturation," *Phys. Rev. Lett.*, vol. 88, no. 20, p. 204801, May 2002.

[4] "Linac Coherent Light Source (LCLS) Conceptual Design Report," SLAC, Tech. Rep. SLAC-R-593, 2002.

[5] "TESLA Technical Design Report," DESY, Tech. Rep. DESY-2001-011, 2001.

[6] R. Bonifacio, L. De Salvo Souza, and E. T. Pierini, P. Scharlemann, "Generation of xuv light by resonant frequency tripling in a two-wiggler fel amplifier," *Nucl. Instr. Meth. Phys. Res. A*, vol. 296, no. 1-3, pp. 787–790, Oct 1990.

[7] I. Ben-Zvi, K. M. Yang, and L. H. Yu, "The "fresh-bunch" technique in fels," *Nucl. Instr. Meth. Phys. Res. A*, vol. 318, no. 1-3, pp. 726–729, Jul 1992.

[8] L. H. Yu *et al.*, "High-gain harmonic-generation free-electron laser," *Science*, vol. 289, no. 5481, pp. 932–934, 2000.

[9] G. Penn *et al.*, "Harmonic cascade fel designs for lux," in *Proc. of the Europ. Part. Accel. Conf.*, Lucerne, Switzerland, Jul 2004, p. 488.

[10] A. W. Chao, B. Richter, and C. Y. Yao, "Beam emittance growth caused by transverse deflecting fields in a linear accelerator," *Nucl. Instr. Meth. Phys. Res. A*, vol. 178, p. 1, 1980.

[11] R. Wanzenberg, "Review of beam dyamnics and instabilities in linear colliders," in *Proc. of the 18th Int. Lin. Accel. Conf.*, Geneva, Switzerland, Aug 1996.

[12] R. Assmann, "Beam Dynamics in SLC," in *Proc. of the Part. Accel. Conf.*, Vancouver, Canada, May 1997.

[13] P. Tenenbaum, "Effectiveness of emittance bumps on the NLC and US Cold LC main linear accelerators," SLAC, Tech. Rep. SLAC-TN-04-038, May 2004.

[14] J. T. Seeman, F. J. Decker, and I. Hsu, "The Introduction of trajectory oscillations to reduce emittance growth in the SLC LINAC," in *Proc. of the 15th International Conference on High Energy Accelerators*, Hamburg, Germany, Jul 1992.

[15] C. Adolphsen and T. Raubenheimer, "Method to evaluate steering and alignment algorithms for controlling emittance growth," in *Proc. of the Part. Accel. Conf.*, Washington, USA, 1993, p. 417.

[16] R. Assmann *et al.*, "LIAR: A computer program for the modelling and simulation of high performance linacs," SLAC, Tech. Rep. SLAC-AP-103, Apr 1997.

[17] P. Eliasson and D. Schulte, "Design of main linac emittance tuning bumps for the compact linear collider and the international linear collider," *Phys. Rev. ST Accel. Beams*, vol. 11, no. 1, p. 011002, Jan 2008.

[18] C. Adolphsen *et al.*, "Beam Trajectory Jitter in the SLC Linac," in *Proc. of the Part. Accel. Conf.*, Dallas, Texas, May 1995.

[19] R. Assmann *et al.*, "LIAR - A new program for the modelling and simulation of linear accelerator with high gradients and small emittances," in *Proc. of the 18th Int. Lin. Accel. Conf.*, Geneva, Switzerland, Aug 1996.

[20] G. Guignard *et al.*, "Emittance dilution in 1 and 5 TeV 30 GHz Linear Colliders," in *Proc. of the Europ. Part. Accel. Conf.*, Stockholm, Jun 1998.

[21] N. Leros and D. Schulte, "Dynamics Effects in the Min Linac of CLIC," in *Proc. of the Part. Accel. Conf.*, Chicago, Illinois, USA, Jun 2001.

[22] "FERMI@Elettra Conceptual Design Report," Sincrotrone Trieste, Tech. Rep. ST/F-TN-07/12, 2007.

[23] G. Penn *et al.*, "Effect of Off-Axis Displacement Errors on FEL-1," Sincrotrone Trieste, Tech. Rep. ST/F-TN-06/01, Mar 2006.

[24] G. Guignard, "Stability studies for the CLIC main linac beam," CERN, Tech. Rep. CERN-SL-91-19-AP, Apr 1991.

[25] G. Guignard and J. Hagel, "Multibunch Emittance Preservation in CLIC," in *Proc. of the Europ. Part. Accel. Conf.*, Barcelona, Espana, Jun 1996.

[26] E. T. D'Amico *et al.*, "Simulation package based on placet," in *Proc. of the Part. Accel. Conf.*, Chicago, Illinois, USA, Jun 2001.

[27] J. Resta-Lopez *et al.*, "PLACET Based on Start-to-End Simulations on the ilc with intra-train fast feedback system," in *Proc. of the 11th Europ. Part. Accel. Conf.*, Genoa, Italy, Jun 2008.

[28] P. Craievich and S. Di Mitri, "Emiitance growth due to short range transverse wakefields in the fermi linac," in *Proc. of the 27th Int. Conf. on FEL*, Palo Alto, California, Aug 2005.

[29] S. Di Mitri and P. Craievich, "Beam break-up instability in the fermi@elettra linac," in *Proc. of the 10th Europ. Part. Accel. Conf.*, Edinburgh, Scotland, Jun 2006.

[30] M. Borland, APS, Tech. Rep. APS LS-287, 2000.

[31] J. Delayen, *Phys. Rev. ST Accel. Beams*, vol. 6, p. 084402, 2003.

[32] ——, *Phys. Rev. ST Accel. Beams*, vol. 7, p. 077702, 2004.

[33] A. W. Chao, *Physics of collective beam instabilities in high-energy accelerators.* New York: Wiley, 1993.

[34] P. Craievich, I. Zagorodnov, and T. Weiland, "The short-range wakeelds in the BTW accelerating structure of the ELETTRA linac," *Nucl. Inst. Meth. Phys. Res. A*, vol. 558, p. 58, 2006.

[35] S. Di Mitri and A. A. Zholents, "Trajectory Correction in the Fermi@Elettra Linac," in *Proc. of the 11th Europ. Part. Accel. Conf.*, Genoa, Italy, Jun 2008.

[36] S. Di Mitri, "Trajectory Correction in the FERMI@Elettra Linac," Sincrotrone Trieste, Tech. Rep. ST/F-TN-07/06, May 2007.

[37] M. Cornacchia, S. Di Mitri, G. Penco, and A. A. Zholents, "Formation of electron bunches for harmonic cascade x-ray free electron lasers," *Phys. Rev. ST Accel. Beams*, vol. 9, p. 120701, 2006.

[38] E. L. Saldin, E. A. Schneidmiller, and M. V. Yurkov, "On the coherent radiation of an electron bunch moving in an arc of a circle," *Nucl. Instr. Meth. Phys. Res. A*, vol. 398, no. 2-3, pp. 373–394, Oct 1997.

[39] M. Borland *et al.*, "Start-to-end simulation of self-amplified spontaneous emission free electron lasers from the gun through the undulator," *Nucl. Instr. Meth. Phys. Res. A*, vol. 483, no. 1-2, pp. 268–272, May 2002.

[40] R. Assmann and A. W. Chao, "Dispersion in the Presence of Strong Transverse Wake Fields," in *Proc. of the Europ. Part. Accel. Conf.*, Stockholm, Jun 1998.

[41] P. Craievich *et al.*, "A transverse RF deflecting cavity for the FERMI@Elettra project," in *Proc. of the 8th European Workshop on Beam Diagnostics and Instrumentation for Particle Accelerator*, Mestre, Italy, May 2007.

Chapter 4

Wakefield induced energy spread in the undulator vacuum chamber

Abstract
Within the ultra-relativistic limit, analytical expressions are found for the high-frequency resistive-wall coupling impedance of an elliptical cross-section vacuum chamber. Subsequently the corresponding wake functions are derived by performing inverse Fourier transformations numerically. The electromagnetic fields have been developed working out two systems of solutions, namely for the vacuum and for the resistive-wall. The constants involved in these systems have been determined by matching boundary conditions at the interface vacuum-wall. Several study cases have been considered as concerns the aspect ratio of the elliptical cross-section and the transverse position of the leading charge in order to exemplify the behaviour of the longitudinal and transverse wake functions[1].
Estimations of the induced energy-spread caused by the resistive wall and surface roughness wakefields along the FERMI FEL 1 undulator are presented. The energy spread and losses induced by resistive wall wakefield are determined for three possible transverse geometries of the vacuum chamber, namely circular, rectangular and elliptic cross-section, while the energy spread and losses induced by the surface roughness wakefields are obtained for the circular cross-section case[2].

[1]P. Craievich, A. Lutman and R. Vescovo, "Electromagnetic field and short-range wake function in a beam pipe of elliptical cross section," *Phys. Rev. ST Accel. Beams*, vol. 11, n. 7, p. 074401, 2008.

[2]P. Craievich, C. Bontoiu, M. Castronovo, A.A. Lutman, L. Rumiz, R. Vescovo, "Wakefield Induced Energy Spread in the FERMI Undulator", in *Proceedings of the 29th International FEL Conference*, Novosibirsk, Russia, p. 347, 2007.

4.1 Introduction

Free electron laser (FEL) projects aim to achieve high-brightness photon beam pulses of minimum bandwidth. However such pulses may be corrupted by possible large wakefields along the undulator small-gap vacuum chamber. Thus, knowledge of the short-range wakefields in the undulator vacuum chamber is needed to predict the beam quality in terms of the single bunch energy spread and emittance. A possible choice for a small-gap vacuum chamber is one with elliptical cross section, for which there are references to analytically derived expressions for the low-frequency resistive-wall coupling impedance (see for example [1–3]). Expressions for the high frequency resistive wall impedance are given, in case of DC conductivity model, for a round pipe in [4], and for the conducting parallel plates in [5]. Adopting the AC conductivity model [6], the resistive wall impedance is given for the round pipe in [7] and for the parallel plates in [8]. The problem of calculating the coupling impedance, including the high frequencies, of a resistive beam pipe with arbitrary cross section has been solved by Yokoya [9] with the boundary element method. He applied the method to numerically work out the solution in the case of an elliptical pipe, moreover the method can be applied using both AC and DC conductivity models.
In this paper we analytically derive expressions for the longitudinal and transverse resistive-wall coupling impedance of a vacuum chamber with elliptical cross section using another method, precisely the field matching method, and make a comparison with the results obtained with the boundary element method on the same geometry. The paper is organized as follows. In section II we describe the physical model used to obtain the expressions of the electromagnetic fields inside the vacuum and inside the resistive parts of the beam pipe, respectively. We use elliptical coordinates and write the field components in term of Fourier transformations. In the sections III we work out the Maxwell equations to derive a series expression of the e.m. field in the vacuum part, while in section IV we derive a series expansion of the e.m. field in the resistive part of the beam pipe. In Section V, the constants involved in the two series expansions are determined by imposing the boundary conditions at the interface vacuum-resistive wall. This fully determines the field components. In section VI we derive the expressions of the longitudinal and transverse resistive-wall impendances, and the short range wake functions are then obtained by calculating numerically the inverse Fourier transformations of the impedances. In section VII applications and examples are illustrated, involving different aspect ratios of the cross section, different materials using both AC and DC conductivity models and different leading and trailing charges displacement from the beam pipe axis.

4.2 Physical model description

Let us consider an elliptical cross-section pipe with finite conductivity σ and infinite wall thickness, and denote with a the major half-axis of the ellipse and with b the minor one, respectively. Figure 4.1 shows cross section and longitudinal section of the beam pipe, and the travelling point charge with the elliptic cylindrical (u, v, s) coordinates system, where the s-axis coincides with the pipe axis. The relations between the Cartesian and the elliptical coordinates are given in [10] and are illustrated in figure 4.2. The equation $u = u_0$ defines the surface separating the vacuum region from the resistive wall. The vacuum region is specified by $u < u_0$ while the metal region by $u > u_0$. The leading point charge, travelling along the beam pipe, is assumed to be ultra-relativistic, and its longitudinal position is $s = ct$, where c is the velocity of light in vacuum, while its transverse

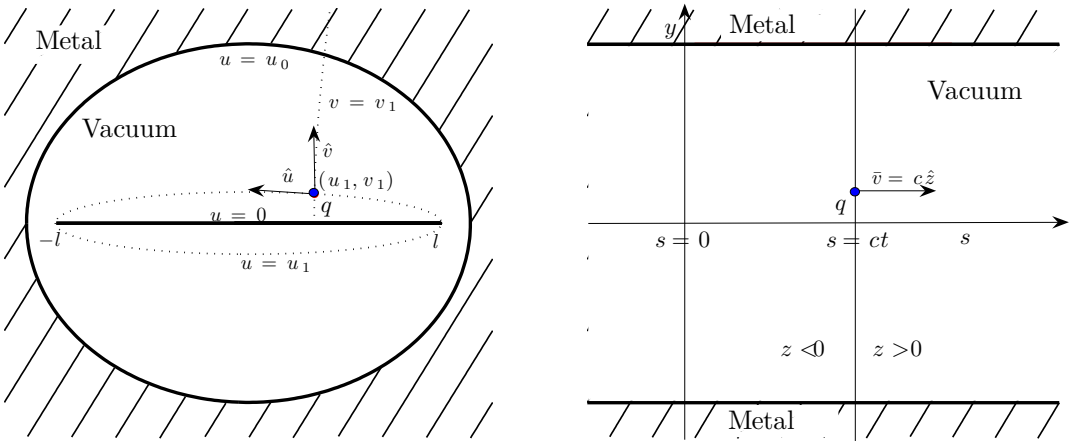

Figure 4.1: s-y plane view and cross-section plane view.

coordinates are (u_1, v_1).

4.3 Fields in the vacuum

Using the elliptical cylindrical coordinates system $O(u, v, s)$, the Maxwell's equations in the vacuum region, can be written as follows, denoting the electric field components with E_u, E_v and E_s, and the magnetic field components B_u, B_v and B_s:

$$\frac{1}{h^2}\frac{\partial hE_u}{\partial u} + \frac{1}{h^2}\frac{\partial hE_v}{\partial v} + \frac{\partial E_s}{\partial s} = \frac{\rho}{\epsilon_0}, \tag{4.1a}$$

$$\frac{1}{h}\frac{\partial E_s}{\partial v} - \frac{\partial E_v}{\partial s} = -\frac{\partial B_u}{\partial t}, \tag{4.1b}$$

$$\frac{\partial E_u}{\partial s} - \frac{1}{h}\frac{\partial E_s}{\partial u} = -\frac{\partial B_v}{\partial t}, \tag{4.1c}$$

$$\frac{1}{h^2}\frac{\partial hE_v}{\partial u} - \frac{1}{h^2}\frac{\partial hE_u}{\partial v} = -\frac{\partial B_s}{\partial t}, \tag{4.1d}$$

$$\frac{1}{h^2}\frac{\partial hB_u}{\partial u} + \frac{1}{h^2}\frac{\partial hB_v}{\partial v} + \frac{\partial B_s}{\partial s} = 0, \tag{4.1e}$$

$$\frac{1}{h}\frac{\partial B_s}{\partial v} - \frac{\partial B_v}{\partial s} = \frac{1}{c^2}\frac{\partial E_u}{\partial t}, \tag{4.1f}$$

$$\frac{\partial B_u}{\partial s} - \frac{1}{h}\frac{\partial B_s}{\partial u} = \frac{1}{c^2}\frac{\partial E_v}{\partial t}, \tag{4.1g}$$

$$\frac{1}{h^2}\frac{\partial hB_v}{\partial u} - \frac{1}{h^2}\frac{\partial hB_u}{\partial v} = \frac{1}{c^2}\frac{\partial E_s}{\partial t} + \mu_0 J. \tag{4.1h}$$

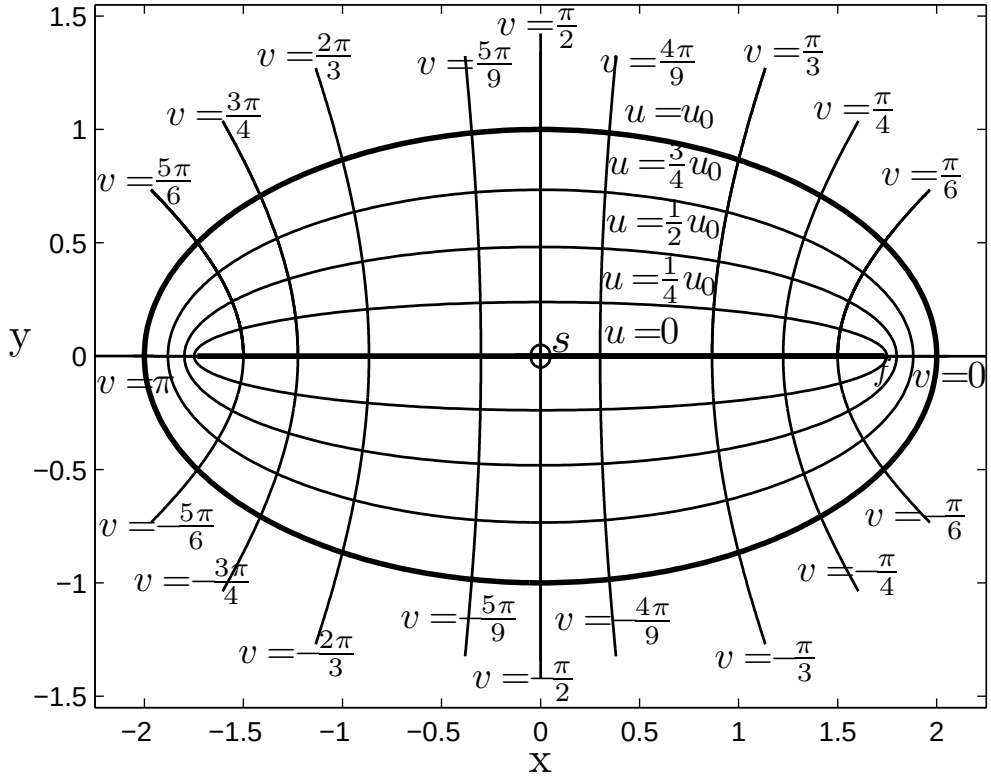

Figure 4.2: Elliptic cylindrical (u, v, s) and a Cartesian orthogonal (x, y, s) coordinates system.

where h is the metric while the charge and current density are:

$$\rho = q\frac{\delta(s-ct)\delta(u-u_1)\delta(v-v_1)}{h^2}, \tag{4.2a}$$

$$\boldsymbol{J} = qc\frac{\delta(s-ct)\delta(u-u_1)\delta(v-v_1)}{h^2}\hat{s}. \tag{4.2b}$$

In addition, we refer to the coordinate $z = s - ct$, which is the longitudinal displacement from the point charge. Thus it is $z < 0$ behind the leading charge and $z > 0$ ahead of it. Due to the causality principle, all fields must vanish for $z > 0$.
Using the same approach adopted in [4], we write the field vectors $\boldsymbol{E} = (E_u, E_v, E_z)$ and $\boldsymbol{B} = (B_u, B_v, B_z)$ in terms of the Fourier transformed vectors $\tilde{\boldsymbol{E}}$, $\tilde{\boldsymbol{B}}$ on the z-axis:

$$(\boldsymbol{E}, \boldsymbol{B}) = \frac{1}{2\pi}\int_{-\infty}^{+\infty}(\tilde{\boldsymbol{E}}, \tilde{\boldsymbol{B}})e^{ikz}dk. \tag{4.3}$$

Substituting Eq. (4.2a) into Eq. (4.1a) and Eq. (4.2b) into Eq. (4.1h) the equations in (4.1), one obtain the following system of six equations:

$$\frac{\partial \tilde{E}_z}{\partial v} = c\frac{\partial \tilde{B}_z}{\partial u}, \tag{4.4a}$$

$$\frac{\partial \tilde{E}_z}{\partial u} = -c\frac{\partial \tilde{B}_z}{\partial v}, \tag{4.4b}$$

$$\frac{\partial h\tilde{E}_u}{\partial u} - \frac{\partial ch\tilde{B}_u}{\partial v} = \frac{q}{\epsilon_0}\delta(u-u_1)\delta(v-v_1) + \\ -ikh^2\tilde{E}_z + \frac{i}{k}\frac{\partial^2 \tilde{E}_z}{\partial v^2}, \tag{4.4c}$$

$$c\frac{\partial h\tilde{B}_u}{\partial u} + \frac{\partial h\tilde{E}_u}{\partial v} = -ikh^2 c\tilde{B}_z + \frac{ic}{k}\frac{\partial^2 \tilde{B}_z}{\partial v^2}, \tag{4.4d}$$

$$\tilde{E}_v = -\frac{i}{hk}\frac{\partial \tilde{E}_z}{\partial v} - c\tilde{B}_u, \tag{4.4e}$$

$$c\tilde{B}_v = -\frac{ic}{hk}\frac{\partial \tilde{B}_z}{\partial v} + \tilde{E}_u. \tag{4.4f}$$

Starting from Eqs. (4.4a) and (4.4b), and following the approach described in [10], the longitudinal components of the electric and magnetic fields can be written as follows:

$$\tilde{E}_z = A_0 + \sum_{n=1}^{+\infty} A_n \cosh nu \cos nv + \sum_{n=1}^{+\infty} B_n \sinh nu \sin nv, \tag{4.5a}$$

$$c\tilde{B}_z = B_0 + \sum_{n=1}^{+\infty} B_n \cosh nu \cos nv - \sum_{n=1}^{+\infty} A_n \sinh nu \sin nv, \tag{4.5b}$$

where A_n and B_n are constants to be determined.
Starting from Eqs. (4.4c) and (4.4d) and using the solutions in (4.5), the approach described in [10] yields the following expressions for the transverse fields $\tilde{E}_u$ and $\tilde{B}_u$:

$$h\tilde{E}_u(u,v) = K_{\tilde{E}u} + S^c_{\tilde{E}u} + S^s_{\tilde{E}u} + S^q_{\tilde{E}u}, \tag{4.6a}$$

$$hc\tilde{B}_u(u,v) = K_{\tilde{B}u} + S^c_{\tilde{B}u} + S^s_{\tilde{B}u} + S^q_{\tilde{B}u}, \tag{4.6b}$$

where denoting with $H(u)$ the Heaviside step function and letting $W = ik(a^2 - b^2)$ we can write:

$$K_{\tilde{E}u} = \sum_{n=1}^{+\infty}\left(E_n - \frac{ni}{k}B_n\right)\cosh nu \sin nv + \sum_{n=1}^{+\infty} F_n \sinh nu \cos nv, \tag{4.7a}$$

$$K_{\tilde{B}u} = \sum_{n=1}^{+\infty}\left(F_n + \frac{ni}{k}A_n\right)\cosh nu \sin nv - \sum_{n=1}^{+\infty} E_n \sinh nu \cos nv, \tag{4.7b}$$

$$S^c_{\tilde{E}u} = -A_0 W\frac{\sinh 2u}{4} + \frac{A_1 W}{16}\left(\sinh u \cos 3v - \sinh 3u \cos v\right) + W\sum_{n=2}^{+\infty} A_n \frac{\sinh nu}{8(n+1)}\cos(n+2)v + \\ + W\sum_{n=2}^{+\infty} A_n \frac{\sinh nu}{8(n-1)}\cos(n-2)v - W\sum_{n=2}^{+\infty} A_n\left[\frac{\sinh(n+2)u}{8(n+1)} + \frac{\sinh(n-2)u}{8(n-1)}\right]\cos nv, \tag{4.7c}$$

$$S^s_{\tilde{E}u} = +B_0 W \frac{\sin 2v}{4} + \frac{B_1 W}{16}\left(\cosh u \sin 3v - \cosh 3u \sin v\right) + W\sum_{n=2}^{+\infty} B_n \frac{\cosh nu}{8(n+1)} \sin\left(n+2\right)v + \\ + W\sum_{n=2}^{+\infty} B_n \frac{\cosh nu}{8(n-1)} \sin\left(n-2\right)v - W\sum_{n=2}^{+\infty} B_n \Big[\frac{\cosh\left(n+2\right)u}{8(n+1)} + \frac{\cosh\left(n-2\right)u}{8(n-1)}\Big] \sin nv, \quad (4.7d)$$

$$S^c_{\tilde{B}u} = -B_0 W \frac{\sinh 2u}{4} + \frac{B_1 W}{16}\left(\sinh u \cos 3v - \sinh 3u \cos v\right) + W\sum_{n=2}^{+\infty} B_n \frac{\sinh nu}{8(n+1)} \cos\left(n+2\right)v \\ + W\sum_{n=2}^{+\infty} B_n \frac{\sinh nu}{8(n-1)} \cos\left(n-2\right)v - W\sum_{n=2}^{+\infty} B_n \Big[\frac{\sinh\left(n+2\right)u}{8(n+1)} + \frac{\sinh\left(n-2\right)u}{8(n-1)}\Big] \cos nv, \quad (4.7e)$$

$$S^s_{\tilde{B}u} = -A_0 W \frac{\sin 2v}{4} + \frac{A_1 W}{16}\left(\cosh 3u \sin v - \cosh u \sin 3v\right) - W\sum_{n=2}^{+\infty} A_n \frac{\cosh nu}{8(n+1)} \sin\left(n+2\right)v + \\ - W\sum_{n=2}^{+\infty} A_n \frac{\cosh nu}{8(n-1)} \sin\left(n-2\right)v + W\sum_{n=2}^{+\infty} A_n \Big[\frac{\cosh\left(n+2\right)u}{8(n+1)} + \frac{\cosh\left(n-2\right)u}{8(n-1)}\Big] \sin nv, \quad (4.7f)$$

$$S^q_{\tilde{E}u} = \frac{q}{2\pi\epsilon_0} H(u-u_1) \\ + \sum_{n=1}^{+\infty} \frac{q}{\pi\epsilon_0} \cos nv_1 \left[H(u-u_1)\cosh nu_1 \cosh nu + H(u_1-u)\sinh nu_1 \sinh nu\right] \cos nv \\ - \sum_{n=1}^{+\infty} \frac{q}{\pi\epsilon_0} \sin nv_1 \Big[H(u-u_1)\sinh nu_1 \sinh nu + H(u_1-u)\cosh nu_1 \cosh nu\Big] \sin nv, \quad (4.7g)$$

$$S^q_{\tilde{B}u} = \sum_{n=1}^{+\infty} \frac{q}{\pi\epsilon_0} \sin nv_1 \Big[H(u-u_1)\sinh nu_1 \cosh nu + H(u_1-u)\cosh nu_1 \sinh nu\Big] \cos nv \\ + \sum_{n=1}^{+\infty} \frac{q}{\pi\epsilon_0} \cos nv_1 \Big[H(u-u_1)\cosh nu_1 \sinh nu + H(u_1-u)\sinh nu_1 \cosh nu\Big] \sin nv. \quad (4.7h)$$

The field components $\tilde{E}_v$ and $\tilde{B}_v$ can be directly obtained from Eqs. (4.4e) and (4.4f) using the solutions (4.5) and (4.6), yielding:

$$h\tilde{E}_v = K_{\tilde{E}v} + S^c_{\tilde{E}v} + S^s_{\tilde{E}v} + S^q_{\tilde{E}v}, \quad (4.8a)$$

$$hc\tilde{B}_v = K_{\tilde{B}v} + S^c_{\tilde{B}v} + S^s_{\tilde{B}v} + S^q_{\tilde{B}v}. \quad (4.8b)$$

where:

$$K_{\tilde{E}v} = -K_{\tilde{B}u}, \tag{4.9a}$$

$$S^s_{\tilde{E}v} = -S^s_{\tilde{B}u} + \sum_{n=1}^{+\infty} \frac{ni}{k} A_n \cosh nu \sin nv, \tag{4.9b}$$

$$S^c_{\tilde{E}v} = -S^c_{\tilde{B}u} - \sum_{n=1}^{+\infty} \frac{ni}{k} B_n \sinh nu \cos nv, \tag{4.9c}$$

$$S^q_{\tilde{E}v} = -S^q_{\tilde{B}u}, \tag{4.9d}$$

$$K_{\tilde{B}v} = +K_{\tilde{E}u}, \tag{4.9e}$$

$$S^s_{\tilde{B}v} = +S^s_{\tilde{E}u} + \sum_{n=1}^{+\infty} \frac{ni}{k} B_n \cosh nu \sin nv, \tag{4.9f}$$

$$S^c_{\tilde{B}v} = +S^c_{\tilde{E}u} + \sum_{n=1}^{+\infty} \frac{ni}{k} A_n \sinh nu \cos nv, \tag{4.9g}$$

$$S^q_{\tilde{B}v} = +S^q_{\tilde{E}u}. \tag{4.9h}$$

4.4 Fields in the resistive wall

The constants A_n, B_n, E_n and F_n will be determined by imposing the boundary conditions at the surface separating the vacuum from the resistive-wall. To this aim we need to calculate the expressions of the fields inside the wall ($u > u_0$). In the conductor we assume that:

$$\rho = 0, \tag{4.10a}$$

$$\boldsymbol{J} = \sigma \boldsymbol{E}, \tag{4.10b}$$

where σ is the conductivity of the metal. Furthermore, the Maxwell equations can be written as:

$$\frac{1}{h^2}\frac{\partial h E_u}{\partial u} + \frac{1}{h^2}\frac{\partial h E_v}{\partial v} + \frac{\partial E_s}{\partial s} = 0, \tag{4.11a}$$

$$\frac{1}{h}\frac{\partial E_s}{\partial v} - \frac{\partial E_v}{\partial s} = -\frac{\partial B_u}{\partial t}, \tag{4.11b}$$

$$\frac{\partial E_u}{\partial s} - \frac{1}{h}\frac{\partial E_s}{\partial u} = -\frac{\partial B_v}{\partial t}, \tag{4.11c}$$

$$\frac{1}{h^2}\frac{\partial h E_v}{\partial u} - \frac{1}{h^2}\frac{\partial h E_u}{\partial v} = -\frac{\partial B_s}{\partial t}, \tag{4.11d}$$

$$\frac{1}{h^2}\frac{\partial h B_u}{\partial u} + \frac{1}{h^2}\frac{\partial h B_v}{\partial v} + \frac{\partial B_s}{\partial s} = 0, \tag{4.11e}$$

$$\frac{1}{h}\frac{\partial B_s}{\partial v} - \frac{\partial B_v}{\partial s} = \frac{1}{c^2}\frac{\partial E_u}{\partial t} + \mu_0 \sigma E_u, \tag{4.11f}$$

$$\frac{\partial B_u}{\partial s} - \frac{1}{h}\frac{\partial B_s}{\partial u} = \frac{1}{c^2}\frac{\partial E_v}{\partial t} + \mu_0 \sigma E_v, \tag{4.11g}$$

$$\frac{1}{h^2}\frac{\partial h B_v}{\partial u} - \frac{1}{h^2}\frac{\partial h B_u}{\partial v} = \frac{1}{c^2}\frac{\partial E_s}{\partial t} + \mu_0 \sigma E_s. \tag{4.11h}$$

Using the variable $z = s - ct$ and manipulating Eqs. (4.11) yields equations:

$$\frac{\partial^2}{\partial u^2}\tilde{E}_z + \frac{\partial^2}{\partial v^2}\tilde{E}_z + h^2\lambda^2\tilde{E}_z = 0, \tag{4.12a}$$

$$\frac{\partial^2}{\partial u^2}c\tilde{B}_z + \frac{\partial^2}{\partial v^2}c\tilde{B}_z + h^2\lambda^2 c\tilde{B}_z = 0, \tag{4.12b}$$

$$h\tilde{E}_u = \frac{ik}{\lambda^2}\frac{\partial}{\partial u}\tilde{E}_z + \frac{ik}{\lambda^2}\frac{\partial}{\partial v}c\tilde{B}_z, \tag{4.12c}$$

$$h\tilde{E}_v = \frac{ik}{\lambda^2}\frac{\partial}{\partial v}\tilde{E}_z - \frac{ik}{\lambda^2}\frac{\partial}{\partial u}c\tilde{B}_z, \tag{4.12d}$$

$$ch\tilde{B}_u = -\Big[\frac{ik}{\lambda^2} + \frac{i}{k}\Big]\frac{\partial}{\partial v}\tilde{E}_z + \frac{ik}{\lambda^2}\frac{\partial}{\partial u}c\tilde{B}_z, \tag{4.12e}$$

$$ch\tilde{B}_v = \Big[\frac{ik}{\lambda^2} + \frac{i}{k}\Big]\frac{\partial}{\partial u}\tilde{E}_z + \frac{ik}{\lambda^2}\frac{\partial}{\partial v}c\tilde{B}_z. \tag{4.12f}$$

where $\lambda^2 = ikZ_0\sigma$ and λ is chosen with positive imaginary part.

4.4.1 Longitudinal fields in the conductor

Each of Eqs. (4.12a) and (4.12b) can be solved by separating the variables u and v, that is assuming the unknown is proportional to the product between two functions $U(u)$ and $V(v)$. Substituting the product $U(u)V(v)$

$$\frac{d^2}{dv^2}V + \Big[a - 2Q\cos 2v\Big]V = 0, \tag{4.13a}$$

$$\frac{d^2}{du^2}U - \Big[a - 2Q\cosh 2u\Big]U = 0, \tag{4.13b}$$

where $Q = l^2\lambda^2/4$ and a is a separation constant.
Eqs. (4.13a) and (4.13b) are called the Mathieu angular and radial equations, respectively [11]. On the other hand, the electric and magnetic fields, as well as the function $V(v)$, must be 2π-periodic in v. There is a countable infinity of values of the constant a that allow 2π-periodic solutions in v. Such values are called the Mathieu Characteristic Numbers (MCNs), and can be calculated with the algorithms in [12]. In particular, for imaginary values of Q (i.e., in the case of DC conductivity), an useful algorithm can be found in [13].
Adopting the standard notation for the MCNs [14], the constants a_{2n} and a_{2n+1} $(n \geq 0)$ produce even π-periodic and 2π- periodic solutions respectively, while the constants b_{2n} $(n \geq 1)$ and b_{2n+1} $(n \geq 0)$ produce odd π-periodic and 2π-periodic solutions respectively.

Furthermore the possible solutions $V(v)$ can be written as:

$$V_{a_{2n}}(v) = \sum_{m=0}^{+\infty} A_{2m}^{a_{2n}} \cos 2mv, \tag{4.14a}$$

$$V_{a_{2n+1}}(v) = \sum_{m=0}^{+\infty} A_{2m+1}^{a_{2n+1}} \cos (2m+1)v, \tag{4.14b}$$

$$V_{b_{2n}}(v) = \sum_{m=1}^{+\infty} B_{2m}^{b_{2n}} \sin 2mv, \tag{4.14c}$$

$$V_{b_{2n+1}}(v) = \sum_{m=0}^{+\infty} B_{2m+1}^{b_{2n+1}} \sin (2m+1)v, \tag{4.14d}$$

where the Fourier coefficients can be calculated by recursion formulas [14].
It is worth noting that, for each of the solutions in (4.14), the other linearly independent solution of the Mathieu angular equation, for a fixed MCN, is not periodic in v [11], thus can be discarded. The Mathieu radial equation has two linearly independent solutions for every MCN. They are called the first and the second kind radial Mathieu functions, respectively, and can be expressed as series of products of Bessel functions [12].
Since we are interested in damped solutions inside the conductor, a proper linear combination of the solutions of first and second kind has to be chosen. The damped solutions required for a complex Q are:

$$U_{a_{2n}}(u,Q) = \sum_{m=0}^{+\infty} (-1)^{m+n} A_{2m}^{2n} \times \Big[J_{m-n}(w_1) H_{m+n}^{(1)}(w_2) + J_{m+n}(w_1) H_{m-n}^{(1)}(w_2) \Big], \tag{4.15a}$$

$$U_{a_{2n+1}}(u,Q) = \sum_{m=0}^{+\infty} (-1)^{m+n} A_{2m+1}^{2n+1} \times \Big[J_{m-n}(w_1) H_{m+n+1}^{(1)}(w_2) + J_{m+n+1}(w_1) H_{m-n}^{(1)}(w_2) \Big], \tag{4.15b}$$

$$U_{b_{2n}}(u,Q) = \sum_{m=1}^{+\infty} (-1)^{m+n} B_{2m}^{2n} \times \Big[J_{m-n}(w_1) H_{m+n}^{(1)}(w_2) - J_{m+n}(w_1) H_{m-n}^{(1)}(w_2) \Big], \tag{4.15c}$$

$$U_{b_{2n+1}}(u,Q) = \sum_{m=0}^{+\infty} (-1)^{m+n} B_{2m+1}^{2n+1} \times \Big[J_{m-n}(w_1) H_{m+n+1}^{(1)}(w_2) - J_{m+n+1}(w_1) H_{m-n}^{(1)}(w_2) \Big]. \tag{4.15d}$$

where J_n is the Bessel function of the first kind of n-th order, $H_n^{(1)}$ is the Hankel function of first kind of n-th order, $w_1 = \sqrt{Q} e^{-u}$ and $w_2 = \sqrt{Q} e^{u}$, $\sqrt{Q}$ having positive imaginary part.

Being proportional to $U(u)V(v)$, the unknowns $\tilde{E}_z$ and $c\tilde{B}_z$, can be finally expressed as:

$$\begin{aligned}\tilde{E}_z = &\sum_{n=0}^{+\infty} C_{a_n}^E\, U_{a_n}(u) \sum_{m=0}^{+\infty} A_m^{a_n} \cos mv + \\ &+ \sum_{n=1}^{+\infty} D_{b_n}^E\, U_{b_n}(u) \sum_{m=1}^{+\infty} B_m^{b_n} \sin mv, \end{aligned} \tag{4.16a}$$

$$\begin{aligned}c\tilde{B}_z = &\sum_{n=0}^{+\infty} C_{a_n}^B\, U_{a_n}(u) \sum_{m=0}^{+\infty} A_m^{a_n} \cos mv + \\ &+ \sum_{n=1}^{+\infty} D_{b_n}^B\, U_{b_n}(u) \sum_{m=1}^{+\infty} B_m^{b_n} \sin mv, \end{aligned} \tag{4.16b}$$

where the constants $C_{a_n}^E$, $D_{b_n}^E$, $C_{a_n}^B$, $D_{b_n}^B$ are to be determined.

4.4.2 Transverse fields in the conductor

The transverse fields in the conductor can be directly calculated by substituting Eqs. (4.16a) and (4.16b) into Eqs. (4.12c), (4.12d), (4.12e) and (4.12f). As in the following only tangential fields are involved, we give only the expressions for $h\tilde{E}_v$ and $ch\tilde{B}_v$

$$\begin{aligned}h\tilde{E}_v = \sum_{n=0}^{+\infty} \Big[&-\frac{ik}{\lambda^2} C_{a_n}^E U_{a_n} \sum_{m=1}^{+\infty} m A_m^{a_n} \sin mv \\ &-\frac{ik}{\lambda^2} C_{a_n}^B U'_{a_n} \sum_{m=0}^{+\infty} A_m^{a_n} \cos mv \Big] + \\ + \sum_{n=1}^{+\infty} \Big[&\frac{ik}{\lambda^2} D_{b_n}^E U_{b_n} \sum_{m=1}^{+\infty} m B_m^{b_n} \cos mv \\ &-\frac{ik}{\lambda^2} D_{b_n}^B U'_{b_n} \sum_{m=1}^{+\infty} B_m^{b_n} \sin mv \Big], \end{aligned} \tag{4.17a}$$

$$\begin{aligned}ch\tilde{B}_v = \sum_{n=0}^{+\infty} \Big[&\Big(\frac{ik}{\lambda^2} + \frac{i}{k}\Big) C_{a_n}^E U'_{a_n} \sum_{m=0}^{+\infty} A_m^{a_n} \cos mv \\ &-\frac{ik}{\lambda^2} C_{a_n}^B U_{a_n} \sum_{m=1}^{+\infty} m A_m^{a_n} \sin mv \Big] + \\ + \sum_{n=1}^{+\infty} \Big[&\Big(\frac{ik}{\lambda^2} + \frac{i}{k}\Big) D_{b_n}^E U'_{b_n} \sum_{m=1}^{+\infty} B_m^{b_n} \sin mv \\ &+\frac{ik}{\lambda^2} D_{b_n}^B U_{b_n} \sum_{m=1}^{+\infty} m B_m^{b_n} \cos mv \Big]. \end{aligned} \tag{4.17b}$$

4.5 Evaluation of the constants

The constants involved in the field expressions are determined by satisfying the boundary conditions at $u = u_0$, separating the vacuum from the resistive-wall.
Precisely, the continuity of $\tilde{E}_z$, $h\tilde{E}_v$, $c\tilde{B}_z$ and $hc\tilde{B}_v$, the field components tangential to the surface $u = u_0$, is imposed. As a result, the constants A_{2n}, A_{2n+1}, B_{2n} and B_{2n+1} can be calculated by solving through four independent tri-diagonal linear systems. More details about the estimation of the linear system can be found in [10]. Truncating every tri-diagonal linear system at the (M+1)-th order we obtain:

$$\begin{pmatrix} d_0 & z_0 & & & \\ s_0 & d_1 & z_1 & & \\ & s_1 & \ddots & \ddots & \\ & & \ddots & \ddots & z_{M-1} \\ & & & s_{M-1} & d_M \end{pmatrix} \begin{pmatrix} X_0 \\ X_1 \\ \vdots \\ \vdots \\ X_M \end{pmatrix} = \begin{pmatrix} t_0 \\ t_1 \\ \vdots \\ \vdots \\ t_M \end{pmatrix} \tag{4.18}$$

Since the coefficients on the diagonals are not zero the system can be easily determined by Gaussian elimination without pivoting. Thus, the following recursive formula can be used to obtain the coefficients:

$$X_M = \frac{T^c_M}{C_M}, \tag{4.19}$$

$$X_n = \frac{T^c_n - z_n X_{n+1}}{C_n}. \tag{4.20}$$

where

$$\begin{aligned} C_n &= \begin{cases} d_0 & n = 0 \\ d_n - \dfrac{s_{n-1} z_{n-1}}{C_{n-1}} & n = 1..M \end{cases} \\ D_n &= \frac{s_{n-1}}{C_{n-1}} \qquad n = 1..M \\ T^c_n &= \begin{cases} t_0 & n = 0 \\ t_n - T^c_{n-1} D_n & n = 1..M \end{cases} \end{aligned} \tag{4.21}$$

Introducing the quantities $l = \sqrt{a^2 - b^2}$, $W = ikl^2$, $\lambda^2 = ikZ_0\sigma$, $R(u_0) = il\lambda \cosh u_0$, the coefficients s_n, d_n, z_n and t_n on the diagonals are given by the following relations for each system:

A. System involving the constants A_{2n}

$$
\begin{aligned}
d_0 &= -\frac{W}{4}\sinh 2u_0 - R(u_0)\Big[\frac{ik}{\lambda^2}+\frac{i}{k}\Big],\\
d_n &= -W\Big[\frac{\sinh(2n+2)u_0}{(16n+8)\sinh 2nu_0}+\frac{\cosh(2n+2)u_0}{(16n+8)\cosh 2nu_0}\\
&\quad +\frac{\sinh(2n-2)u_0}{(16n-8)\sinh 2nu_0}+\frac{\cosh(2n-2)u_0}{(16n-8)\cosh 2nu_0}\Big]\\
&\quad +\frac{2ni}{k}-\frac{i}{k}R(u_0)\coth 2nu_0-\frac{ik}{\lambda^2}\Big[R(u_0)\Big(\tanh 2nu_0+\coth 2nu_0\Big)-4n\Big] \qquad n\geq 1,\\
z_0 &= \frac{W}{8}\sinh 2u_0,\\
z_n &= \frac{W}{16n+8}\Big[\frac{\sinh(2n+2)u_0}{\sinh 2nu_0}+\frac{\cosh(2n+2)u_0}{\cosh 2nu_0}\Big] \qquad n\geq 1,\\
s_0 &= \frac{W}{4}\frac{1}{\cosh 2u_0},\\
s_n &= \frac{W}{16n-8}\Big[\frac{\sinh(2n-2)u_0}{\sinh 2nu_0}+\frac{\cosh(2n-2)u_0}{\cosh 2nu_0}\Big] \qquad n\geq 1,\\
t_0 &= -\frac{q}{2\pi\epsilon_0},\\
t_n &= \frac{q}{\pi\epsilon_0}\cos 2nv_1\cosh 2nu_1\Big[\tanh 2nu_0-\coth 2nu_0\Big] \qquad n\geq 1.
\end{aligned}
\tag{4.22}
$$

B. System involving the constants A_{2n+1}

$$
\begin{aligned}
d_0 &= -\frac{W}{16}\Big[\frac{\sinh 3u_0}{\sinh u_0}+\frac{\cosh 3u_0}{\cosh u_0}\Big]\\
&\quad +\frac{i}{k}-\frac{i}{k}R(u_0)\coth u_0-\frac{ik}{\lambda^2}\Big[R(u_0)\Big(\tanh u_0+\coth u_0\Big)-2\Big],\\
d_n &= -\frac{W}{16(n+1)}\Big[\frac{\sinh(2n+3)u_0}{\sinh(2n+1)u_0}+\frac{\cosh(2n+3)u_0}{\cosh(2n+1)nu_0}\Big]\\
&\quad -\frac{W}{16n}\Big[\frac{\sinh(2n-1)u_0}{\sinh(2n+1)nu_0}+\frac{\cosh(2n-1)u_0}{\cosh(2n+1)u_0}\Big],\\
&\quad +\frac{(2n+1)i}{k}-\frac{i}{k}\frac{R(u_0)}{\tanh(2n+1)u_0}\\
&\quad -\frac{ik}{\lambda^2}\Big[R(u_0)\Big(\tanh(2n+1)u_0+\coth(2n+1)u_0\Big)-2(2n+1)\Big] \qquad n\geq 1,\\
z_{n-1} &= \frac{W}{16n}\Big[\frac{\sinh(2n+1)u_0}{\sinh(2n-1)u_0}+\frac{\cosh(2n+1)u_0}{\cosh(2n-1)u_0}\Big] \qquad n\geq 1,\\
s_{n-1} &= \frac{W}{16n}\Big[\frac{\sinh(2n-1)u_0}{\sinh(2n+1)u_0}+\frac{\cosh(2n-1)u_0}{\cosh(2n+1)u_0}\Big] \qquad n\geq 1,\\
t_{n-1} &= \frac{q}{\pi\epsilon_0}\cos(2n-1)v_1\cosh(2n-1)u_1\Big[\tanh(2n-1)u_0-\coth(2n-1)u_0\Big] \qquad n\geq 1.
\end{aligned}
\tag{4.23}
$$

C. System involving the constants B_{2n}

$$
\begin{aligned}
d_0 &= +\frac{W}{4}\sinh 2u_0 + R(u_0)\Big[\frac{ik}{\lambda^2}+\frac{i}{k}\Big],\\
d_n &= +W\Big[\frac{\sinh(2n+2)u_0}{(16n+8)\sinh 2nu_0}+\frac{\cosh(2n+2)u_0}{(16n+8)\cosh 2nu_0}\\
&\quad +\frac{\sinh(2n-2)u_0}{(16n-8)\sinh 2nu_0}+\frac{\cosh(2n-2)u_0}{(16n-8)\cosh 2nu_0}\Big]\\
&\quad -\frac{2ni}{k}+\frac{i}{k}R(u_0)\coth 2nu_0+\frac{ik}{\lambda^2}\Big[R(u_0)\Big(\tanh 2nu_0+\coth 2nu_0\Big)-4n\Big] \quad n\geq 1,\\
z_0 &= -\frac{W}{8}\sinh 2u_0,\\
z_n &= -\frac{W}{16n+8}\Big[\frac{\sinh(2n+2)u_0}{\sinh 2nu_0}+\frac{\cosh(2n+2)u_0}{\cosh 2nu_0}\Big] \quad n\geq 1,\\
s_0 &= -\frac{W}{4}\frac{1}{\cosh 2u_0},\\
s_n &= -\frac{W}{16n-8}\Big[\frac{\sinh(2n-2)u_0}{\sinh 2nu_0}+\frac{\cosh(2n-2)u_0}{\cosh 2nu_0}\Big] \quad n\geq 1,\\
t_0 &= 0,\\
t_n &= \frac{q}{\pi\epsilon_0}\sin 2nv_1\sinh 2nu_1\Big[\coth 2nu_0-\tanh 2nu_0\Big] \quad n\geq 1.
\end{aligned}
\tag{4.24}
$$

D. System involving the constants B_{2n+1}

$$
\begin{aligned}
d_0 &= +\frac{W}{16}\Big[\frac{\sinh 3u_0}{\sinh u_0}+\frac{\cosh 3u_0}{\cosh u_0}\Big]-\frac{i}{k}+\frac{i}{k}R(u_0)\tanh u_0\\
&\quad +\frac{ik}{\lambda^2}\Big[R(u_0)\Big(\tanh u_0+\coth u_0\Big)-2\Big],\\
d_n &= +\frac{W}{16(n+1)}\Big[\frac{\sinh(2n+3)u_0}{\sinh(2n+1)u_0}+\frac{\cosh(2n+3)u_0}{\cosh(2n+1)nu_0}\Big]\\
&\quad +\frac{W}{16n}\Big[\frac{\sinh(2n-1)u_0}{\sinh(2n+1)nu_0}+\frac{\cosh(2n-1)u_0}{\cosh(2n+1)u_0}\Big]\\
&\quad -\frac{(2n+1)i}{k}+\frac{i}{k}\frac{R(u_0)}{\tanh(2n+1)u_0}\\
&\quad +\frac{ik}{\lambda^2}\Big[R(u_0)\Big(\tanh(2n+1)u_0+\coth(2n+1)u_0\Big)-2(2n+1)\Big] \quad n\geq 1,\\
z_{n-1} &= -\frac{W}{16n}\Big[\frac{\sinh(2n+1)u_0}{\sinh(2n-1)u_0}+\frac{\cosh(2n+1)u_0}{\cosh(2n-1)u_0}\Big] \quad n\geq 1,\\
s_{n-1} &= -\frac{W}{16n}\Big[\frac{\sinh(2n-1)u_0}{\sinh(2n+1)u_0}+\frac{\cosh(2n-1)u_0}{\cosh(2n+1)u_0}\Big] \quad n\geq 1,\\
t_{n-1} &= \frac{q}{\pi\epsilon_0}\sin(2n-1)v_1\sinh(2n-1)u_1\Big[\coth(2n-1)u_0-\tanh(2n-1)u_0\Big] \quad n\geq 1.
\end{aligned}
\tag{4.25}
$$

4.6 Short-range Wake Functions

Let us consider an ultrarelativistic trailing charge q_t travelling with a longitudinal displacement z from the leading charge q; its transverse coordinates are (u, v). The Lorentz force experienced by the trailing charge due to the leading charge is

$$\boldsymbol{F} = q_t \left(\boldsymbol{E} + \hat{z} \times c\boldsymbol{B}\right). \tag{4.26}$$

The longitudinal and transverse components of $\boldsymbol{F}$ are:

$$F_L = q_t E_z, \tag{4.27a}$$

$$\boldsymbol{F_T} = q_t \left[\hat{u}\left(E_u - cB_v\right) + \hat{v}\left(E_v + cB_u\right)\right], \tag{4.27b}$$

where the fields E_z, E_u, E_v, B_u and B_v are evaluated in (u, v, z) and depend on the position $(u_1, v_1, 0)$ of the leading charge q. Using the Eqs. (4.4e) and (4.4f); we can write:

$$\tilde{E}_v + c\tilde{B}_u = -\frac{i}{hk}\frac{\partial \tilde{E}_z}{\partial v}, \tag{4.28a}$$

$$\tilde{E}_u - c\tilde{B}_v = +\frac{i}{hk}\frac{\partial c\tilde{B}_z}{\partial v}. \tag{4.28b}$$

Thus, the force depends only on the longitudinal components E_z and B_z.
The wake function per unit of length is defined by $\boldsymbol{W} = \boldsymbol{F}/qq_t$, and is related to the impedance through the following Fourier transformation:

$$\boldsymbol{Z}(u, v, k) = \frac{1}{c}\int_{-\infty}^{+\infty} \boldsymbol{W}(z, u, v) e^{-ikz} dz. \tag{4.29}$$

Consequently, the longitudinal impedance per unit of length is given by $1/qc$ times the expression of $\tilde{E}_z(k)$ in Eq. (4.5a):

$$\begin{aligned} Z_L(u, v, k) = &\sum_{n=0}^{+\infty} \frac{A_n}{qc} \cosh nu \cos nv + \\ &+ \sum_{n=1}^{+\infty} \frac{B_n}{qc} \sinh nu \sin nv \end{aligned} \tag{4.30}$$

while the two components Z_u and Z_v of the transverse impedance $\boldsymbol{Z}_T = Z_u\hat{u} + Z_v\hat{v}$ are calculated using Eqs. (4.27b) and (4.28):

$$\begin{aligned} Z_u(u, v, k) = -\frac{i}{qchk} \sum_{n=1}^{+\infty} n\Big(&A_n \sinh nu \cos nv + \\ &+ B_n \cosh nu \sin nv\Big), \end{aligned} \tag{4.31a}$$

$$\begin{aligned} Z_v(u, v, k) = +\frac{i}{qchk} \sum_{n=1}^{+\infty} n\Big(&A_n \cosh nu \sin nv + \\ &- B_n \sinh nu \cos nv\Big). \end{aligned} \tag{4.31b}$$

Thus, the wake functions are obtained by a numerical inverse Fourier transformation of the impedance. The fields vanish for $z > 0$ and since the real part of the impedance drops more quickly for large values of k than the imaginary part it seems to be more convenient to use the cosine inverse transformation:

$$W_L = \frac{2c}{\pi} \int_0^{+\infty} \Re(Z_L) \cos(kz)\, dk \tag{4.32}$$

$$\boldsymbol{W}_T = \frac{2c}{\pi} \int_0^{+\infty} \Big[\Re(Z_v)\hat{v} + \Re(Z_u)\hat{u} \Big] \cos(kz)\, dk \tag{4.33}$$

4.7 Examples and results

In this section the impedances and the short wake functions are calculated for several cases, such as cross sections with different aspect ratio values a/b and two different kinds of conductors, aluminium and copper with DC and AC conductivity values. The conductivity σ and the relaxation time τ used for aluminium and copper are listed in Table 4.1. The relative displacement between the leading and the trailing charge is also considered. Basically, the tri-diagonal linear system in Eq. (4.18) must be truncated and when we consider large values for the aspect ratio a/b, more sine and cosine components are needed to represent the fields accurately. A particular

Table 4.1: Conductivity and electron relaxation time for aluminium and copper.

	σ	τ
Aluminium	4.2281×10^7 Sm^{-1}	8.0055×10^{-15} s
Copper	6.4534×10^7 Sm^{-1}	2.7019×10^{-14} s

case is when both charges, leading and trailing, travel along on-axis in the vacuum chamber. In this case, only the A even subsystem is excited, and the longitudinal impedance is then simplified as:

$$Z_L(u, v, k) = \sum_{n=0}^{+\infty} \frac{(-1)^n}{qc} A_{2n}. \tag{4.34}$$

In a small region around the axis the longitudinal wake function remains approximately constant while the transverse wake function depends linearly on the displacements of the leading and the trailing charges. This effect is shown in figure 4.3. The longitudinal wake function has been calculated at $z = 0$ with different transverse positions of both the leading and the trailing charges from the axis (offset). Figures 4.3(a) and 4.3(b) show these values normalized to the value of the wake function on axis. For the transverse wake function, the maximum values divided by the offset of the charges have been calculated, and figures 4.3(c) and 4.3(d) show these values normalized with respect to the limit of the wake function for the offset approaching zero. In this way it is shown that, if the offset is sufficiently small, the longitudinal wake function is approximately equal to the value on-axis, while the transverse wake function can be considered as a linear function of the offset. For this reason, whenever the offset is small, transverse wake functions are expressed per unit of length of transverse displacement in V/pC/m^2.
In the following examples we applied our method using vacuum chambers having the short half

axis length $b = 3$ mm. The reason is that this value is equal to the half gap for the undulator vacuum chamber of the FERMI@Elettra FEL project [15]. Nevertheless to better compare our plots with the results obtained with the boundary element method by Yokoya, figure 4.6 has been obtained using $b = 1$ cm, the DC conductivity model, and the same aspect ratio values presented in [9].
Figure 4.4 shows the longitudinal impedance with the AC conductivity model for copper and aluminum, as a function of the wave number k and for several values of the aspect ratio a/b.
Figure 4.5 shows the longitudinal wake functions for a vacuum chamber with semi-minor axis $b = 3$ mm and several aspect ratio values a/b, as a function of the longitudinal displacements behind the leading charge. It is worthwhile noting that the longitudinal wake functions reduce to those of the circular case when $a/b = 1$ [7] and to those of the parallel plates when $a/b >> 1$ [8], respectively.
Figure 4.6 shows the transverse wake functions obtained using DC conductivity model for copper and a semi-axis $b = 10$ mm. It is worthy to mention that in the figure the conductivity used is 5.3×10^7 Sm^{-1} and that the results obtained reduce correctly to the circular case [4] and to the parallel plates case [5]. Furthermore, the results are in good agreement with the solutions proposed in [9].
Figure 4.7 shows the transverse wake functions as functions of the longitudinal displacement behind the leading charge, for aluminum. Here we considered three different relative transverse positions between the leading and the trailing charges: both charges with a y-offset, the leading charge off-axis and the trailing charge on-axis and vice versa. The semi-minor axis b is 3 mm and the more significant case of AC conductivity model is considered. Figure 4.7(f) shows that $\frac{\partial}{\partial x}W_x + \frac{\partial}{\partial x_1}W_x$ vanishes for large values of a/b, when the ellipse approches the parallel plates limit. When an ultra short bunch is considered, then the transverse wake with the leading and the trailing charges off-axis with the same offset should be considered. Figures 4.7(e) and 4.7(f) represent this case. As explained in [16], the transverse wake forces near the axis of a bi-symmetric pipe (the elliptical pipe has mirror simmetry in both x and y) have the property $\frac{\partial W_y}{\partial y} = -\frac{\partial W_x}{\partial x}$. This explains why Fig. 4.7(d) is the mirror of Fig. 4.7(c).
Once the wake function is known, the energy change per unit length (in eV/m) induced within a particle bunch is obtained from the convolution:

$$\Delta E(z) = -eQ \int_{-\infty}^{z} W_L(z - z')\rho(z')dz'. \tag{4.35}$$

where e is the electron charge and Q is the total bunch charge with longitudinal charge distribution $\rho(z)$ expressed in m^{-1}. Figure 4.8 shows the convolutions obtained with the wake functions and flat top bunches of charge equal to 1 nC and different lengths.
Like for the longitudinal case, once the transverse wake function is known, the transverse kick for unit length and for transverse offset (in $\mathrm{rad/m}^2$) received by the particles in the vertical plane within the bunch is obtained from the following convolution:

$$k_y(z) = \frac{eQ}{E_0} \int_{-\infty}^{z} W_y(z - z')\rho(z')dz', \tag{4.36}$$

where e is the electron charge, Q is the total bunch charge with longitudinal bunch distribution $\rho(z)$ and E_0 is the bunch mean energy. Here only the vertical plane is considered, because for

aspect ratio values $a/b > 3$ the effect of the transverse wake for a horizontal offset can be neglected. Figure 4.9 shows the convolutions obtained with the wake functions and flat top bunches of charge equal to 1 nC and different lengths.

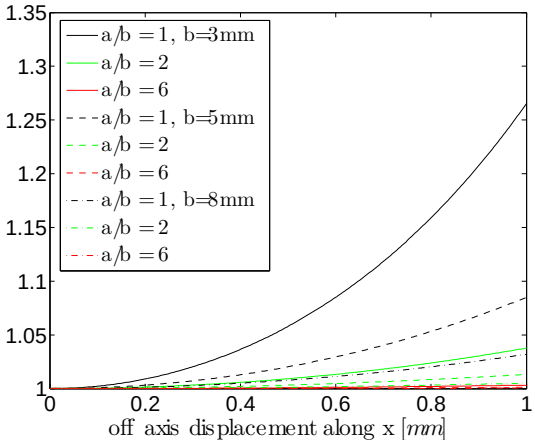

(a) $W_z(x, x_1, z = 0)/W_z(x = 0, x_1 = 0, z = 0)$ vs $x = x_1$.

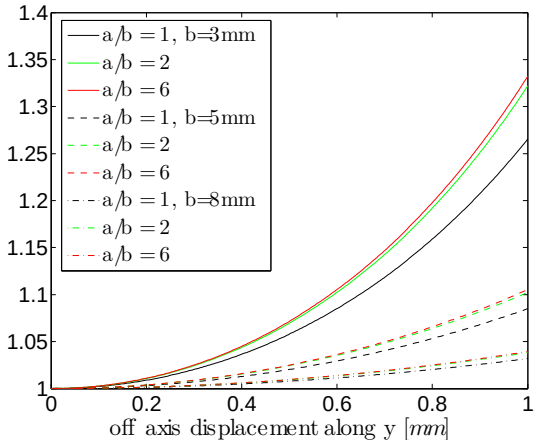

(b) $W_z(y, y_1, z = 0)/W_z(y = 0, y_1 = 0, z = 0)$ vs $x = x_1$.

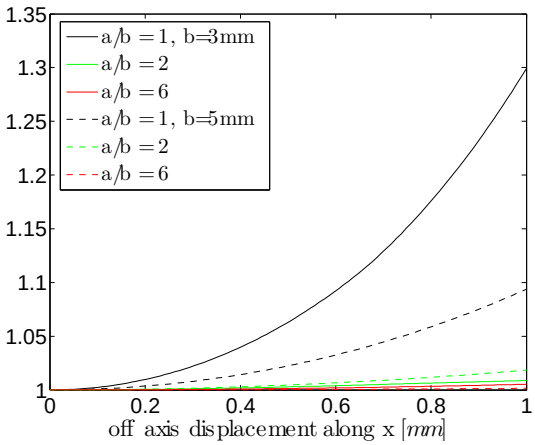

(c) $\max_z |W_x(x, x_1)/x| / \max_z |W_x(x = \epsilon, x_1 = \epsilon)/\epsilon|$ vs $x = x_1$, $\epsilon << 1\mu$m.

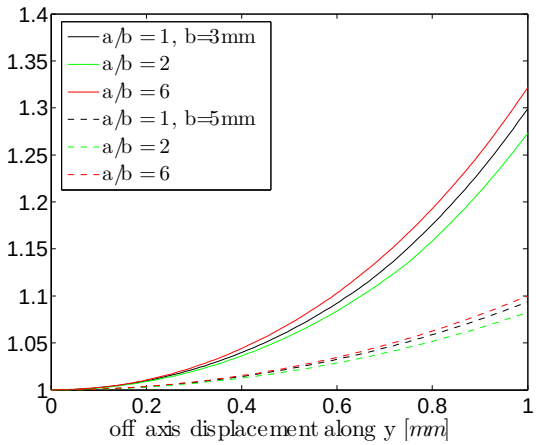

(d) $\max_z |W_y(y, y_1)/y| / \max_z |W_y(y = \epsilon, y_1 = \epsilon)/\epsilon|$ vs $y = y_1$, $\epsilon << 1\mu$m.

Figure 4.3: Growth of the longitudinal wake functions and non linearity with the offset of the tranverse wake functions depending on the offset of the leading and trailing charges

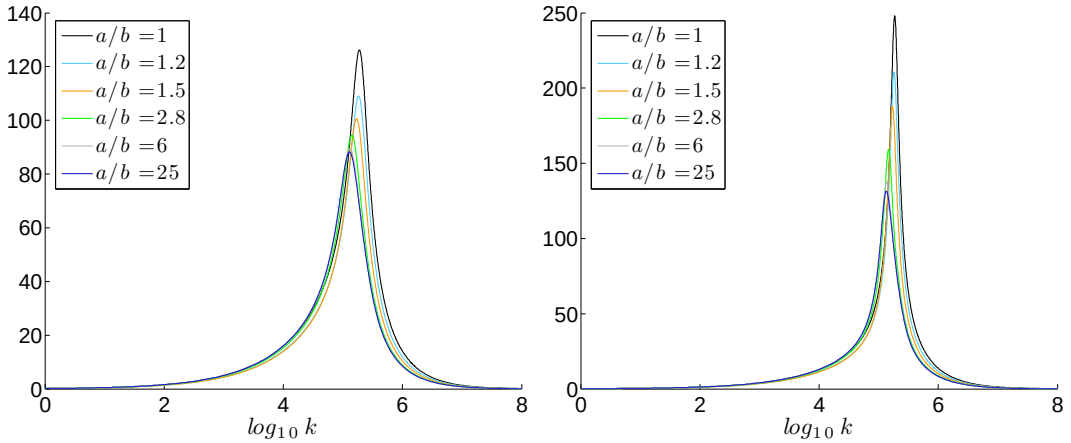

(a) $|Z_L|$, Ω/m, aluminum, semi-minor axis $b = 3$ mm. (b) $|Z_L|$, Ω/m, copper, semi-minor axis $b = 3$ mm.

Figure 4.4: Longitudinal impedance vs $log_{10}k$ (k in m^{-1}) obtained using the AC conductivity model for aluminium (a) and copper (b), semi-axis $b = 3$mm and with several aspect ratio values a/b.

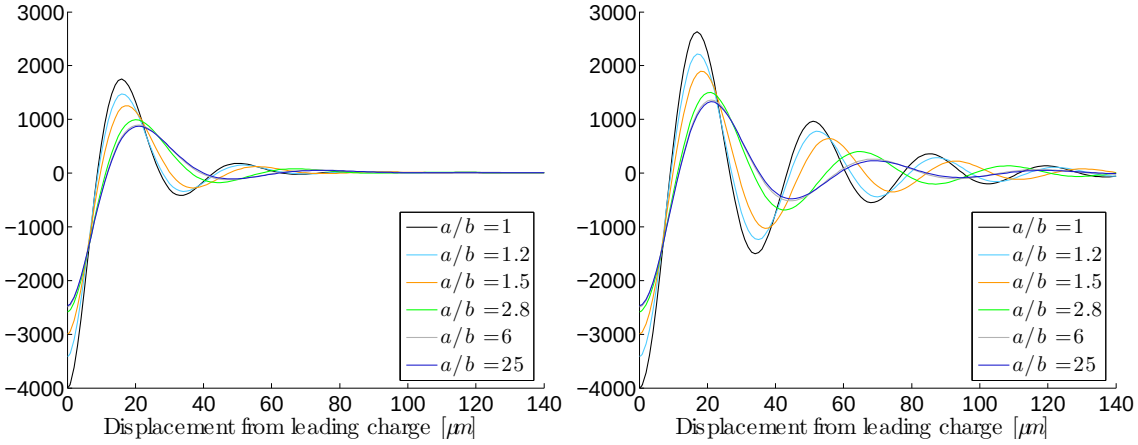

(a) W_L, V/pC/m, Al, with AC conductivity model. (b) W_L, V/pC/m, Cu, with AC conductivity model.

Figure 4.5: Dependence of longitudinal wake functions on the longitudinal displacement behind the leading charge. Semi-minor axis $b = 3$ mm, AC conductivity models for aluminum (a) and copper (b) and several aspect ratio values a/b.

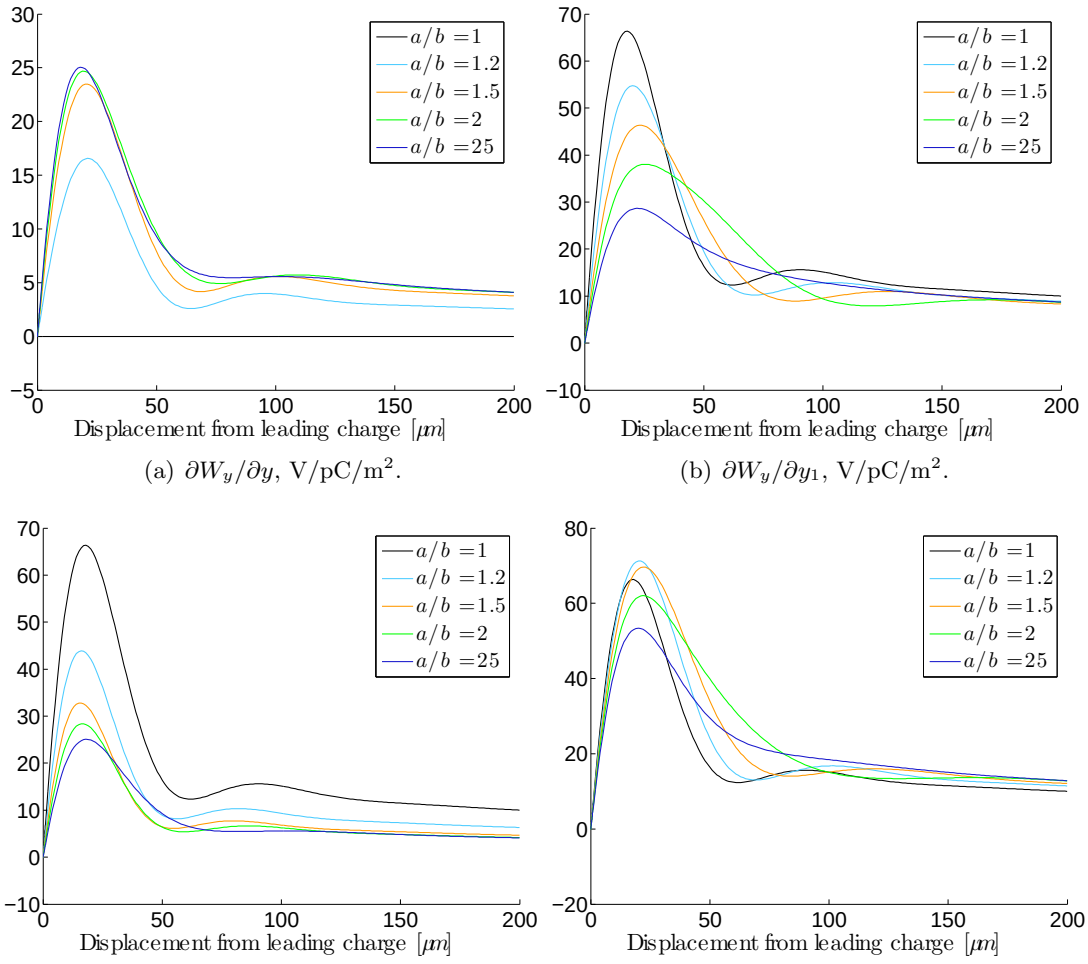

(a) $\partial W_y/\partial y$, V/pC/m^2.

(b) $\partial W_y/\partial y_1$, V/pC/m^2.

(c) $\partial W_x/\partial x$, V/pC/m^2.

(d) $\partial W_y/\partial y + \partial W_y/\partial y_1$, V/pC/m^2, due to the leading and trailing charghe with the same y-offset.

Figure 4.6: Transverse wake functions in the case where both charges are close to the vacuum chamber axis. The vacuum chamber has short half-axis of length $b = 1$ cm, the metal wall is characterized by a conductivity $\sigma = 5.3 \times 10^7$ Sm^{-1}, and the DC conductivity model has been used.

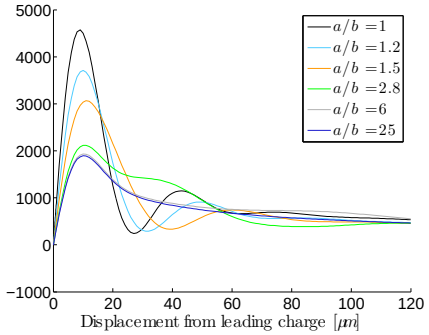

(a) $\partial W_y/\partial y_1$, V/pC/m^2, the leading charge off axis and the trailing charge on-axis.

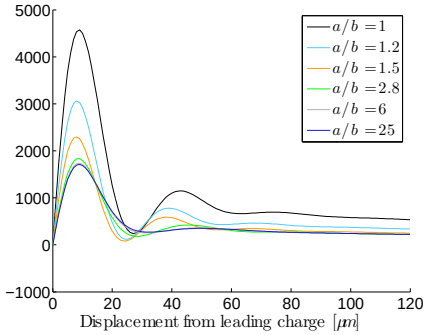

(b) $\partial W_x/\partial x_1$, V/pC/m^2, the leading charge off axis and the trailing charge on-axis.

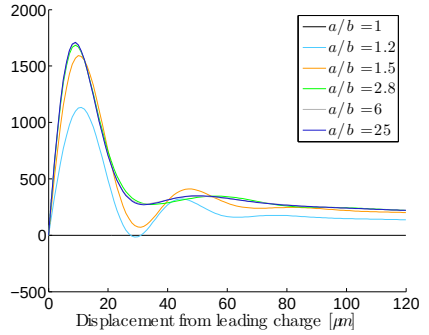

(c) $\partial W_y/\partial y$,V/pC/m^2, the trailing charge off axis and the leading charge on-axis.

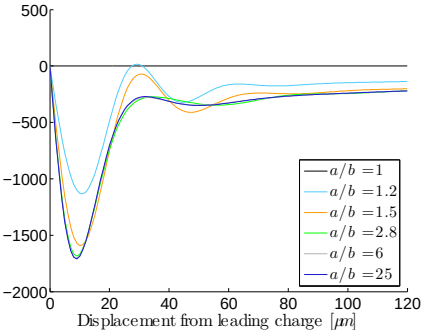

(d) $\partial W_x/\partial x$, V/pC/m^2,the trailing charge off axis and the leading charge on-axis.

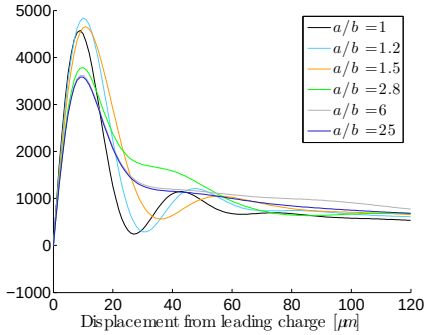

(e) $\partial W_y/\partial y_1 + \partial W_y/\partial y$, V/pC/m^2, the leading and the trailing charges off-axis.

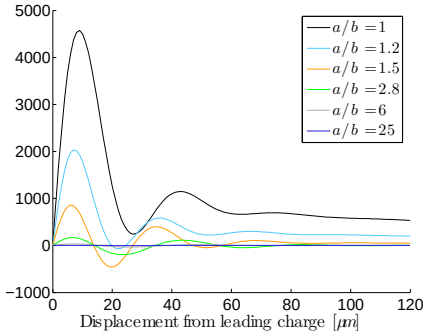

(f) $\partial W_x/\partial x_1 + \partial W_x/\partial x$, V/pC/m^2, the leading and the trailing charges off-axis.

Figure 4.7: Dependence of tranverse wake functions on the longitudinal displacement behind the leading charge in a small region around the vacuum chamber axis. Semi-minor axis $b = 3$ mm and several values of the aspect ratio a/b are considered. AC conductivity model for aluminium is used.

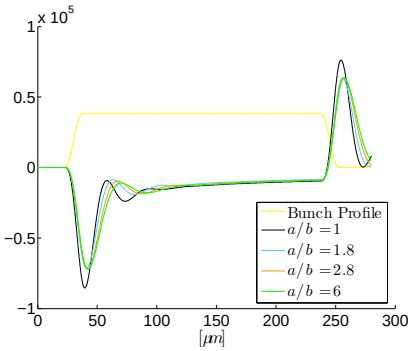

(a) ΔE, eV/m, flat length 200μm, rise length 15μm, aluminum.

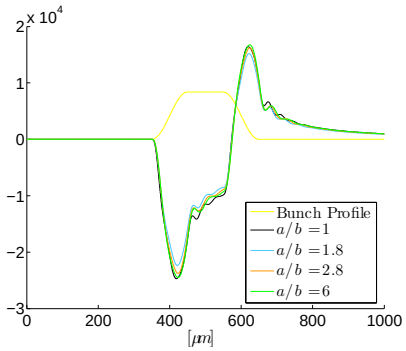

(b) ΔE, eV/m, flat length 200μm, rise length 15μm, copper.

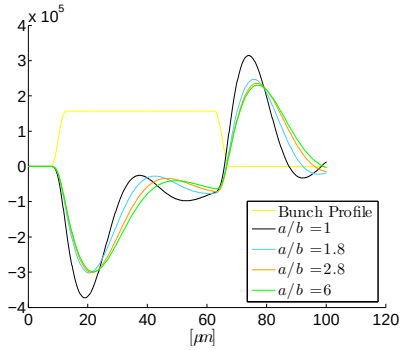

(c) ΔE, eV/m, flat length 50μm, rise length 5μm, aluminum.

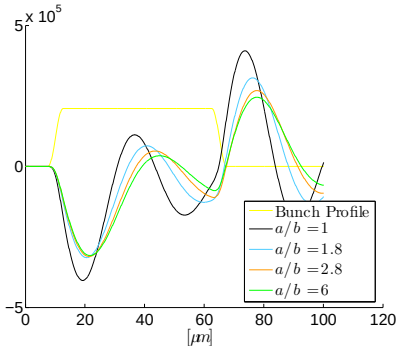

(d) ΔE, eV/m, flat length 50μm, rise length 5μm, copper.

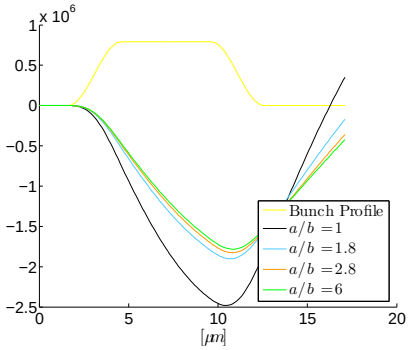

(e) ΔE, eV/m, flat length 5μm, rise length 3μm, aluminum.

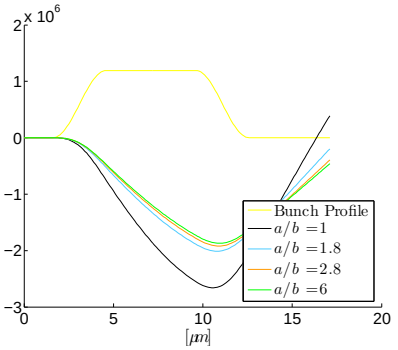

(f) ΔE, eV/m, flat length 5μm, rise length 3μm, copper.

Figure 4.8: Energy variation per unit length induced within flat top bunches with different lengths and charge of 1 nC. Semi-minor axis $b = 3$ mm, AC conductivity model and several aspect ratio values a/b are used.

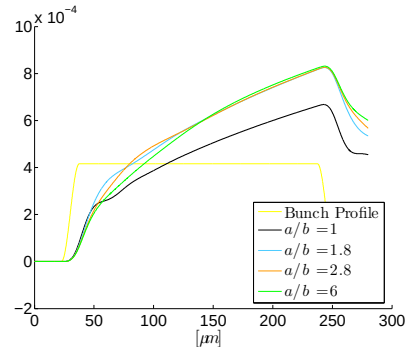

(a) k_y, rad/m^2, flat length 200μm, rise length 15μm, aluminum.

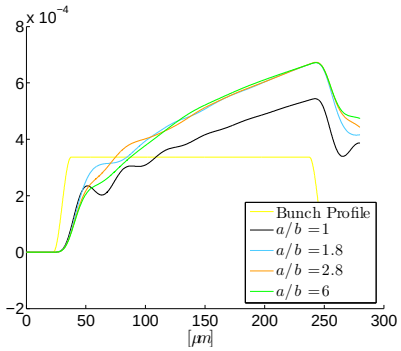

(b) k_y,rad/m^2, flat length 200μm, rise length 15μm, copper.

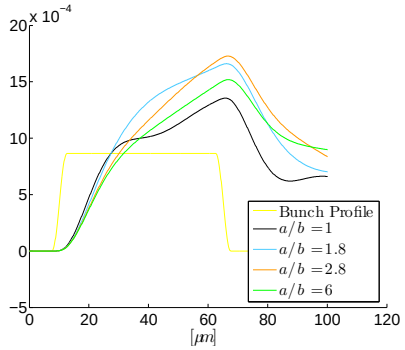

(c) k_y, rad/m^2, flat length 50μm, rise length 5μm, aluminum.

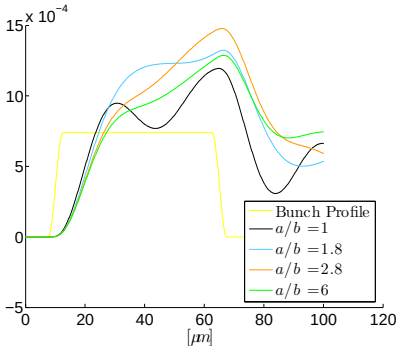

(d) k_y, rad/m^2, flat length 50μm, rise length 5μm, copper.

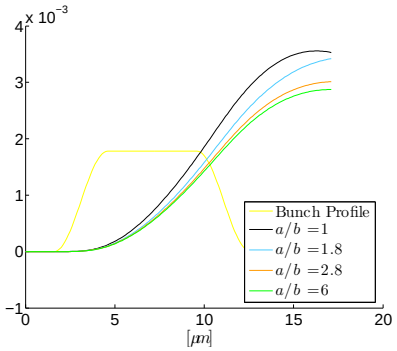

(e) k_y, rad/m^2, flat length 5μm, rise length 3μm, aluminum.

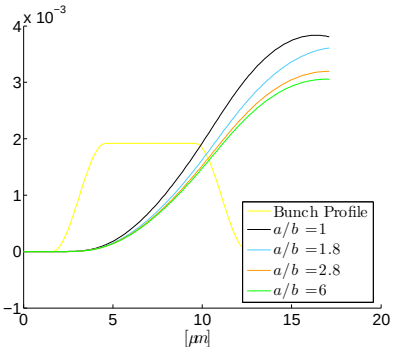

(f) k_y, rad/m^2, flat length 5μm, rise length 3μm, copper.

Figure 4.9: Transversal kick per unit length and off-axis displacement, along the short axis direction, induced within flat top bunches with different lengths and charge 1 nC at 1.2 GeV. Semi-minor axis $b = 3$ mm, AC conductivity model and several aspect ratio values a/b are used.

4.8 Wakefield effects in the FERMI FEL 1 Undulator Vacuum chamber

An electron beam will pass through an array of 9 separate undulator segments to produce FEL x-ray radiation. The total length of the undulator will be 32.8 m long, which includes one 3.2-m-long modulator segment, one 1.2-m-long drift tube with a dispersive section, eight 2.5-m-long radiator segments, and 1.2-m-long breaks in between.
There are two sources of wakefields within the undulator vacuum chamber: the resistive walls (RW) and the rough surface wakes. The effect of the undulator wakefields becomes considerable when the variation in energy becomes big compared to the FEL parameter ρ which is $2.6 \cdot 10^{-3}$ for FEL 1 and $2.1 \cdot 10^{-3}$ for FEL-1^+, respectively. In fact, we can write the condition considering the total rms relative energy spread:

$$(\sigma_\delta)_{tot} = \sqrt{\sigma_\delta^2 + (\sigma_\delta)_{seed}^2 + \sigma_{\delta W}^2} < \rho \tag{4.37}$$

where σ_δ is the electron beam slice energy spread, δ_{seed} is the energy modulation introduced by the seed laser in the modulator and $\sigma_{\delta W}$ is the energy variation due to the wake effects. We can write $\delta_{seed} = n\sigma_\delta$ where n is the harmonic that is 6 for FEL-1 ($40nm$) and 12 for FEL-1^+ ($20nm$), respectively. The condition that the total wake effect at $1.2GeV$ should respect is $\Delta W_{rms} < 129keV/m$ for FEL-1 and $\Delta W_{rms} < 75keV/m$ for FEL-1^+, respectively.
Two electron beam scenarios have been proposed: the medium length bunch (MLB) mode with a bunch length of $200\mu m$ and the short length bunch (SLB) with a bunch length of $35\mu m$.

4.8.1 The Resistive Wall Wakes

The undulator vacuum chamber is designed to fit the minimum undulator gap of $10mm$; and in order to mitigate the RW wake effects, a pipe with inner surface material of aluminum and an elliptical cross-section with inner minor axis of $7mm$ and major axis of $21mm$ has been proposed. The longitudinal wake functions for an elliptical vacuum chamber for several aspect ratios a/b (a is the major semi-axis while b is the minor semi-axis of the ellipse) are shown in fig. 4.10 for $b = 3.5mm$. The figure clearly shows that the maximum amplitude of the wake function decreases if we increase the aspect ratio (between parallel plates and rounded pipe the the wake function $w(s = 0^+)$ is $\pi^2/16$ times lower). Figure 4.11 shows the mapping of the longitudinal wake function in the transversal plane at $s = 0^+$ for an elliptical pipe with $a/b = 3$ and $b = 3.5mm$. The electromagnetic field is strongly attenuated close to the lateral side of the ellipse at $x \approx 10mm$ and $y = 0$. Table 4.2 reports the values of the wake functions at the origin ($s = 0^+$) and at the lateral side ($x = a$). The amplitude of the wake results attenuated at least by 10% for aspect ratio $a/b \geq 2.8$.

Induced energy variation for the MLB case

The effect of the longitudinal resistive wall wakefield is to induce an energy variation which is correlated with the longitudinal position inside the bunch. The bunch profile for the medium bunch case [15] with a total charge $Q = 0.8nC$ is shown in figure 4.12 (the head of the bunch is to the left). The induced energy variation is defined as the convolution of the wake function with the electron bunch linear current density distribution. The results for several aspect ratios

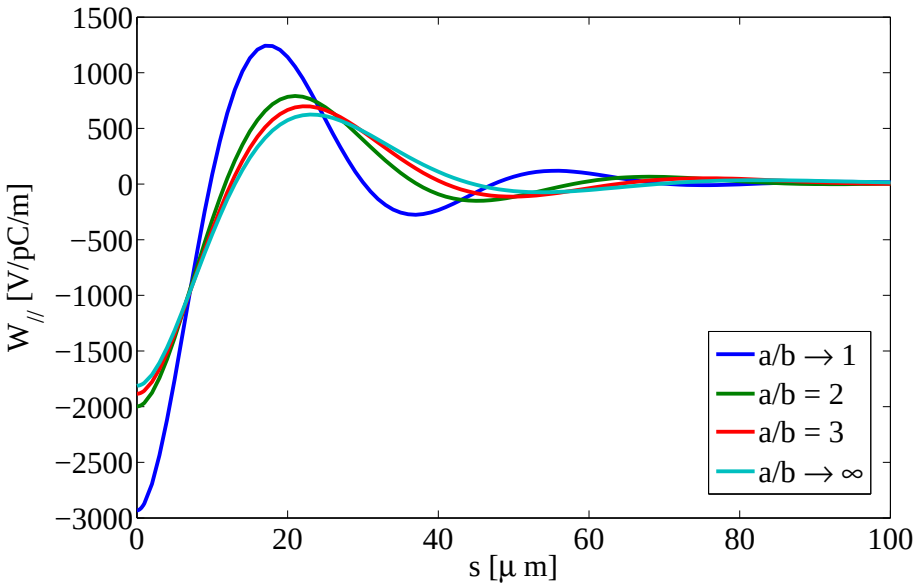

Figure 4.10: Dependence of longitudinal wake functions on the longitudinal displacement behind the leading charge. Semi-minor axis $b = 3.5mm$, AC conductivity models for aluminum and several aspect ratio values a/b.

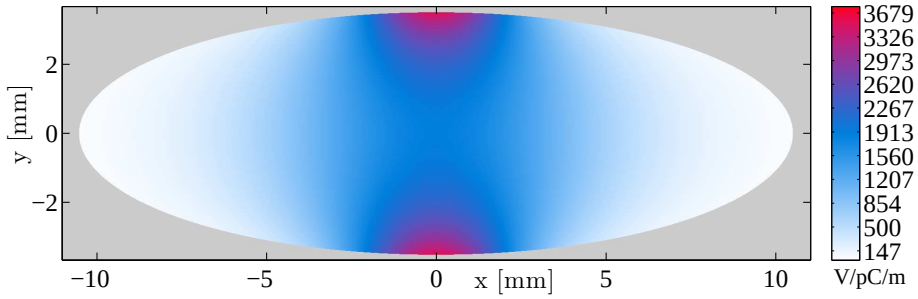

Figure 4.11: Mapping of longitudinal wake functions in the transversal section at $s = 0^+$ for an elliptical vacuum chamber with $a/b = 3$ and $b = 3.5mm$.

with $b = 3.5mm$ are shown in fig. 4.13. The sign convention is that positive values indicate energy gain for a particle located at a distance s behind the leading point charge. It is worthwhile noting that, apart from rather large amplitude oscillations at the head and the tail of the bunch the absolute energy variation is constant at the bunch core ($\approx 4keV/m$) for all aspect ratios considered. Table 4.3 shows the average energy lost by the bunch and the rms energy spread for several aspect ratios. It is to be noted that for the medium bunch used for the $FEL1$ the energy variation due to the RW wakes is negligible for all aspect ratios compared to $129keV/m$.

Table 4.2: Values of the longitudinal wake functions at the origin and close to the boundary for several aspect ratiosdifferent a/b.

a/b	$W_{//}$ $x=0$	$W_{//}$ $x=a$	ratio	$W_{//}$ $x=a-1mm$	ratio	$W_{//}$ $x=a-2mm$	ratio
	$[V/pC/m]$	$[V/pC/m]$	[%]	$[V/pC/m]$	[%]	$[V/pC/m]$	[%]
1.001	-2931.8	-2927.4	99.8	-2929.5	99.9	-2931.0	100
2.0	-1997.8	-310.2	15.5	-503.6	25.0	-754.3	37.8
2.8	-1896.0	-53.7	2.8	-107.7	5.6	-191.6	10.1
3.0	-1883.9	-34.5	1.8	-72.5	3.8	-132.9	7.1
3.2	-1874.2	-22.1	1.2	-48.5	2.6	-91.6	4.9
4.0	-1850.0	-3.7	0.2	-9.5	0.5	-19.8	1.1
20.0	-1811.8	0.0	0.0	0.0	0.0	0.0	0.0

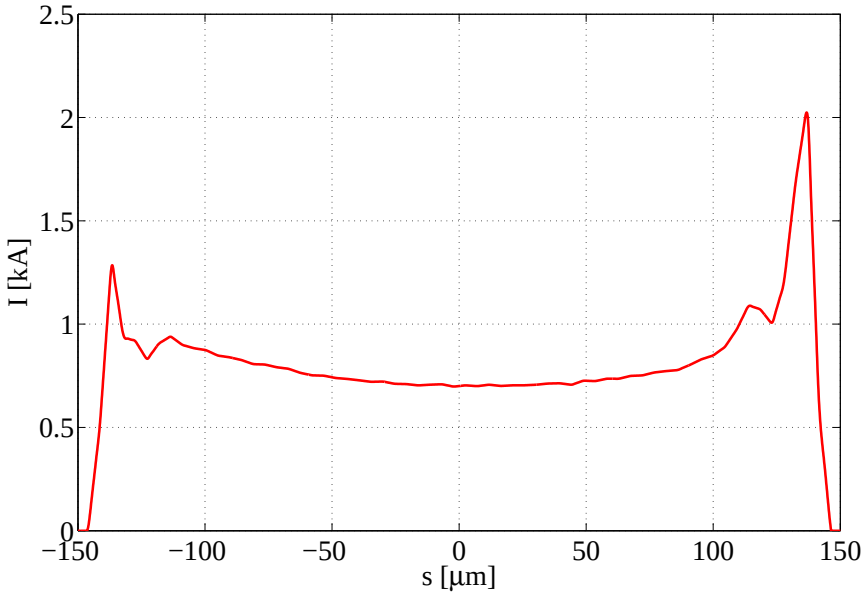

Figure 4.12: Nominal current distribution for the MLB case. Total charge 0.8nC.

Induced energy variation for the SLB case

The induced energy variation for several aspect ratios and with $b = 3.5mm$ are shown in fig. 4.14. It is worthwhile noting that the energy variations are much larger than in the previous case. In particular, the energy change in the head of the bunch results in an unacceptable value for the $FEL1^+$ for all aspect ratios ($< 75keV/m$) while, for $FEL1$ ($< 129keV/m$), when using an elliptical cross section with $a/b > 2$, the energy variation meets the specifications. The bunch profile for the SLB case used for $FEL1^+$ with a total charge $Q = 0.33nC$ is shown in figure 4.15 (the head of the bunch is to the left). Table 4.4 shows the average energy lost by the bunch and the rms energy spread per unit of length for several aspect ratios. For the FEL, the variation of the induced energy change is important since an average change can always be compensated by

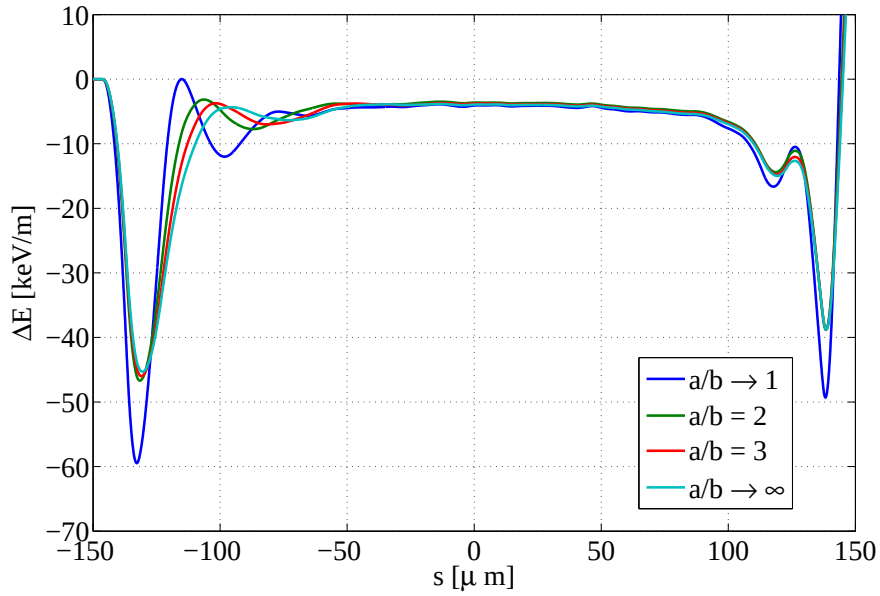

Figure 4.13: Energy change per unit of length within the medium length bunch for several aspect ratio a/b.

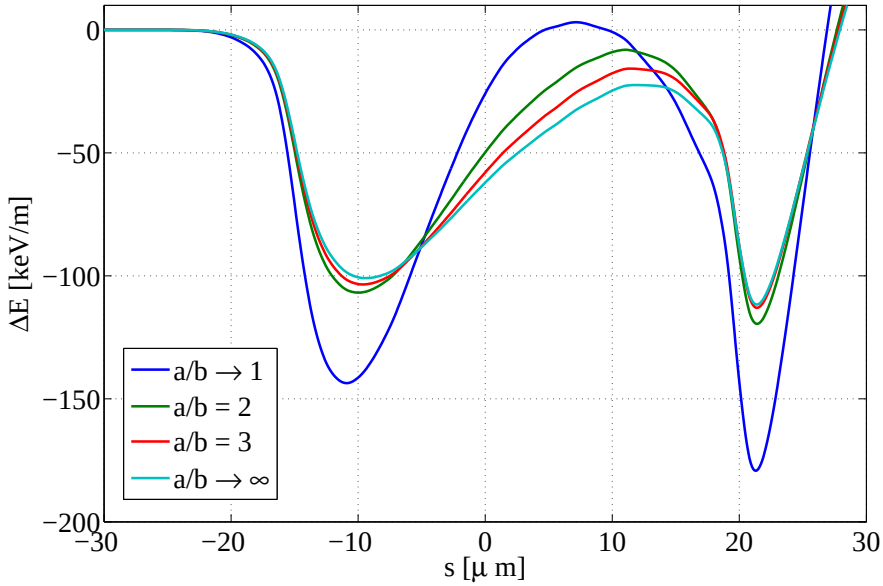

Figure 4.14: Energy change per unit of length within the short bunch for several aspect ratio a/b and with minor-semi axis $b = 3.5mm$.

tapering the undulator strength. We see, from table 4.4, that the rms energy spreads could be reduced at reasonable values after the tapering. The effect can be further reduced with respect

Table 4.3: Average energy lost by the bunch and energy spread per unit of length for MLB case.

a/b	$\langle \Delta E \rangle$	ΔE_{rms}
	$[keV/m]$	$[keV/m]$
1.001	-11.29	13.10
2.0	-9.93	10.65
2.8	-10.26	10.70
3.0	-10.31	10.70
3.2	-10.35	10.71
4.0	-10.44	10.71
20.0	-10.60	10.71

to a round pipe of approximately 40% if we use an elliptical vacuum chamber.

Table 4.4: Average energy lost by the bunch and energy spread per unit of length. SLB case with the total charge of $0.33nC$.

a/b	$\langle \Delta E \rangle$	ΔE_{rms}
	$[keV/m]$	$[keV/m]$
1.001	-70.66	56.71
2.0	-55.59	35.97
3.0	-57.03	32.17
20.0	-58.98	29.70

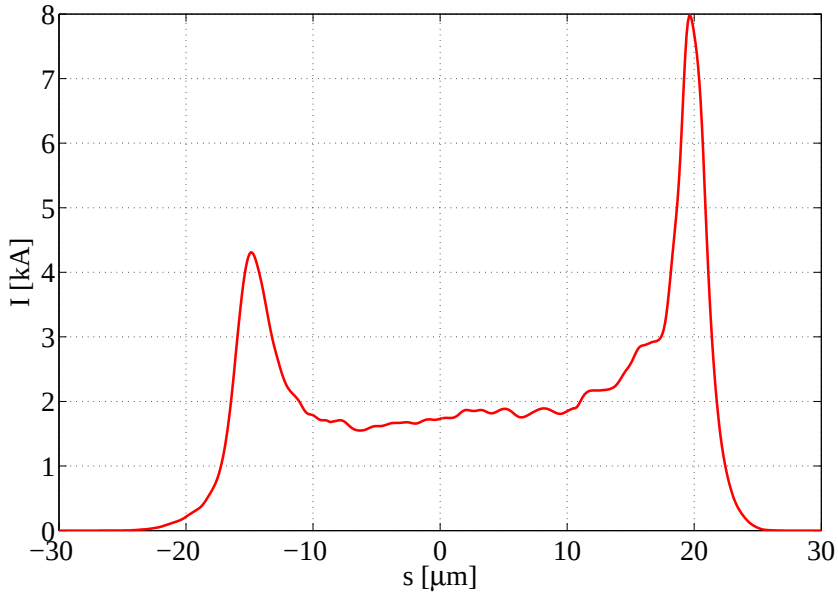

Figure 4.15: Nominal current distribution for the short bunch case used for ($FEL1^{+}$). Total charge 0.33nC.

4.8.2 The Surface Roughness Wakefields

This section addresses the effects of the wakefields that are excited by the interaction of the bunch charge with the roughness of the vacuum chamber surface. The model for the study considers a perfectly round conducting pipe wall with radius b, having a sinusoidal corrugation with longitudinal periodicity λ_s and rms amplitude h_{rms}. Details can be found in ref. [17, 18]. The results presented here were obtained in the small angle approximation, assuming a rms amplitude h_{rms} which is much smaller than the period λ_s or, in terms of aspect ratio, $AR = \lambda_s/h_{rms} >> 1$.

Induced energy variation for the MLB case

The induced energy variations within the medium bunch profile for several aspect ratios and with $b = 3.5mm$ are shown in fig. 4.16. It is worthwhile noting that for the medium bunch case the energy variations in the core of the bunch can be neglected if the $AR \geq 80$ (less than 10% of the specification). If the $AR > 40$ then the energy variation in the bunch core is less than 30% of the specification. Table 4.5 shows the average energy lost by the bunch core and the rms energy spread per unit of length for several aspect ratios AR. It is to be noted that tha amplitude of the energy variation closely depends on $1/AR^2$ and $1/b$.

Table 4.5: Average energy and energy spread per unit of length due to the roughness wall wakefields within the bunch core for the medium bunch case. The longitudinal periodicity is $\lambda_s = 20\mu m$.

AR	$\langle \Delta E \rangle$	ΔE_{rms}
	$[keV/m]$	$[keV/m]$
200	0.0	0.6
80	0.0	3.9
40	0.3	16.5
25	46.8	23.4

Induced energy variation for the SLB case

The induced energy variations within the short bunch profile for several aspect ratios and with $b = 3.5mm$ are shown in fig. 4.17. Table 4.6 shows the average energy lost by the bunch and the rms energy spread for several aspect ratios AR. It is worthwhile noting that for the short bunch case the energy variations due to surface roughness wakes can still be acceptable if the $AR \geq 80$, apart from rather large oscillations at the head and the tail of the bunch. With an aspect ratio AR 200 the energy variation can be completely neglected.

4.8.3 Induced energy variation for the SLB case with $b = 5mm$

The induced energy variations due to the RW wakes within the short bunch profile for several aspect ratios and with $b = 5mm$ are shown in fig. 4.18. The comparison with the previous results obtained with $b = 3.5mm$ shows that in this case we can reduce the first peak of the energy variation of approximately 40% and to meet the specification without tapering the undulator strength. The induced energy variations due to surface roughness wakes within the short bunch profile for several aspect ratios and with $b = 5mm$ are shown in fig. 4.19. The conclusions are

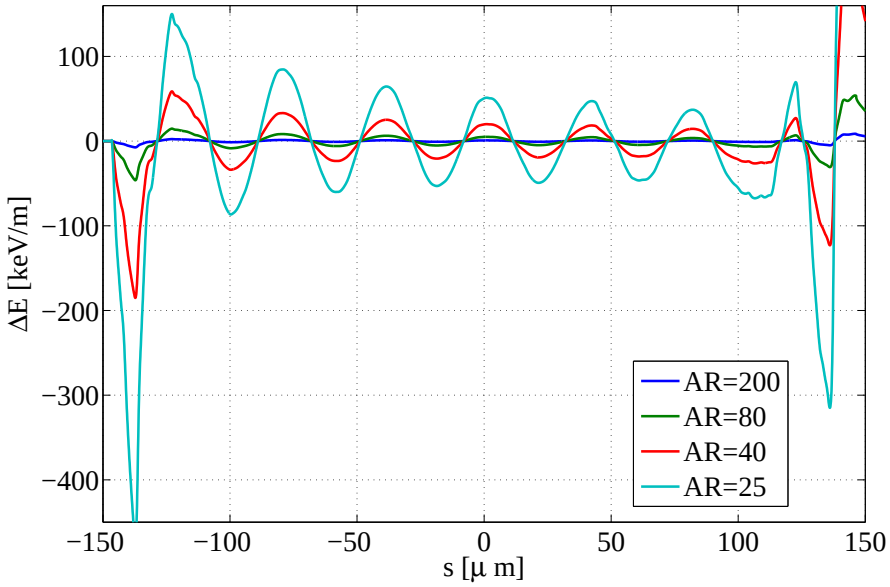

Figure 4.16: Energy variation for the medium bunch in a circular cross-section vacuum chamber with radius 3.5mm with several aspect ratio $AR = \lambda_s/h_{rms}$. The longitudinal periodicity is $\lambda_s = 20\mu m$.

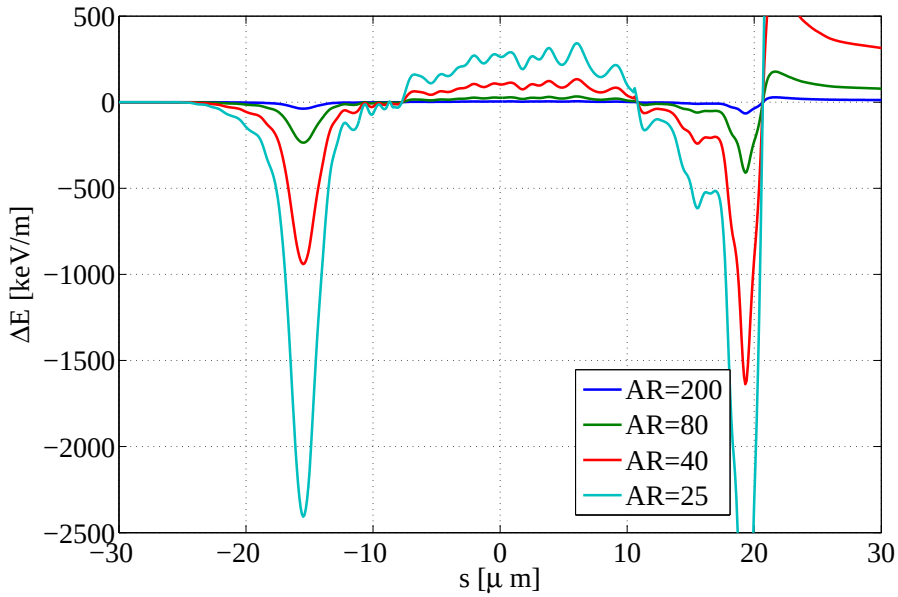

Figure 4.17: Energy variation for the short bunch in a circular cross-section vacuum chamber with radius 3.5mm with several aspect ratio $AR = \lambda_s/h_{rms}$. The longitudinal periodicity is $\lambda_s = 20\mu m$.

that the requirements on the sinusoidal corrugations remains in the same order of magnitude as in the previous case ($b = 3.5mm$). For the medium length bunch (MLB) case using a round pipe

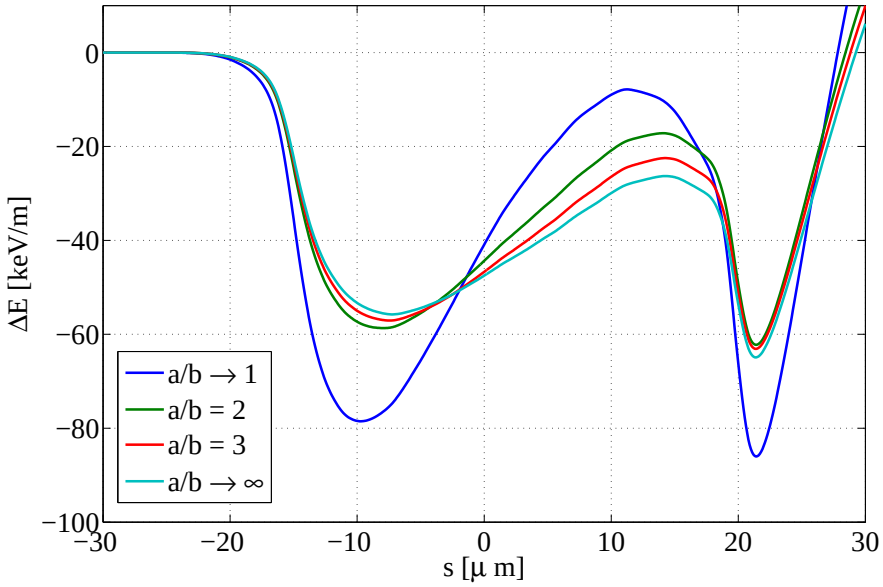

Figure 4.18: Energy change per unit of length due to RW wakes within the short bunch for several aspect ratio of the elliptical cross section and with $b = 5mm$.

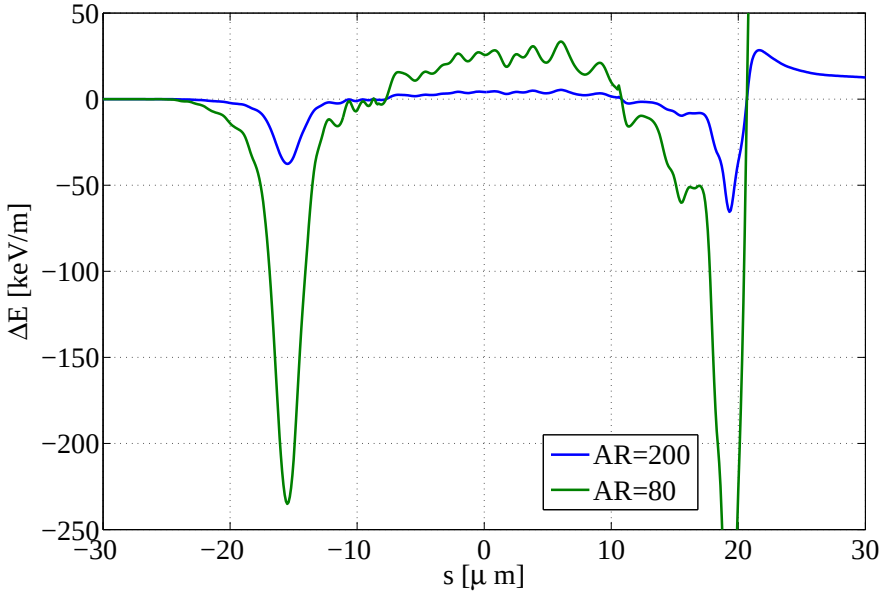

Figure 4.19: Energy change per unit of length due to rough surface wakes for the short bunch in a circular cross-section vacuum chamber with $b = 5mm$ with several aspect ratio $AR = \lambda_s/h_{rms}$. The longitudinal periodicity is $\lambda_s = 20\mu m$.

with surface roughness aspect ratio $AR \geq 80$ the energy variation due to the RW and surface roughness wakes is less than 10% of the specification ($< 129keV/m$). For the short length bunch (SLB) case using an elliptical cross section with aspect ratio $a/b > 2$ the energy variation due to the RW wakes in the head of the bunch results in an unacceptably value for $FEL1^+$ and thus a tapering of the undulator stregth is required. On the other hand the specification for $FEL1$ are met without tapering. For the SLB case the energy variation due to the surface roughness wakes can be acceptable with $AR > 80$ apart from rather large oscillations at the head and the tail of the bunch. With an aspect ratio AR 200 the energy variation can be completely neglected.
For the SLB case if the minor axis b is increased from $3.5mm$ to $5mm$ then the first peak of the energy variation due to RW wakes is reduced by 40% while the requirements on the sinusoidal corrugations remains in the same order of magnitude.

Table 4.6: Average energy and energy spread per unit of length due to the roughness wakefields for the SLB case.

AR	$\langle \Delta E \rangle$	ΔE_{rms}
	$[keV/m]$	$[keV/m]$
200	0.0	7.8
80	-0.2	59.9
40	-12.6	345.2
25	-42.0	521.4

4.9 Conclusion

In this paper we have analytically derived expressions for the high-frequency longitudinal and transverse resistive-wall coupling impedance of an elliptical cross-section vacuum chamber. Then, the corresponding longitudinal and transversal wake functions have been obtained by calculating numerically the inverse Fourier transformations of the impedances. Once the longitudinal wake function was known the energy changes per unit length induced within particle bunches was estimated by means of a convolution between the wake function and several flat-top charge distributions. The results show that the energy variation induced within the bunch could assume an unacceptably large value when shorter electron bunches are used. Using the aluminum as material and an elliptical shape with aspect ratio $a/b > 3$ for the vacuum chamber, the amplitude and the number of oscillations can be reduced.
As for the longitudinal case, the transverse kick for unit length and for transverse offset received by the particles in the vertical plane within the bunch, is obtained through the convolution between the transverse wake function and the flat-top charge distributions. For the particle bunches considered, the results have shown that the kick angle received from the head and tail of the bunch itself maintains an acceptable value even for shorter lengths of the charge distributions. It is worthwhile to mention that in a small region around the axis the longitudinal wake function remains approximately constant while the transverse wake function depends linearly on the displacements of the leading and trailing charges.
Estimations of the induced energy-spread caused by the resistive wall and surface roughness wakefields along the FERMI FEL 1 undulator were also presented. Regarding to the resistive wall wakes

it is to be noted that for the MLB case, apart from rather large amplitude oscillations at the head and tail of the bunch, the residual absolute energy variation at the bunch core is $-5keV/m$. On the other hand for the SLB case the residual absolute energy variation at the bunch core could result in an unacceptably value for FEL 1 at $20nm$.
Besides it was found that the residual absolute energy variation due to the surface roughness wakefields could be neglected if the aspect ratio $AR \geq 80$ for both medium and short length bunch cases.

References

[1] R. L. Gluckstern, J. V. Zeijts, and B. Zotter, "Coupling impedance of beam pipes of general cross-section," *Phys. Rev. E*, vol. 47, pp. 656–663, 1992.

[2] L. Palumbo and V. G. Vaccaro, *Il Nuovo Cimento*, 1985, vol. 89, no. 3.

[3] A. Piwinski, "Impedances in lossy elliptical vacuum chambers," DESY, Tech. Rep. DESY-94-068, 1994.

[4] A. W. Chao, *Physics of collective beam instabilities in high-energy accelerators.* New York: Wiley, 1993.

[5] H. Henke and O. Napoly, "Wake fields between two parallel resisitive plates," in *Proc. of 2nd Europ. Part. Accel. Conf.*, Nice, June 1990, p. 1046.

[6] N. W. Ashcroft and N. D. Mermin, *Solid State Physics.* Harcourt Inc., 1976, ch. 1.

[7] K. L. F. Bane and M. Sands, "The short-range resistive wall wakefields," *AIP Conf. Proc.*, vol. 367, pp. 131–149, 1996.

[8] K. L. F. Bane and G. Stupakov, "Resistive Wall Wakefield in the LCLS undulator," in *Proc. of the Part. Accel. Conf.*, Knoxville, Tennessee, USA, May 2005.

[9] K. Yokoya, "Resistive wall impedance of beam pipes of general cross section," *Part. Accel.*, vol. 41, pp. 221–248, 1993.

[10] A. Lutman, R. Vescovo, and P. Craievich, "Electromagnetic field and short-range wake function in a beam pipe of elliptical cross section," *Phys. Rev. ST Accel. Beams*, vol. 11, no. 7, p. 074401, July 2008.

[11] P. M. Morse and H. Feshbach, Eds., *Methods of theoretical physics.* McGraw-Hill, 1953, pp. 556–568.

[12] F. A. Alhargan, "A complete method for the computations of mathieu characteristic numbers of integer orders," *SIAM Rev.*, vol. 38, no. 2, pp. 239–255, 1996.

[13] B. Rembold and Z. Angew, *Math. Mech*, vol. 53, pp. 783–789, 1973.

[14] H. Abramowitz and I. A. Stegun, *Handbook of mathematica functions.* Dover, 1964, pp. 722–742.

[15] "FERMI@Elettra Conceptual Design Report," Sincrotrone Trieste, Tech. Rep. ST/F-TN-07/12, 2007.

[16] R. Klatt and T. Weiland, "Wake Field Calculations with Three-Dimensional BCI Code," in *Proc. of the Lin. Accel. Conf.*, Stanford, California, Jun 1986, pp. 282–285.

[17] G. V. Stupakov, "Surface roughness impedance," in *Proc. of the 18th Advanced ICFA Beam Dynamics Workshop on the Physics of and the Science with X-Ray Free Electron Lasers*, Arcidosso, Italy, Sep 2000.

[18] C. Bontoiu and P. Craievich, "Surface Roughness Wakefields. An account for FERMI undulators," Sincrotrone Trieste, Tech. Rep. ST/F-TN-07/07, 2007.

Chapter 5

Passive longitudinal phase space linearizer

Abstract
We report on the possibility to passively linearize the bunch compression process in electron linacs for the next generation X-ray free electron lasers (FELs). This can be done by using the monopole wakefields in a dielectric-lined waveguide. The optimum longitudinal voltage loss over the length of the bunch is calculated in order to compensate both the second-order RF time-curvature and the second-order momentum compaction terms. Thus, the longitudinal phase space after the compression process is linearized up to a fourth-order term introduced by the convolution between the bunch and the monopole wake function[1].

[1]P. Craievich, "Passive longitudinal phase space linearizer," *Phys. Rev. ST Accel. Beams*, vol. 13, n. 3, p. 034401, 2010.

5.1 Introduction

In an FEL the electron bunch is usually compressed to increase the peak current [1] and thus increase the overall efficiency. This compression process is strongly affected by non-linear effects such as the sinusoidal RF time curvature and the second-order path-length dependence on particle energy in the magnetic chicane. In [2] and references contained therein it is proposed to use a short section of radio-frequency accelerating fields at a higher harmonic with respect to the main accelerating linac to linearize the longitudinal phase space of the overall compression process. This technique linearizes the compression transformation through second order. In this note we describe the use of a passive dielectric-lined waveguide to linearize the longitudinal phase space through the compression process instead of an active higher harmonic system. But use of the passive linearizer is not perfect and, after the convolution with the charge distribution, it introduces a fourth-order term in the position-energy behavior that changes the initial bunch profile.
In Sec. 5.2 and using the concepts presented in [3] we summarize the longitudinal single-mode wakes in a dielectric-lined waveguide considering only the two first characteristic waves. In Sec. 5.3 we give an explicit expression for the energy change within a rectangular bunch distribution upon passage through a dielectric-lined waveguide when only the first characteristic wave is considered for the wake function. Thus, as suggested in [2], we work out the voltage needed to completely cancel the second-order compression factor. Furthermore, we give a condition to limit the residual non-linear effects due to the fourth-order term introduced by the convolution between the bunch distribution and the induced wake function of the linearizer. In Sec. 5.4 we present the tracking results considering two cases for a rectangular bunch distribution and the linear compression factor. It is worthwhile noting that the energy change within the bunch due to passage through the dielectric-lined waveguide strongly depends on the charge and bunch distribution. For this reason we also look at the sensitivity of the process as a function of the bunch distribution, in particular the bunch length, and charge variations. In Sec. 5.5 we consider a linear ramped bunch distribution such as that used in [1] and, as in the previous section, we work out the voltage needed to cancel the second-order compression terms. For this case we also give a condition to limit the residual non-linear effects. In Sec. 5.6 we present the tracking results when a passive linearizer is used together with an active fourth-harmonic system in the one-stage compression option of the FERMI@Elettra project [4].

5.2 Longitudinal wake function

Following [3], we summarize in this section relevant aspects of the longitudinal single-mode wakes generated in a dielectric-lined waveguide via passage of a charged particle. Let us consider a charged particle traveling with a speed close to that of light through a pipe of circular cross-section and radius r_2. Let us also assume that the wall of the pipe have infinite conductivity and that it is lined with dielectric material between radii $r_1 < r < r_2$. In the case of such a dielectric-lined waveguide, the longitudinal wake function for the monopole mode, considering only the two first characteristic waves, is:

$$w_{||}(z) \approx A_0 \cos(k_s z) + A_1 \cos(k_{s1} z) \tag{5.1}$$

where the amplitudes are:

$$A_0 = \frac{Z_0 c}{4\pi}\frac{1}{r_2^2}\frac{4}{\epsilon\xi}\frac{x_0 p_0(x_0)}{(d/dx)D_0(x_0)} \tag{5.2}$$

$$A_1 = \frac{Z_0 c}{4\pi}\frac{1}{r_2^2}\frac{4}{\epsilon\xi}\frac{x_1 p_0(x_1)}{(d/dx)D_0(x_1)} \tag{5.3}$$

where Z_0 is the impedance of free space, $\xi = r_1/r_2$ and ϵ is the relative permittivity. The wave numbers of the characteristic waves are defined by:

$$k_s = \frac{x_0}{r_2\sqrt{\epsilon - 1}} \tag{5.4}$$

$$k_{s1} = \frac{x_1}{r_2\sqrt{\epsilon - 1}} \tag{5.5}$$

where x_0 and x_1 are the first two positive zeros of the analytical function:

$$D_0(x) = x p_0'(x) + \frac{x^2\xi}{2\epsilon} p_0(x) \tag{5.6}$$

with

$$p_0(x) = J_0(x)Y_0(\xi x) - J_0(\xi x)Y_0(x) \tag{5.7}$$

$$p_0'(x) = J_0(x)Y_0'(\xi x) - J_0'(\xi x)Y_0(x) \tag{5.8}$$

and where J_0 and Y_0 are, respectively, the Bessel function of order zero and the Neumann function of order zero. We assume that the higher-order modes of wave numbers k_{sn} are suppressed due to the pratical consideration that there will be a finite rms bunch length σ. However, in section 5.6 we give the particle tracking result when the second characteristic wave of wave number k_{s1} is also considered. Figures 5.1 and 5.2 show the amplitudes and wave numbers of the two first characteristic waves as a function of the parameter ξ for $r_2 = 2.5mm$ and $r_2 = 3mm$, respectively.

5.3 Rectangular bunch distribution

For a rectangular bunch distribution $\rho_R(z)$ with full-width L_b, total charge Q, and distributed symmetrically about $z = 0$, the energy change within the bunch due to its passage through a dielectric-loaded vacuum chamber of length L and subject to the wake of the first characteristic monopole mode is given by:

$$\Delta E_s(z) = -eQL\int_{-\infty}^{z} w_{||}(z - z')\rho_R(z')dz' =$$

$$= \begin{cases} = -eQLA_0\frac{\sin(\frac{k_s L_b}{2})}{\frac{k_s L_b}{2}}\cos(k_s z) & \text{if } z > \frac{L_b}{2}, \\ -\frac{eQLA_0}{k_s L_b}\sin(k_s z + \frac{k_s L_b}{2}) & \text{if } |z| \leq \frac{L_b}{2}, \\ 0 & \text{if } z < -\frac{L_b}{2}. \end{cases} \tag{5.9}$$

Let us consider that the electron beam passes through one linac segment and then through a round pipe partially filled with dielectric material as described above. If the beam has an initial

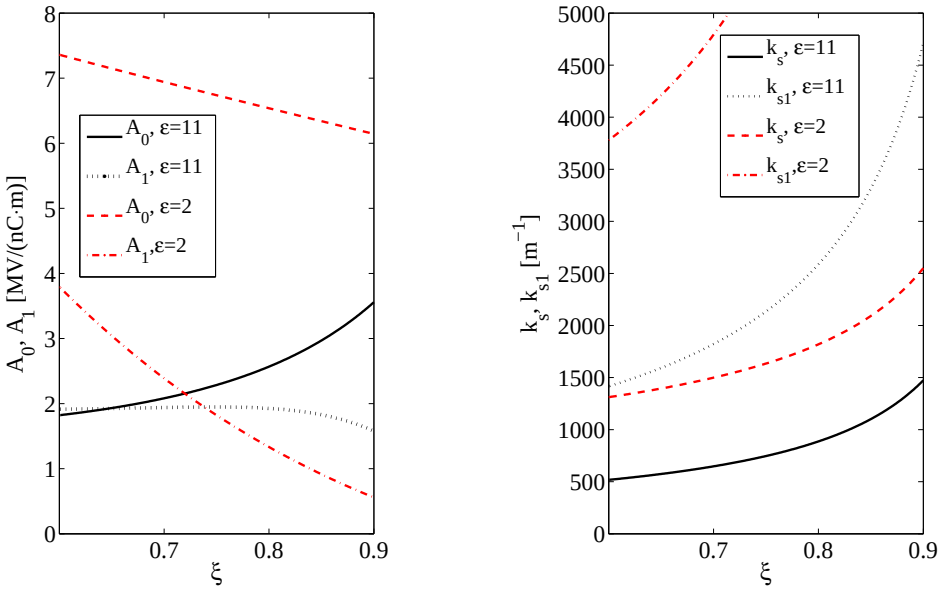

Figure 5.1: Amplitudes (A_0 and A_1) and wave numbers (k_s and k_{s1}) as a function of the parameter $\xi = r_1/r_2$ for $r_2 = 2.5mm$.

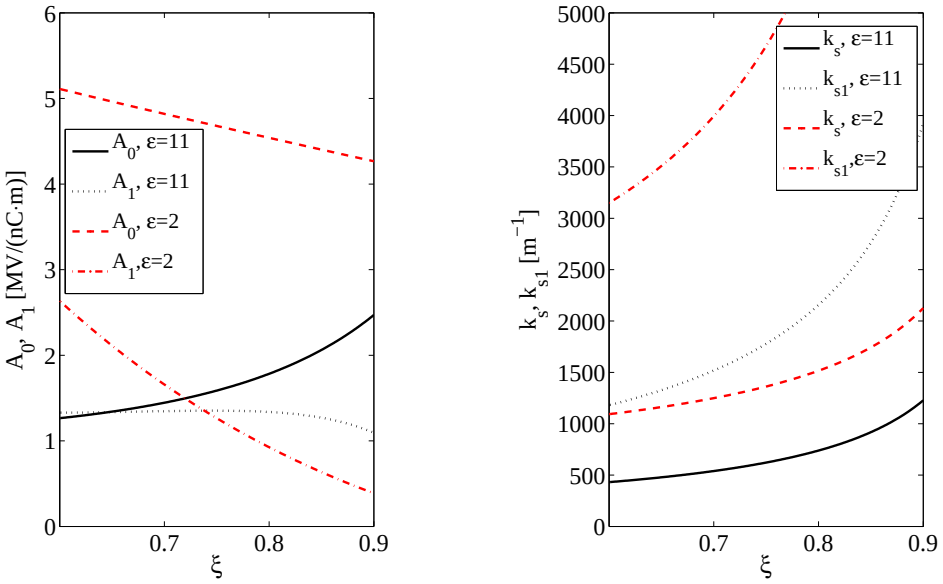

Figure 5.2: Amplitudes (A_0 and A_1) and wave numbers (k_s and k_{s1}) as a function of the parameter $\xi = r_1/r_2$ for $r_2 = 3mm$.

mean energy E_i then following the linac and after the round pipe the electron energy for particles with $|z_0| \leq L_b/2$ is:

$$E(z_0) = E_i + eV_1 \cos(k_1 z_0 + \phi_1) - eA_s \sin(k_s z_0 + \phi_s) \tag{5.10}$$

where k_1 is the RF wave number, V_1 is the amplitude of the voltage of the linac segment, z_0 is the longitudinal position of the particle with respect to the bunch center and the bunch head is at $z_0 < 0$, $A_s = (QLA_0)/(k_s L_b)$ and $\phi_s = (k_s L_b)/2$. The RF phase ϕ_1 is defined to be zero at accelerating crest and a phase in the interval $-90^\circ < \phi_1 < 0$ will accelerate the bunch head less than the bunch tail.
The synchronous mode can provide a decelarating voltage at the bunch center when its phase is $\phi_s \sim \pi/2$ and this condition can be obtained by choosing a dielectric-lined waveguide with $k_s \sim \pi/L_b$. The relative energy deviation can be expanded in a power series about the reference particle and becomes:

$$\begin{aligned} \frac{\Delta E(z_0)}{E_0} \approx & -\frac{eV_1 k_1 \sin(\phi_1) + eA_s k_s \cos(\phi_s)}{E_0} z_0 \\ & -\frac{eV_1 k_1^2 \cos(\phi_1) - eA_s k_s^2 \sin(\phi_s)}{2E_0} z_0^2 \\ & +\frac{eA_s k_s^3 \cos(\phi_s)}{6E_0} z_0^3 - \frac{eA_s k_s^4 \sin(\phi_s)}{24E_0} z_0^4 \end{aligned} \tag{5.11}$$

where E_0 is the chicane energy. In eq. 5.11 we choose to expand up to the fourth-order in bunch length coordinate z_0 for the energy change due to the dielectric-loaded vacuum chamber, while assuming that $k_1 L_b << 1$ we choose to expand only up to the second order in bunch length for the energy gain from the linac.
Let us write the relative energy deviation in (5.11) as:

$$\frac{\Delta E}{E_0} \approx a z_0 + b z_0^2 + c z_0^3 + d z_0^4 \tag{5.12}$$

A magnetic chicane is next used to transform energy deviations into path-length deviations. The chicane transformation can be written to third-order in relative energy deviation as:

$$z = z_0 + R_{56} \frac{\Delta E}{E_0} + T_{566} \left(\frac{\Delta E}{E_0} \right)^2 + U_{5666} \left(\frac{\Delta E}{E_0} \right)^3 \tag{5.13}$$

where $T_{566} \approx -3R_{56}/2$ and $U_{5666} \approx 2R_{56}$ for a typical chicane and R_{56}, T_{566} and U_{5666} are the linear, 2^{nd}-order and 3^{rd}-order transport matrix elements relating energy offset to longitudinal displacements following transport through the chicane.

Putting eq. (5.12) into eq. (5.13) we obtain:

$$\begin{aligned} z &= (1+aR_{56})\,z_0 + \left(bR_{56}+a^2T_{566}\right)z_0^2 + \left(2abT_{566}+a^3U_{5666}+R_{56}c\right)z_0^3 \\ &+ \left(dR_{56}+b^2T_{566}+3a^2bU_{5666}+2caT_{566}\right)z_0^4 \\ &+ \left(3U_{5666}ca^2+3U_{5666}ab^2+2T_{566}da+2T_{566}cb\right)z_0^5 \\ &+ \left(3U_{5666}da^2+6U_{5666}abc+Ub^3+2T_{566}db+T_{566}c^2\right)z_0^6 \\ &+ \left(3U_{5666}b^2c+6U_{5666}adb+3U_{5666}ac_2^2T_{566}dc\right)z_0^7 \\ &+ \left(3U_{5666}b^2d+3U_{5666}bc^2+6U_{5666}acd+T_{566}d^2\right)z_0^8 \\ &+ \left(U_{5666}c^3+6U_{5666}bcd+3U_{5666}ad^2\right)z_0^9 \\ &+ \left(3U_{5666}c^2d+3U_{5666}bd^2\right)z_0^{10} \\ &+ \left(3U_{5666}cd^2\right)z_0^{11} + \left(U_{5666}d^3\right)z_0^{12} \end{aligned} \tag{5.14}$$

Fixing $k_1 z_0 << 1 \ \forall\, z_0$, $k_1 << k_s$, $\phi_s \sim \pi/2$, $eV_1 \sim E_0$, $QLA_0 << E_0$ and $k_s \sim \pi/L_b$, an order analysis is performed and Eq. (5.14) can be simplified as:

$$z \approx (1+aR_{56})\,z_0 + \left(bR_{56}+a^2T_{566}\right)z_0^2 + dR_{56}z_0^4 \tag{5.15}$$

In order to evaluate the quality of the analytical treatment and the degree of confidence in the assumption concerning the approximations, we perform a comparison between the results obtained with eq. (5.13) without approximations and how this deviates from the approximation of eq. (5.15). For this purpose, we consider a realistic set of parameters reported in table 5.1 and also used in the following paragraphs. These parameters are close to the design parameters of FERMI@Elettra project [1]. Figure 5.3 shows that there is very good agreement between the two results.

To compensate the quadratic term in the transformation in Eq. (5.15), the second term must be set to zero:

$$bR_{56} + a^2T_{566} = 0 \tag{5.16}$$

that is:

$$b = -\frac{T_{566}}{R_{56}}a^2 \approx \frac{3}{2}a^2 \tag{5.17}$$

Choosing to hold the energy at the chicane constant and at E_0 and assuming that the synchronous mode is decelerating, then it is necessary to increase the voltage of the linac:

$$eV_1\cos(\phi_1) = E_0 - E_i + eA_s\sin(\phi_s) \tag{5.18}$$

A second requirement is to hold the compression factor, $C = 1/(1+aR_{56})$, constant. If the R_{56} is fixed, then the requirement is to hold the parameter a constant:

$$eV_1\sin(\phi_1) = -\frac{aE_0}{k_1} + eA_s\frac{k_s}{k_1}\cos(\phi_s) \tag{5.19}$$

Using (5.18) to eliminate the eV_1 terms from eq. (5.17) we can calculate the amplitude of the voltage A_s needed to completely cancel the second-order compression terms:

$$eA_s = \frac{1}{\sin(\phi_s)}\frac{E_0\left(1+\frac{3a^2}{k_1^2}\right)-E_i}{\left(\frac{k_s}{k_1}\right)^2-1} \tag{5.20}$$

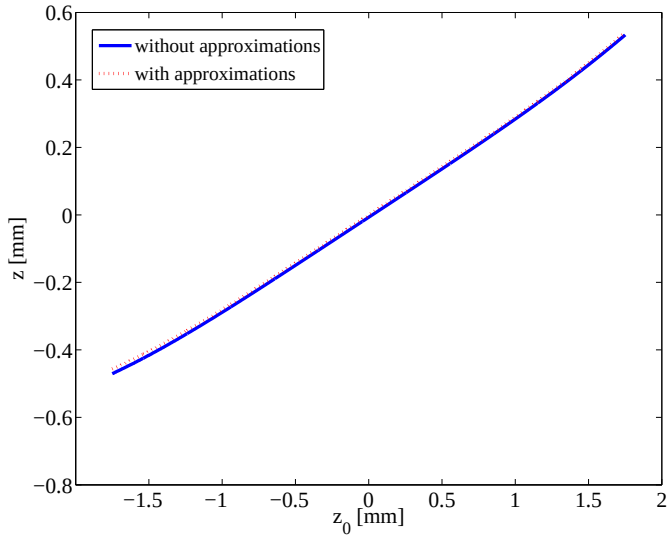

Figure 5.3: Comparison between the compression obtained numerically in eq. (5.13) without the approximations and the compression given by eq. (5.15) i.e. derived from the approximation in the power series for the energy variation of eq. (5.12) and from the simplification due to the order analysis of eq. (5.14).

If $k_s >> k_1$ and $\sin(\phi_s) \sim 1$ then the amplitude A_0 of the synchronous mode can be written:

$$A_0 \approx \frac{L_b}{k_s}\frac{k_1^2 A_{s0}}{QL} \tag{5.21}$$

where

$$eA_{s0} = E_0\left(1 + \frac{3a^2}{k_1^2}\right) - E_i \tag{5.22}$$

In eq. (5.15) the residual non-linear effects are small if the fourth-order term is maintained small compared with the linear compression term, that is:

$$1 + aR_{56} >> dR_{56}\left(\frac{L_b}{2}\right)^3 \tag{5.23}$$

considering the worst condition at the tail of the bunch where $z_0 = L_b/2$.
The condition (5.23) can be rearranged as follows:

$$\left|\frac{R_{56}}{1 + aR_{56}}\right| << \frac{192E_0}{\pi^2 k_1^2 eA_{s0}L_b} \tag{5.24}$$

here we have assumed $k_s L_b \sim \pi$ and $\sin(\phi_s) \sim 1$. Basically, there are two possibilities to limit the residual non-linear effects: the first one is to reduce the bunch length L_b from the photo-injector and the second one is to limit the linear compression factor $C = 1/(1 + aR_{56})$. When the charge and the length of the electron bunch are fixed we can choose a dielectric- lined vacuum chamber with $k_s \sim \pi/L_b$ and A_0 from eq. (5.21). In order to accomodate a range of bunch charges

and current distributions one possible idea would be implement a set of passive linearizers on a movable stage. Each linearizer would be 'tuned' to different values of k_s and A_0 and so could be used for a range of bunch length and charge. Another possible idea would be to use a parallel plate waveguide configuration where changing the gap could be used to vary the synchronous mode.
In the following paragraphs we present the results from the tracking analysis considering two bunch length cases both with a total charge of $1nC$. For both cases we also consider relative bunch length and relative charge variations up to 20% with respect to the nominal parameters at the injector in order to gauge the method's sensitivity to fluctuations.

5.4 Tracking results for a rectangular bunch distribution

In this section we present the LiTrack [5] tracking results for two bunch length cases, $L_b = 3.5mm$ and $L_b = 2mm$. In the former case the linear compression factor is limited to $C = 3.5$, while in the latter the linear compression factor is limited to $C = 6$. The nominal energy at the chicane is $E_0 = 230MeV$, while the initial energy is $E_i = 96MeV$. The wave number of the main accelerating linac is $k_1 = 62.9m^{-1}$. A rectangular bunch distribution with total charge $Q = 1nC$ is used for both cases.

5.4.1 Case 1: $L_b = 3.5mm$ and $C = 3.5$

Figure 5.4 shows the simulated energy profile, longitudinal phase space, and bunch current distribution after the bunch compressor chicane without second order compensation ($V_1 = 149.4MeV$, $\phi_1 = -26.3deg$ and $R_{56} = -3.95cm$). A current spike develops at the bunch head due to the combined RF and compression non-linearities.
Figure 5.5 shows the phase space and the bunch current distribution after the bunch compressor chicane when an active fourth-harmonic RF system is used to compensate the quadratic term introduced by the accelerating RF system and the compressor (in this case the harmonic voltage is $-12.7MV$ while $V_1 = 161.0MeV$, $\phi_1 = -24.3deg$ and $R_{56} = -3.95cm$). The compressed current distribution is nearly unchanged with respect to the initial profile (i.e. it is still rectangular) and the energy-z correlation is linear. Table 5.1 lists the RF and bunch compression parameters

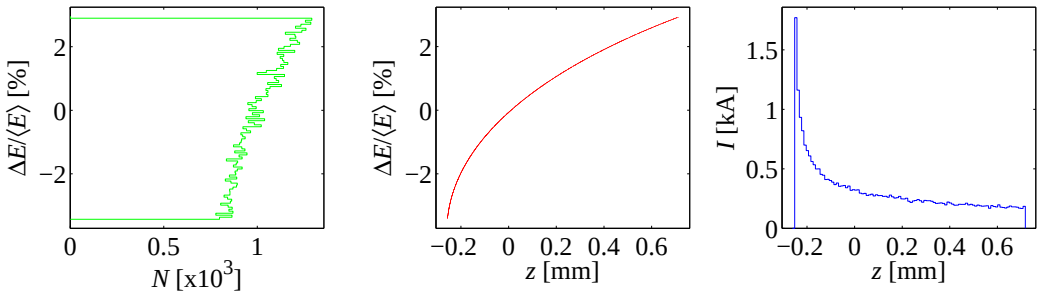

Figure 5.4: Energy profile (left), longitudinal phase space (middle), and beam current distribution (right) after the bunch compressor chicane without passive linearizer or active fourth-harmonic system. An undesirable sharp current spike develops at the bunch head due to the quadratic term in the RF followed by the chicane compression. Bunch head at left, $z < 0$.

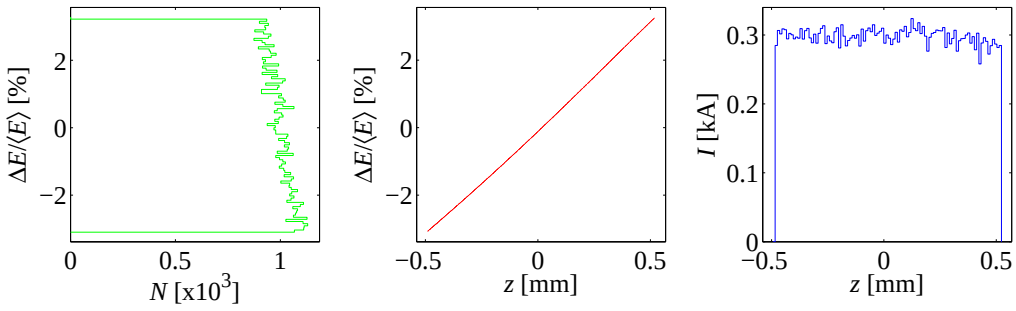

Figure 5.5: Energy profile (left), longitudinal phase space (middle) and bunch current distribution (right) after the chicane when a fourth-harmonic RF system (X-band) is used.

when a passive linearizer is used. The harmonic voltage A_s was calculated from Eq. (5.20) and $k_s = \pi/L_b \approx 890m^{-1}$. The voltage and phase of the linac were adjusted in order to be used with the passive linearizer. Figure 5.6 shows the phase space after the chicane when the passive linearizer is used to compensate the quadratic term. If the remaining fourth-order term remains limited then the phase space is quite linear and the current distribution does not develop a significant sharp current spike at the head of the bunch. On the other hand, there is a distortion of the current distribution due to the the fourth-order term introduced by the passive linearizer. Table 5.1 lists parameters for a possible dielectric-lined waveguide that would meet the requirements necessary to produce the results of figure 5.6. This dielectric-lined waveguide would have radii $r_1 = 2.48mm$ and $r_2 = 3.5mm$, would be $1 - m$ long, and would be lined with a dielectric material with $\epsilon = 2.8$.

Table 5.1: RF and bunch compression parameters for the second-order compensation with the passive linearizer ($C = 3.5$).

Parameter	
V_1	$150.3MV$
ϕ_1	$-26.1deg$
R_{56}	$-3.95cm$
A_s	$0.94MV$
$n = k_s/k_1$	14.33
r_1	$2.48mm$
r_2	$3.50mm$
ϵ	2.8
A_0	$2.95MV/(nC \cdot m)$
L_{guide}	$1m$

We next look at the sensitivity of the process as a function of the bunch length and charge variations. Figure 5.7 plots the relative peak current $\Delta I_{pk}/I_{pk}$, relative mean energy $\Delta E/E$ and bunch arrival time variation Δt_f after the bunch compression as a function of the bunch length variation $\Delta L_b/L_b$ (upper plots) and the relative charge variations $\Delta Q/Q$ (lower plots) at the injector. As an example, the upper middle plot in figure 5.7 indicates that a $\pm 19\%$ bunch length

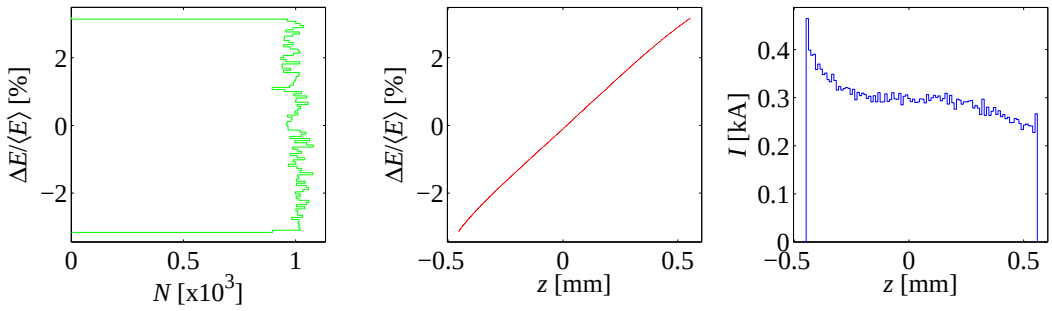

Figure 5.6: Energy profile (left), longitudinal phase space (middle) and bunch current distribution (right) after the chicane when the passive linearizer is used to compensate the quadratic term. The goal is to have the compression factor $C = 3.5$.

variation at the injector causes an approximately to $\mp 8\%$ relative peak current variation after the bunch compression. Table 5.2 lists the sensitivities of the electron beam parameters to the relative bunch length and charge variations. Each sensitivity number quoted in the table independently causes an 8% relative peak current increase, a 0.1% relative mean energy increase and a $150fs$ bunch arrival time increase. Figure 5.10 shows the bunch current distributions after the bunch compression chicane for different bunch length variations at the injector and for different relative bunch charge variations. We can still see that the current distributions do not develop a significant current spike at the bunch head for any of the simulated cases.

Table 5.2: Individual sensitivities. Each parameter variation causes a $\Delta I_{pk}/I_{pk} = +8\%$ relative peak current change, or a $\Delta E/E_0 = +0.1\%$ relative energy change or a $\Delta t_f = 150fs$ bunch arrival time change after the bunch compression.

Parameters		$\Delta I_{pk}/I_{pk} = +8\%$	$\Delta E/E = +0.1\%$	$\Delta t_f = +150fs$
$\Delta L_b/L_b$	[%]	-19	> 20	< -20
$\Delta Q/Q$	[%]	8	< -20	> 20

5.4.2 Case 2: $L_b = 2mm$, and $C = 6$

If the bunch length is reduced, then the compression factor can be increased as seen from the condition (5.24). Table 5.3 lists the RF and compression parameters for the second-order compensation when the compression factor $C = 6$. In this case the wave number of the linearizer is $k_s = \pi/L_b \approx 1572m^{-1}$. Figure 5.8 shows the phase space after the magnetic chicane. As in case 1 the phase space remains quite linear and the current distribution does not develop a significant current spike at the head. However, as in case 1 the current distribution displays a distortion due to the fourth-order term if compared with the situation in figure 5.5 when an X-band system is used. In this case the harmonic voltage A_s, calculated from Eq. (5.20), is approximately 3 times less than the previous case 1 ($0.304MV$ versus $0.94MV$). Thus, if the bunch length, L_b, is reduced approximately 40% with respect to case 1 then the linear compression factor can be

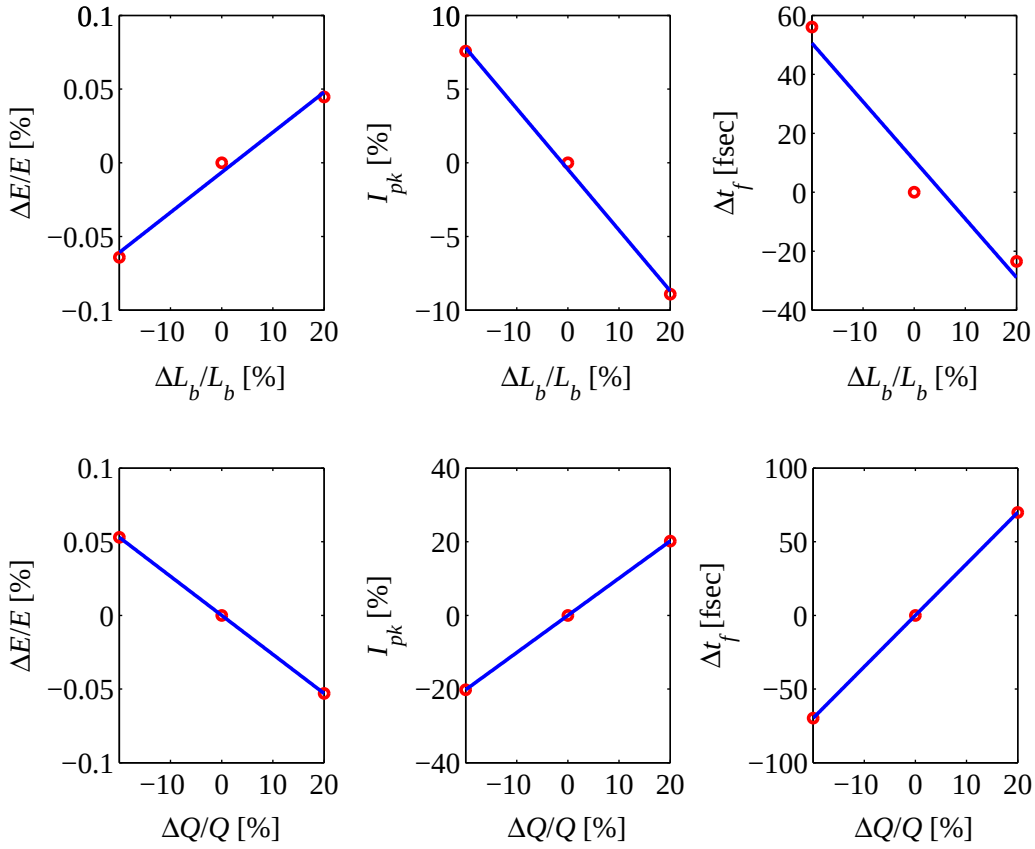

Figure 5.7: Relative mean energy $\Delta E/E$, relative peak current $\Delta I_{pk}/I_{pk}$ and bunch arrival time variations Δt_f as a function of the relative initial bunch length variations $\Delta L_b/L_b$ (upper plots) and relative initial bunch charge variations $\Delta Q/Q$ (lower plots).

increased without increasing the non-linear effects, i.e. C=6. Table 5.3 lists the parameters for a possible dielectric-lined waveguide that would meet the requirements necessary to produce the results of figure 5.8. In this case such a dielectric-lined waveguide would be constructed with the same radius r_2 and dielectric material as in the previous case but it would be $325mm$ long, i.e. considerably shorter than in the previous case. As in the previous case a sensitivity analysis was performed and figure 5.9 plots the relative peak current $\Delta I_{pk}/I_{pk}$, relative mean energy $\Delta E/E$, and bunch arrival time variation Δt_f after bunch compression as a function of the bunch length variations $\Delta L_b/L_b$ (upper plots) and the relative charge variations $\Delta Q/Q$ (lower plots) at the injector. As an example, the upper middle plot in figure 5.9 indicates that a $\pm 20\%$ bunch length variation at the injector causes an approximately to -8%, $+5\%$ relative peak current variation after bunch compression. Table 5.4 lists the sensitivities of the electron beam parameters to the relative bunch length and charge variations. As before each sensitivity number quoted in the table independently causes an 8% relative peak current increase, or a 0.1% relative mean energy increase, or a $150fs$ bunch arrival time increase. Figure 5.11 shows the bunch current distributions

Table 5.3: RF and bunch compression parameters for the second-order compensation with the passive linearizer ($C = 6$).

Parameter	
V_1	$149.5MV$
ϕ_1	$-26.0deg$
R_{56}	$-4.65cm$
A_s	$0.305MV$
$n = k_s/k_1$	25
r_1	$3.15mm$
r_2	$3.50mm$
ϵ	2.8
A_0	$2.96MV/(nC \cdot m)$
L_{guide}	$325mm$

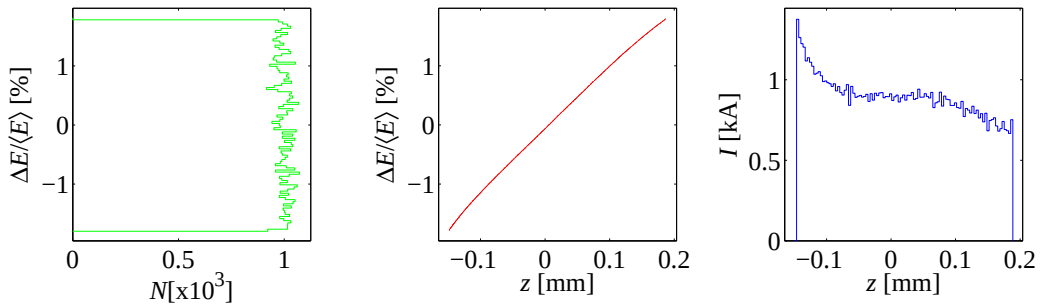

Figure 5.8: Energy profile (left), longitudinal phase space (middle) and bunch current distribution (right) after the bunch compressor when the passive linearizer is used to compensate the quadratic term. The goal is to have a compression factor $C = 6$.

after the bunch compression chicane for different bunch length variations at the injector and for different relative bunch charge variations. The current distributions do not develop a significant sharp current spike at the bunch head in any cases studied.

5.5 Ramped bunch distribution

The operation of X-ray free electron lasers (FELs) relies on extremely high quality electron beams. In the presence of wakefields, the electron density distribution plays an important role in the formation of the electron bunch distribution at the end of the accelerator. The electron density distribution with a linear ramped peak current, obtained through a quadratic ramp in the laser intensity, can in principle compensate the non-linear time dependent variations due to the linac structural wakefields [6]. For this reason we consider a linear ramped charge distribution that can be defined as:

$$\rho_{ramp}(z) = \frac{2}{L_b^2} z + \frac{1}{L_b} \quad \text{if } |z| \leq \frac{L_b}{2}. \tag{5.25}$$

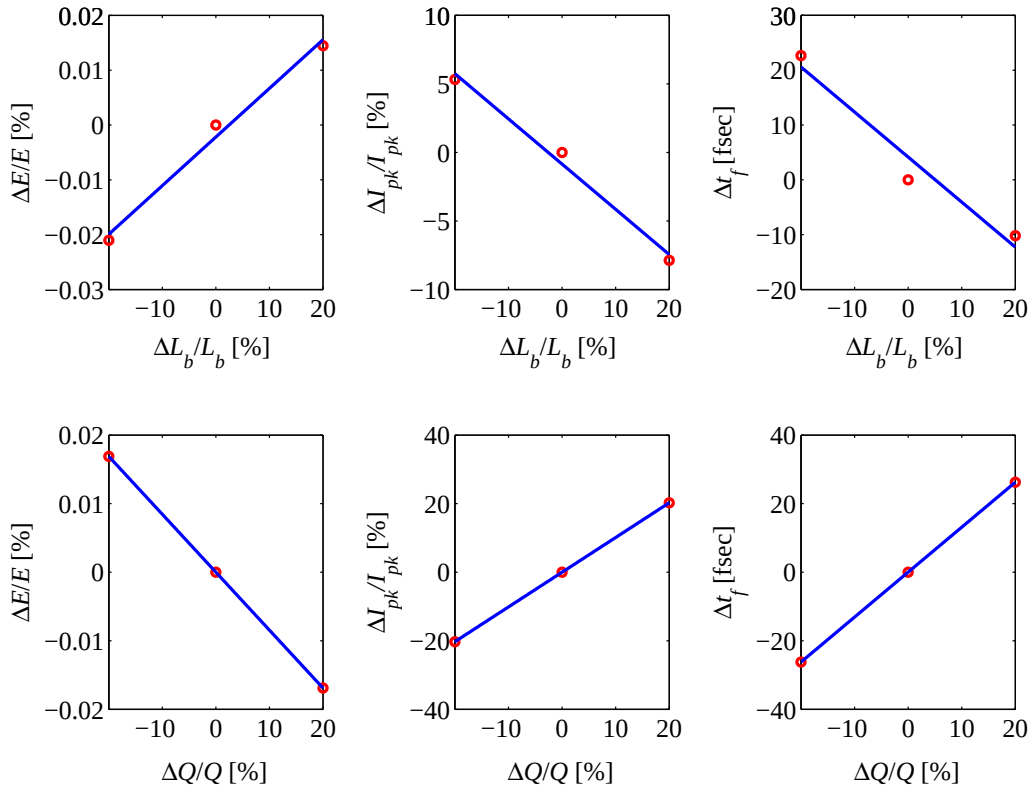

Figure 5.9: Relative mean energy $\Delta E/E$, relative peak current $\Delta I_{pk}/I_{pk}$ and bunch arrival time variation Δt_f as a function of the relative initial bunch length variations $\Delta L_b/L_b$ (upper plots) and relative initial bunch charge variations $\Delta Q/Q$ (lower plots).

The energy change within the bunch itself in a dielectric-lined vacuum chamber of length L is given by:

$$\Delta E_s(z) = -A_s\left[1 - \cos(k_s z + \phi_s)\right] \quad \text{if} \quad |z| \leq \frac{L_b}{2} \tag{5.26}$$

where $A_s = 2QLA_0/k_s^2 L_b^2$ and $\phi_s = (k_s L_b)/2$. In this case the synchronous mode can provide a decelarating voltage at the bunch center when its phase is $\phi_s \sim \pi$ and this condition can be obtained by choosing a dielectric-lined waveguide with $k_s \sim 2\pi/L_b$. The energy change in

Table 5.4: Individual sensitivities. Each parameter variation causes a $\Delta I_{pk}/I_{pk} = +8\%$ relative peak current change, or a $\Delta E/E_0 = +0.1\%$ relative energy change, or a $\Delta t_f = 150fs$ bunch arrival time change after the bunch compression.

Parameters		$\Delta I_{pk}/I_{pk} = +8\%$	$\Delta E/E = +0.1\%$	$\Delta t_f = +150fs$
$\Delta L_b/L_b$	[%]	-20	> 20	< -20
$\Delta Q/Q$	[%]	8	< -20	> 20

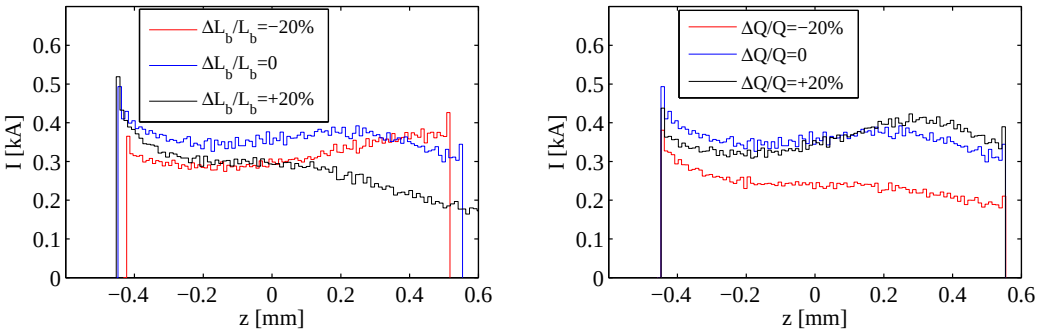

Figure 5.10: Bunch current distributions after the chicane for different bunch length variations at the injector (left plot) and for different relative bunch charge variations (right plot).

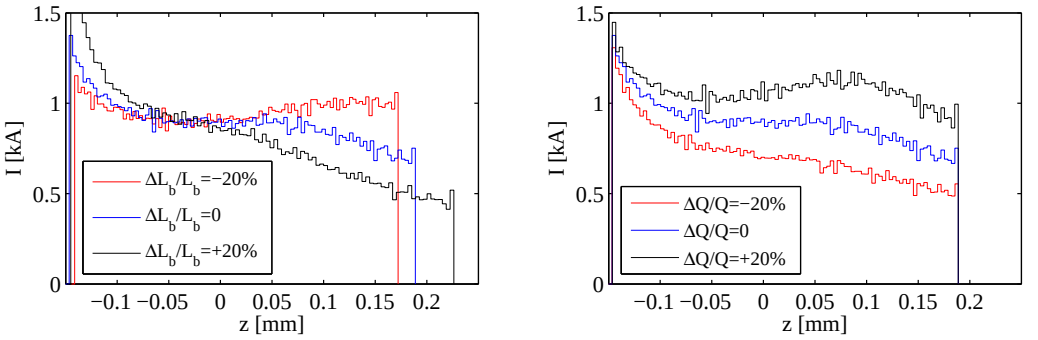

Figure 5.11: Bunch current distributions after the chicane for different bunch length variations at the injector (left plot) and for different relative bunch charge variations (right plot).

Eq. (5.26) can be written as:

$$\Delta E_s(z) \approx -A_s\left[1+\cos(k_s z)\right] \quad \text{if} \quad |z| \leq \frac{L_b}{2} \tag{5.27}$$

As in the paragraph 5.3 for the rectangular bunch distribution, we can calculate the amplitude A_s of the voltage needed to completely cancel the second-order compression terms:

$$eA_s \approx \frac{E_0\left(1+\frac{3a^2}{k_1^2}\right)-E_i}{\left(\frac{k_s}{k_1}\right)^2-2} \tag{5.28}$$

If $k_s >> k_1$ then the amplitude A_0 of the synchronous mode can be written:

$$A_0 \approx \frac{L_b^2}{2}\frac{k_1^2 A_{s0}}{QL} \tag{5.29}$$

where A_{s0} is given in eq. 5.22. Following the same consideration as in the rectangular bunch distribution the residual non-linear effects are small if the following condition holds:

$$\left|\frac{R_{56}}{1+aR_{56}}\right| << \frac{48E_0}{\pi^2 k_1^2 e A_{s0} L_b} \tag{5.30}$$

here we have assumed $k_s L_b \sim 2\pi$ and $k_s >> k_1$. If we compare the conditions described by eq. (5.24) and eq. (5.30), then we observe that the conditions required to achieve a similar level of the beam quality as for the rectangular beam case are 4 times more stringent.

5.6 Tracking results using a passive linearizer and fourth-harmonic system

From the previous sections we have seen that the passive linearizer could work well with a ramped current distribution if the needed harmonic voltage is not too high. An idea could be to use the passive linearizer together with an active fourth-harmonic system for the linearization of the longitudinal phase space. A possible advantage of this option is that both needed voltages, passive and active, could be reduced. In this section we present the tracking results when both systems are used in the one-stage compression option of the FERMI@Elettra project [4]. This option foresees a ramped current distribution with total charge $Q = 0.8nC$. The single bunch beam is produced by a photo-injector, then accelerated up to $250MeV$ and compressed with a single magnetic chicane. After the compression the beam is still accelerated approximately to $1.1GeV$ (linac end) by a linear accelerator, and finally transported to the undulators, where the free electron lasing occurs. Figure 5.12 shows the simulated energy profile, longitudinal phase space, and bunch current distribution at the linac end with parameters given in [4] and using only the fourth-harmonic RF system to compensate the non linearities. In this case the required fourth-harmonic voltage is $19MV$ with an RF phase of $-195°$. Figure 5.13 shows the simulated energy profile, longitudinal phase space, and bunch current distribution at the linac end using a combined passive and active system. In this case the fourth-harmonic voltage is $8.5MV$ and the synchronous mode has a amplitude of $4.4MV/(nC \cdot m)$ and a wave number $k_s = 1440m^{-1}$. Assuming the fourth-harmonic accelerating structure presented in [7] we need an RF power of $4.2MW$ if we use the passive linearizer, and $21MW$ if we only use the fourth-harmonic system. This becomes a practical issue as X-band RF power systems below $5MW$ are commercially available, but at present above that value they are not.
The required voltage for the passive linearizer and the relative wave number can be reached with one dielectric-lined waveguide $1 - m$ long with radii $r_1 = 2.4mm$ and $r_2 = 3mm$. The dielectric material should have a relative dielectric constant $\epsilon = 2.2$ with a thickness of $0.6mm$. The second characteristic wave of the waveguide has the following parameters: $A_1 = 0.5MV/(nC \cdot m)$ and $k_{s1} = 5300m^{-1}$. Figure 5.14 shows the simulated energy profile, longitudinal phase space, and bunch current distribution at the linac end considering also the second characteristic wave. In such a case the fourth-harmonic voltage is $9MV$ and the RF phase $-200°$. This is needed to compensate the spurious effect due to the second characteristic wave.

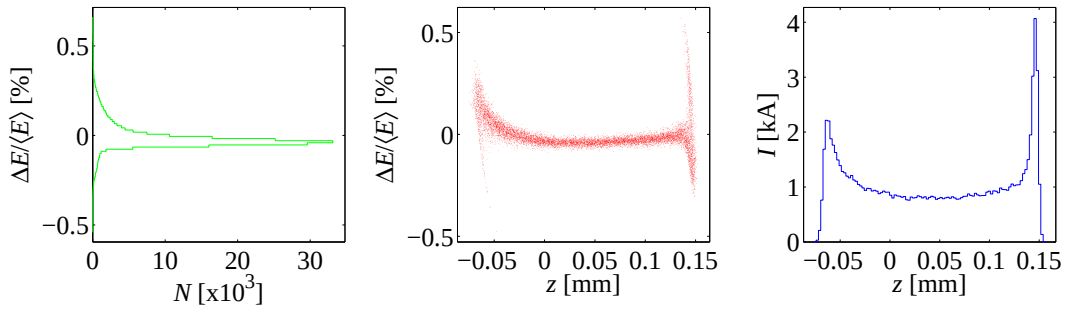

Figure 5.12: Energy profile (left), longitudinal phase space (middle), and bunch current distribution (right) at the linac end when the one-stage compression option as described in [4] is considered. Bunch mean energy $\langle E \rangle = 1067 MeV$.

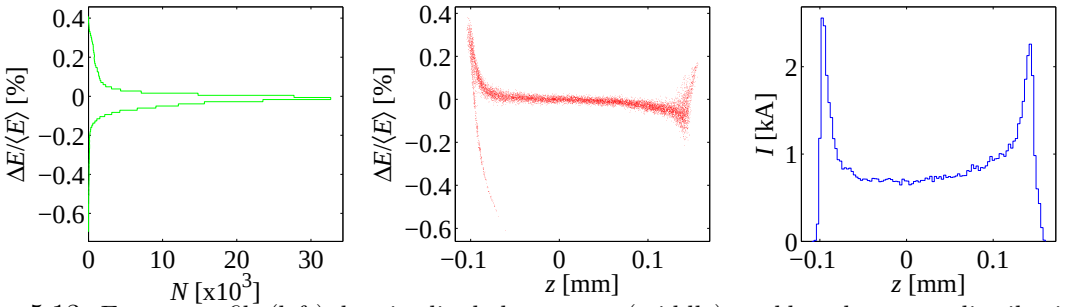

Figure 5.13: Energy profile (left), longitudinal phase space (middle), and bunch current distribution (right) at the linac end when the combined option, passive and active linearizer, is considered. Bunch mean energy $\langle E \rangle = 1076 MeV$.

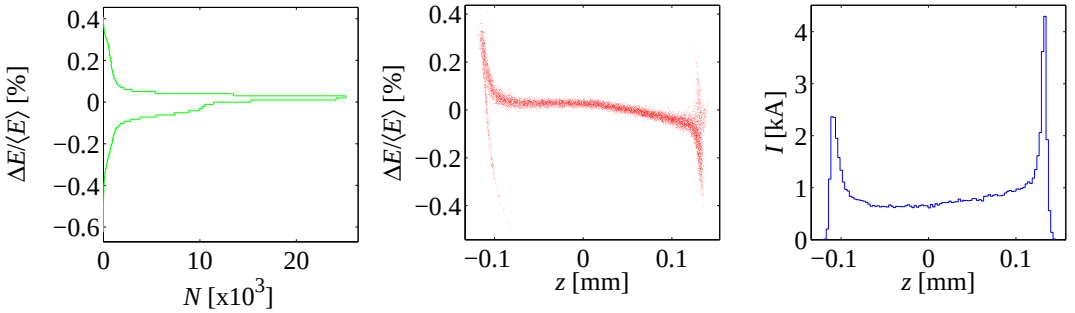

Figure 5.14: Energy profile (left), longitudinal phase space (middle), and bunch current distribution (right) at the linac end when the combined option, passive and active linearizer, is considered. For the passive linearizer the second characteristic wave is also considered. Bunch mean energy $\langle E \rangle = 1076 MeV$

5.7 Conclusion

In this paper a passive linearizer is implemented instead of an active fourth-harmonic linearizer system to compensate both for the second-order RF time-curvature and for the second-order

momentum compaction terms. Using the passive linearizer the current distribution does not develop a significant sharp peak current spike at the head of the beam. On the other hand, there is a distortion of the current distribution due to the the fourth-order term introduced by the convolution between the wake function of the dielectric-lined waveguide and the charge distribution. A condition to limit the non-linear effects due to the fourth-order term is given. Basically, there are two possibilities in keeping the spurious effects small: the first one is to reduce the bunch length from the photo-injector and the second one is to use a small linear compression factor. We have presented the LiTrack tracking results considering two cases of a rectangular bunch distribution with different bunch length and different linear compression factors. For both cases the results have shown that the linearizer can be successfully used in place of the active fourth-harmonic system. Since the energy change within the bunch due to passage through the dielectric-lined waveguide strongly depends on the bunch distribution and charge we have carried out a sensitivity study for both, the case of charge variations and for variations in bunch length of the considered bunch distributions. We have seen that the current distributions do not develop a significant sharp peak current spike at the bunch head for any of the simulated cases. On the other hand, the linearizer is however, tailored to a particular bunch charge and current distribution. In this case in order to accomodate a range of bunch charges and current distributions a possible idea to implement the passive linearizer involving multiple waveguides with separate properties on a movable stage. Each of the dielectric-lined waveguides would be *tuned* with a different wave number k_s and amplitude A_0. Furthermore, the results for the linear ramped bunch distribution, such as that used in [1], were presented. Finally, we have successfully studied the passive linearizer together with an active fourth-harmonic system for the one-stage compression option of the FERMI@Elettra project. As a conclusion, the linearizer can, in principle, be used instead of an active higher harmonic system if the compression factor or the bunch length from the photo-injector are limited. In addition, another result from this work is the suggestion to use the passive linearizer together with an active higher harmonic system. In this way the required higher harmonic voltage could be reduced.
As a final point we must consider the transverse wakefields that can be generated in the dielectric-lined waveguide. The wake functions can be calculated as shown in [3]. For the passive linearizers proposed in this paper the amplitude of the transverse wake functions are of the same order of magnitude, approximately a factor $2 \div 3$ larger when compared to the active fourth-harmonic cavity foreseen for the FERMI layout. Thus, in principle, the transverse wake effects due to the passive linearizer may result in a limited but acceptable amount of emittance growth.

References

[1] "FERMI@Elettra Conceptual Design Report," Sincrotrone Trieste, Tech. Rep. ST/F-TN-07/12, 2007.

[2] P. Emma, "X-band RF harmonic compensation for linear bunch compression in the LCLS," SLAC, Tech. Rep. SLAC-TN-05-004, Nov 2001.

[3] K.-Y. Ng, "Wake fields in a dielectric lined waveguide," *Phys. Rev. D*, vol. 42, pp. 1819–1828, 1990.

[4] M. Cornacchia *et al.*, "Running fermi with one-stage compressor: Advantages, layout, performance," Sincrotrone Trieste, Tech. Rep. ST/F-TN-07/08, Jun 2007.

[5] K. L. F. Bane and P. Emma, "LiTrack: A fast longitudinal phase space tracking code with graphical user interface," in *Proc. of the Part. Accel. Conf.*, Knoxville, Tennessee, May 2005.

[6] M. Cornacchia, S. Di Mitri, G. Penco, and A. A. Zholents, "Formation of electron bunches for harmonic cascade x-ray free electron lasers," *Phys. Rev. ST Accel. Beams*, vol. 9, p. 120701, 2006.

[7] P. McIntosh, R. Akre, W. Brooks, P. Emma, and C. Rago, "Realization of an X-band RF system for LCLS," in *Proc. of the Part. Accel. Conf.*, Knoxville, Tennessee, May 2005.

Chapter 6

Conclusion and outlook

This thesis dealt with analytical and numerical studies of the short-range longitudinal and transverse wakefields and their effects along the linac and undulator chain of the FERMI@Elettra project.
In Ch. 2 we estimated numerically the short-range wake functions in the backward travelling wave (BTW) accelerating structure since existing semi-analytical formulas are not longer valid for these structures. In fact the geometry of the basic cell of the BTW structure is completely different when compared to the geometry of usual constant gradient accelerating structures where the formulas in Ch. 1 hold. Estimation of evolution of the wakefields in the multi-cell structure was done and it was shown that for stabilization of the wake potentials for a short Gaussian bunch at least 7-10 cells out of 162 total cells are needed. Then the short-range wake potentials of the complete BTW accelerating structure were calculated. The analytical models for the wake functions were chosen as a combination of periodic and one-cell dependencies. Thus final short-range longitudinal and transverse wake functions of the BTW structures were obtained by fitting procedures. Figures 6.1 and 6.2 show a comparison between the longitudinal and transverse wake functions of the BTW sections and the wake functions for "standard" constant gradient accelerating structures. From figure 6.1 it is clear that the FERMI@Elettra Linac 3 and Linac 4 accelerating structures are characterized by strong longitudinal wakefields that play a major role in the manipulation of the electron bunch length, peak current and energy spread. The BTW wake functions have been used in the computer codes in order to simulate and to optimize the FERMI@Elettra machine design [1, 2]. In addition, the single-bunch energy spread induced by longitudinal wakefields was analyzed. We found out that the longitudinal wakefields effects could partially be compensated by shifting of the bunch injection phase to optimum values, which however decreases the energy gain. Actually this optimum phase is a possible solution to operate the linac 4 in order to compensate the longitudinal wakefields.
From figure 6.2 let us note that the FERMI@Elettra Linac 3 and Linac 4 accelerating structures are also characterized by strong transverse wakefields that could degrade the projected emittance by laterally displacing the bunch tail with respect to the head (banana shape). In order to gain control of the transverse wakefield induced instability, trajectory manipulation was studied in Ch. 3. This technique was also validated in the presence of shot-to-shot trajectory jitter. In addition a specific script working with Courant-Snyder variables was written to evaluate the residual banana shape after instability suppression in the presence of shot-to-shot trajectory jitter. Basically this study will be the principle according to which the optimization of the transportation in the linac 3

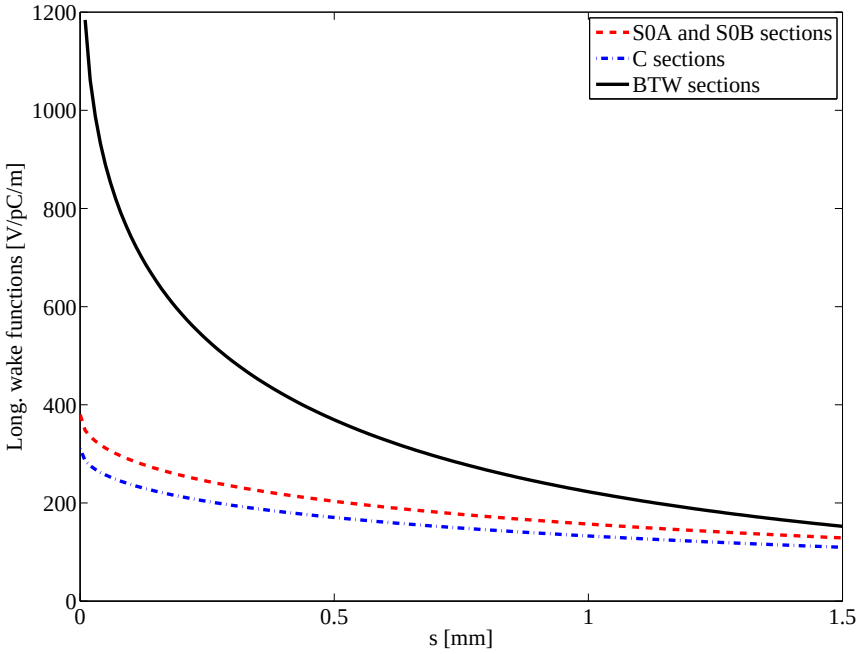

Figure 6.1: Comparison between longitudinal wake functions of the BTW structure and the wake functions of the standard constant gradient accelerating structures. S0A and S0B are the photo-injector accelerating structure while C sections are the accelerating structures of the Linac 1 and 2.

and 4 will be carried out during FERMI@Elettra commissioning.
As possible future research regarding these two chapters I would recommend to validate the semi-analytical model of the short-range longitudinal and transverse wake functions in BTW structures. For this purpose both the average and the shape of the longitudinal and transverse wakefields of the linac should be measured during the next FERMI@Elettra commissioning phases. If the models of wake functions will not be confirmed then a new optimization of the machine design should be carried out.

In Ch. 4 the expressions for the high-frequency longitudinal and transverse resistive-wall coupling impedances of an elliptical cross-section vacuum chamber were derived. This study was motivated since FEL pulses may be corrupted by possible large wakefields along the undulator small-gap vacuum chamber. For FERMI@Elettra the choice for a small-gap vacuum chamber was one with elliptical cross section, for which there are references to analytically derived expressions for the low-frequency resistive-wall coupling impedance. Expressions for the high-frequency resistive-wall impedance are also given in literature, in case of DC and AC conductivity models, for a round pipe and for the conducting parallel plates. The problem of calculating the coupling impedance, including the high frequencies, of a resistive beam pipe with arbitrary cross section has been solved with the boundary element method. In this chapter the expressions for the longitudinal and transverse resistive-wall coupling impedances of a vacuum chamber with elliptical cross

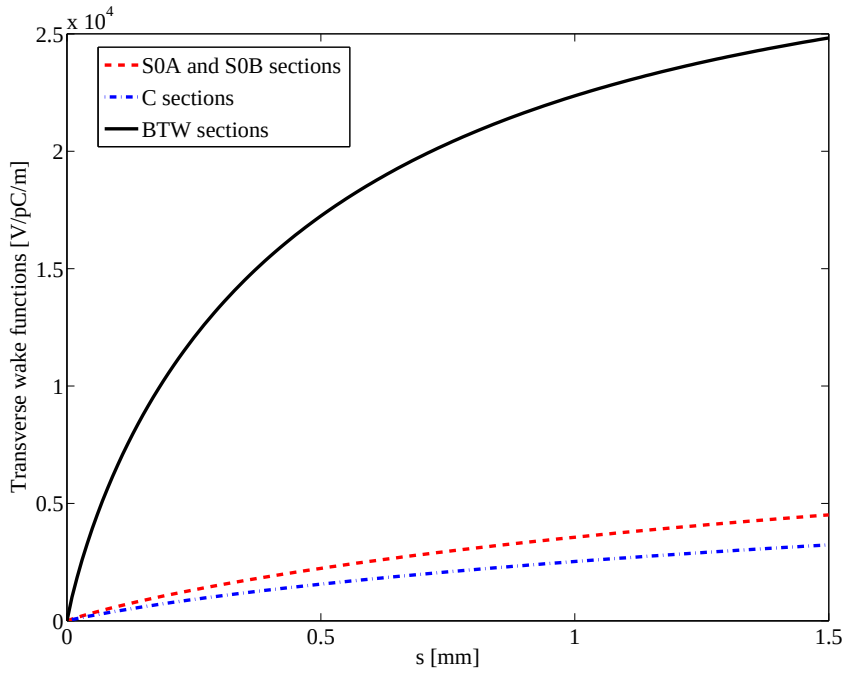

Figure 6.2: Comparison between transverse wake functions of the BTW structure and the wake functions of the standard constant gradient accelerating structures. S0A and S0B are the photo-injector accelerating structure while C sections are the accelerating structures of the Linac 1 and 2.

section were analytically derived using the field matching method. Then, the corresponding longitudinal and transverse wake functions were obtained by calculating numerically the inverse Fourier transformations of the impedance. Once the longitudinal wake function was known the energy changes per unit length induced within particle bunches was estimated. The results showed that the energy variation induced within the bunch could assume an unacceptably large value when shorter bunches are used. As a conclusion of this work, the FERMI@Elettra undulator vacuum chamber was chosen to have elliptical shape with aspect ratio more than 3 and using aluminium as material. With this choice, the amplitude and number of oscillations due to the resistive-wall wakefields can be reduced. Figure 6.3 shows the undulator ultra-high vacuum chamber which has been realized following the specifications given in Ch. 4 [3]. At present, these vacuum chambers are being installed in FERMI@Elettra undulator chains.
As for the longitudinal case, the transverse kick per unit length for the transverse offset received by the particles in the vertical plane within the particle bunch was obtained through the transverse wake function. In this case, the results showed that the kick angle received from the head and tail of the bunch maintains an acceptable value even for shorter lengths than the nominal value of the FERMI project of the charge distributions. Another result from this study, which is worthwhile to mention, is that in a small region around the axis the longitudinal wake function remains approximately constant while the transverse wake function depends linearly on the displacements of the leading and training charges.

At the end of the chapter estimations of the induced single-bunch energy spread caused by resistive-wall and surface roughness wakefields for the actual charge distribution of the FERMI@Elettra project were also presented. Regarding surface roughness wakefields: from this study a specification on the tolerable surface roughness of the vacuum chamber was obtained. The actual vacuum chamber was manufactured according to this recommendation.
As possible future research regarding to this chapter I would recommend to validate the effects of the short-range longitudinal resistive-wall and roughness surface wakefields in the undulator vacuum chamber. This could directly be done measuring the effects on the FEL pulses during the future FERMI@Elettra runs. At present, for this purpose, the FEL properties are currently being studied analytically taking into account the temporal behaviour of the electron bunch energy profile at the entrance and along the undulator chain.

In Ch. 5 we report a novel concept to passively linearize the bunch compression process in electron linacs for X-ray FELs such as the FERMI@Elettra linac. A passive linearizer was implemented instead of an active fourth-harmonic linearizer system to compensate both for the second-order RF time curvature and for the second-order momentum compaction terms. The results showed that the linearizer could be successfully used in place of the active fourth-harmonic system. Since the energy change within a single bunch due to passage through the dielectric-lined waveguide strongly depends on the bunch distribution and charge, a sensitivity study was also done. The results showed that the linearizer still works in the presence of variations of charge and bunch length. It should be noted, however, that the passive linearizer is tailored to a particular bunch charge and current distribution. In addition, another result from this work is the suggestion to use the passive linearizer together with an active higher-harmonic system. In this way the required active higher harmonic voltage could be reduced, which would simplify the design and reduce the required power at X-band frequency.
As possible future research regarding this chapter I would recommend to make a prototype of the passive linearizer. In order to accommodate a range of bunch charges and current distributions a possible idea would be implement a set of passive linearizers with different properties on a movable stage. Each linearizer composed of a dielectric-lined waveguide would be tuned with a different wave number and amplitude and thus the complete structure could be used for a range of bunch lengths and charges. Another possible idea would be to use a parallel plate waveguide configuration where changing the gap could be used to vary the properties of the synchronous mode.

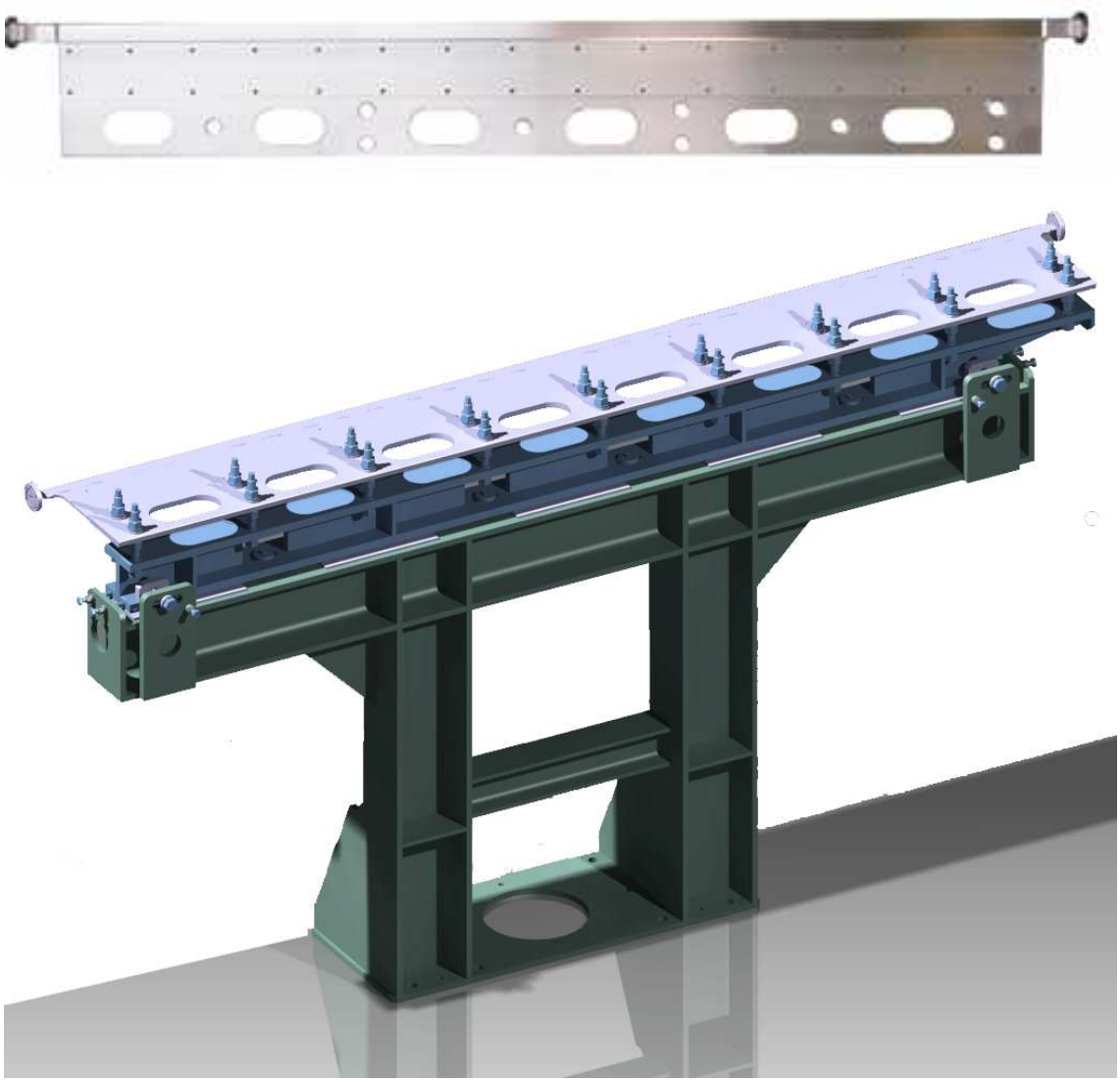

Figure 6.3: The undulator ultra-high vacuum chamber (upper) and its alignment system (lower).

References

[1] "FERMI@Elettra Conceptual Design Report," Sincrotrone Trieste, Tech. Rep. ST/F-TN-07/12, 2007.

[2] S. Di Mitri *et al.*, "Design and simulation challenges for FERMI@Elettra," *Nucl. Inst. Meth. Phys. Res. A*, vol. 608, p. 19, 2009.

[3] G. Lanfranco *et al.*, "Development of Ultra-High Quality Surface Finish Undulator Vacuum Chambers for the FERMI@Elettra Project," in *Proc. of the Int. Part. Accel. Conf.*, Kyoto, Japan, May 2010.

Summary

Short-range longitudinal and transverse wakefield effects in FERMI@Elettra FEL project

The FERMI@Elettra Free Electron Laser (FEL) project is a soft X-ray fourth generation light source under development at the ELETTRA Laboratory of Sincrotrone Trieste. It is one of the FEL based European projects, designed to become the international user facility in Italy for scientific investigations, with ultra high brilliance X-ray pulses, of ultra-fast and ultra-high resolution processes in material science and physical biosciences. When ultra-relativistic charged particles pass through cross section variations of the vacuum chamber wall or experience the finite conductivity of the wall, they generate electromagnetic fields, which are named wakefields since they remain behind the exciting particles. These electromagnetic fields usually influence the energy and the transverse motion of trailing particles leading to beam instabilities, such as single bunch energy spread variations and emittance growth. Since FEL operation requires a beam with a short bunch and high quality in terms of bunch energy spread and emittance, a good knowledge of these wakefields is needed to predict the beam quality. This thesis deals with analytical and numerical studies of the short-range longitudinal and transverse wakefields and their effects along the linac and undulator chain. In Ch. 2 we have estimated the short-range wakefields in the backward traveling wave (BTW) accelerating structure. Each section is a backward traveling (BTW) structure composed of 162 nose cone cavities coupled magnetically. To calculate the effect of the longitudinal and transverse wakefields we have used the time domain numerical approach with a new implicit scheme for calculation of wake potential of short bunches in long structures. The wake potentials of the BTW structure are calculated numerically for very short bunches and analytical approximations for wake functions in short and long ranges are obtained by fitting procedures based on analytical estimations. Finally the single bunch energy spread induced by short-range longitudinal wakefields is analyzed. In Ch. 3 we have studied these electron beam dynamics in the presence of the linac transverse wakefield. Trajectory manipulation is used to gain control of the transverse wakefield induced instability and this technique is also validated in the presence of shot-to-shot trajectory jitter. A specific script working with Courant-Snyder variables has been written to evaluate the residual banana shape after instability suppression in the presence of shot-to-shot trajectory jitter. In Ch. 4 we have analytically derived expressions for the high-frequency longitudinal and transverse resistive-wall coupling impedance of an elliptical cross-

section vacuum chamber. Then, the corresponding longitudinal and transverse wake functions have been obtained by calculating numerically the inverse Fourier transforms of the impedances. In Ch. 5 we report a novel concept to passively linearize the bunch compression process in electron linacs for the next generation X-ray free electron lasers. This can be done by using the monopole wakefields in a dielectric-lined waveguide. The optimum longitudinal voltage loss over the length of the bunch is calculated in order to compensate both the second-order RF time-curvature and the second-order momentum compaction terms. Thus, the longitudinal phase space after the compression process is linearized up to a fourth-order term introduced by the convolution between the bunch and the monopole wake function.

Acknowledgments

Firstly I would like to thank prof.dr. Marnix van der Wiel and dr. Jom Luitien for their effort in supervising my PhD thesis and in particular for having given me this great opportunity. Thanks goes to prof. Fulvio Parmigiani for supporting me during this thesis.
Thanks goes to prof.dr. Thomas Weiland for giving me the opportunity to collaborate with TEMF on the calculation of wakefields in our accelerating sections. I really want to express gratitude to Igor Zagordonov for introducing me to the methods to estimate the wake functions in accelerating structures and for performing the simulations with the ECHO code. Many thanks Igor!
I greatly appreciated the collaboration with Simone Di Mitri with whom I often discussed about the topic of wakefield in recent years. I am also grateful to Simone for performing the huge number of simulations with ELEGANT code in chapter 3. Thanks also goes to dr. Alexander Zholents for supervising and 'deeply' reviewing the work presented in chapter 3. Many thanks goes to Alberto Lutman, my former "PhD student", with whom I worked to get the results of chapter 4. I am grateful to Stephen Milton for his aid and encouragement during the work presented in chapter 5. For fruitful discussion about related issues in this thesis I would also like to thank dr. Max Cornacchia, dr. Sandra Biedron, dr. Enrico Allaria, dr. Mauro Trovò, dr. Bill Fawley, prof. Giovanni De Ninno, dr. Juhao Wu, dr. Paul Emma, dr. Giobatta Lanfranco, dr. Alexander Zholents, Simone Spampinati, dr. Rene Bakker, dr. Carlo Bocchetta, prof. Sergio Tazzari, prof. Roberto Vescovo. A really special thanks goes to dr. Giuseppe Penco for helping me, with new ideas and discussions, in any moment.
Finally, I would like to thank my family and my wife Erika Zettin for their moral support. In particular many thanks go to my wife which has been patient when her husband became a student again. Thanks for putting up with me and for supporting me all the time. Thanks to my son Alvise which allows me at all times to understand what are the important things in life. Last one to greet my daughter waiting to be born...

Curriculum Vitae

3 August 1970	Born at Trieste, Italia
1984 - 1989	Technical High School A. Volta, Trieste, Italy High School qualifications in Telecommunications and electronics.
1990 - 1998	Università degli Studi di Trieste, Trieste, Italy Master Degree in Electronic Engineering. Professional qualification in engineering and inclusion in the engineering register.
1997 - 1998	Consultant at the City of Trieste, Trieste, Italy
2001 - 2004	Consultant at Aleph Consulting SRL, Modena, Italy Development Engineer for moisture and density RF sensors
1998 -	Staff member at Sincrotrone Trieste, Trieste, Italy. From 1998 to 2001 I was in the radiofrequency group focusing my work on the design of the radiofrequency devices, such as normal and superconducting accelerating cavities. From 2001 to 2004 I was in the linac group focusing my work on the travelling wave accelerating structure, wakefield effects and coupling impedances. From 2005 I have been working in the accelerator group working on the longitudinal electron beam dynamics as well. From 2002 I have also been involved in the FERMI@Elettra Free Electron Laser project, in which during the last years I served as a S-band structures lead engineer and physics liaison support for the RF systems and wakefields.